Design, Development and Force Control of a Tendon-driven Steerable Catheter with a Learning-based Approach

Mohammad Jolaei

A Thesis

in

The Department

of

Mechanical and Industrial Engineering

Presented in Partial Fulfillment of the Requirements

for the Degree of

Master of Applied Science (Mechanical Engineering) at

Concordia University

Montréal, Québec, Canada

January 2020

Concordia University

School of Graduate Studies

This is to certify that the thesis prepared

By: **Mohammad Jolaei**

Entitled: **Design, Development and Force Control of a Tendon-driven Steerable**

Catheter with a Learning-based Approach

and submitted in partial fulfillment of the requirements for the degree of

Master of Applied Science (Mechanical Engineering)

complies with the regulations of this University and meets the accepted standards with respect to originality and quality.

Signed by the Final Examining Committee:

_____ Chair
Dr. Wen-Fang Xie

_____ External Examiner
Dr. Shahin Hashtrudi Zad

_____ Examiner
Dr. Mojtaba Kheiri

_____ Supervisor
Dr. Javad Dargahi

_____ Co-supervisor
Dr. Muthukumaran Packirisamy

Approved by   _____
Martin D. Pugh, Chair
Department of Mechanical and Industrial Engineering

_____ 2020   _____
Amir Asif, Dean
Faculty of Engineering and Computer Science

Abstract

Design, Development and Force Control of a Tendon-driven Steerable Catheter with a
Learning-based Approach

Mohammad Jolaei

In this research, a learning-based force control schema for tendon-driven steerable catheters with the application in robot-assisted tissue ablation procedures was proposed and validated. To this end, initially a displacement-based model for estimating the contact force between the catheter and tissue was developed. Afterward, a tendon-driven catheter was designed and developed. Next, a software-hardware-integrated robotic system for controlling and monitoring the pose of the catheter was designed and developed. Also, a force control schema was developed based on the developed contact force model as an *a priori* knowledge. Furthermore, the position control of the tip of the catheter was performed using a learning-based inverse kinematic approach. By combining the position control and the contact model, the force control schema was developed and validated. Validation studies were performed on phantom tissue as well as excised porcine tissue. Results of the validation studies showed that the proposed displacement-based model was 91.5% accurate in contact force prediction. Also, the system was capable of following a set of desired trajectories with an average root-mean-square error of less than 5%. Further validation studies revealed that the system could fairly generate desired static and dynamic force profiles on the phantom tissue. In summary, the proposed force control system did not necessitate the utilization of force sensors and could fairly contribute in automatizing the ablation task for robotic tissue ablation procedures.

Acknowledgments

I would like to pay my special regards to my parents Asieh and Mahmoud who have made it possible for me to have the chance of a better life, Also, I wish to thank my younger brother, Alireza and my good friends who make my life more beautiful.

Contents

List of Figures

List of Tables

Chapter 1

Introduction

1.1 Background

1.1.1 Cardiac arrhythmia

Cardiac abnormalities are known as the prime cause of hospitalization and death worldwide. The most prominent heart disease is coronary artery stenosis (CAS) [1]. Also, arrhythmia, i.e., the abnormality in the heart rhythm rooted in its electrical conduction system, is the second common clinical heart disease [2, 3, 4]. Atrial fibrillation is known as the most common arrhythmia with an overall prevalence of 95% [5]. Arrhythmia is associated with high volume of hospitalization and mortality and entails stroke, sudden cardiac arrest, and heart failure [6, 7]. Different components of the conduction system of the human heart are depicted in Fig 1.1.

Atrial fibrillation (AFib) or arrhythmia is mainly caused by uneven discharge of signals from pulmonary veins (PVs) and will lead to serious heart-related complications. Based on American Heart Association (AHA) statistics, 2.7 million Americans are living with AFib. Studies have revealed that the AFib prevalence will be projected to 12.1 million people by 2030 [9]. Analyzing the electro-cardiogram (ECG) leads to a detailed understanding of the patients cardiac health condition. Cardiac arrhythmias are the condition in which heartbeats are not harmonic, the beats are either faster or slower than normal [10]. Arrhythmic heartbeats pose serious risk to the patients life such as ventricular fibrillation and tachycardia.
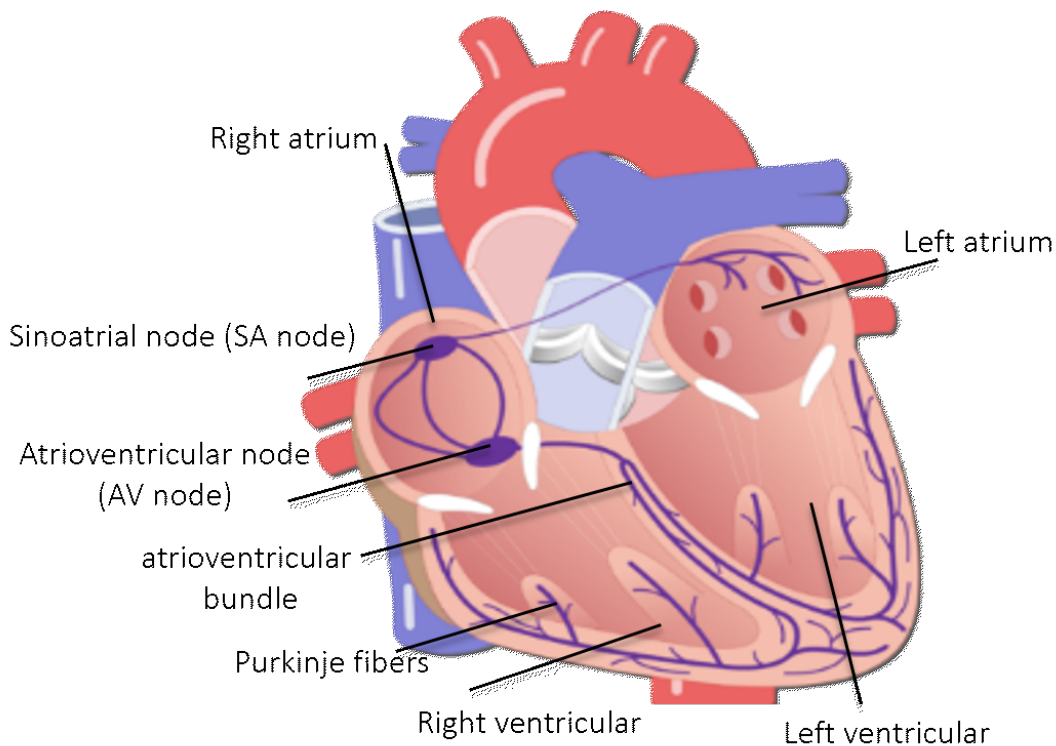
Figure 1.1: SA node or sinoatrial node starts the electrical pulses regularly, 60 to 100 times per minute under normal conditions. The electrical signals then get to the atrioventricular node (also called the AV node). This causes a short delay so the upper part and lower parts of the heart are contracting harmonically. [8].

1.1.2 Treatment options

The current treatment options for arrhythmia are in two categories: drug therapy and non-drug therapy [11]. Different researches have been focused on anti-arrhythmic drug (AAD) therapy. While AADs are recommended for mild cases of ventricular arrhythmias [12]. However, for ventricular arrhythmias surgical ablation is the favorable option. In ablation procedures the ventricular muscles, which are causing undesired pulses or movement in the heart are disabled by being frozen or burnt . The most favorable ablation modality has been radiofrequency ablation (RFA) [13].

Although RFA has exhibited clinical success, treatment efficiency highly depends on the size of the lesion (burnt area) [14]. The average atrial wall thickness in human is approximately 2 mm [15]. During RFA ablation, ablation catheters are inserted to the patient's vessels and are steered toward
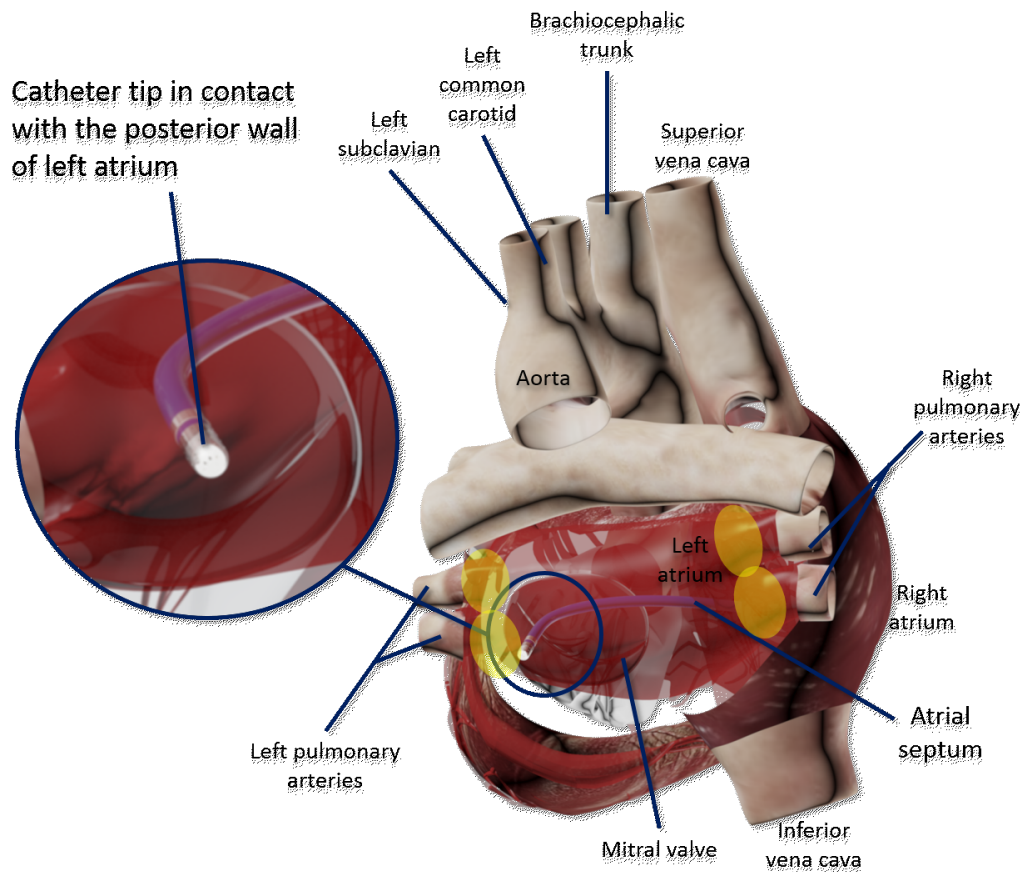
Figure 1.2: To access the ablation target areas (yellow), RFA catheter is passed through the atrial septum, i.e. wall separating left and right atria. Catheter steerability plays a crucial role in both reaching the target areas and maintaining the contact during the ablation procedure [17].

the heart chambers to perform radiofrequency ablation [16]. Steerable catheters are long flexible devices with an RF antenna at the tip that facilitate the delivery of RF waves for RFA ablations. Such devices are widely used in cardiology, neurology, and endovascular minimally invasive srugery, diagnosis, and treatment. Fig. 1.2 depicts the schematic configuration of a steerable catheter inside patient's heart for RFA ablation.
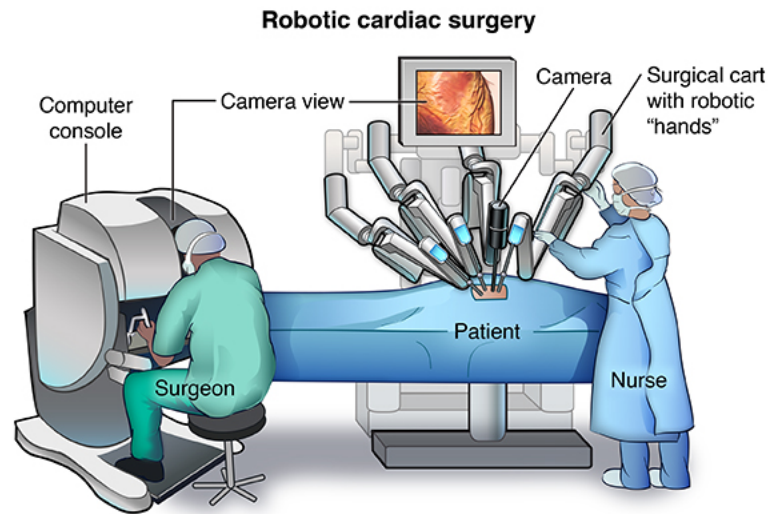
Figure 1.3: A schematic positioning during a robot-assisted cardiac surgery is shown, heart surgery is being done through very small cuts in the chest. The surgeons are doing the manipulations using tiny instruments and robot-controlled tools to do heart surgery [20].

1.1.3 State-of-the-art for treatment

Robotic-assisted surgeries are the current state-of-the-art technology used to treat cardiac abnormalities and perform cardiac surgeries. Robotic catheterization was used to overcome some of the risks associated with conventional intervention methods. Ernst *et al.* [18] reported the early results of robotic catheter ablation with a magnetic navigation system. The results showed that robotic RFA was a safe and feasible tool for remote catheter ablation. Robot-assisted cardiovascular intervention methods are mainly used in percutaneous coronary intervention (PCI), percutaneous peripheral intervention (PPI), electrophysiological intervention (EPI) [19]. A schematic robotic surgery process is shown in Fig. 1.3.

1.1.4 Limitations of the state-of-the-art

Robotic minimally invasive surgeries, a.k.a. robot-assisted catheter intervention (RCI), has enhanced the surgical accuracy, dexterity, and visualization. However, the current commercially available systems do not provide haptic, force, and tactile feedbacks to the surgeons. This limitation has been reported as the most prominent factor hindering the faster adoption of the RCI systems [19].

Giora *et al.* [21] reported a sucess rate of 98.8% PCI with these new methods. Also, RCI has been reported as safe and as effective as the conventional manual approaches [22]. Despite the advantages, the loss of sense of touch is a huge concern during the robotic-assisted surgeries [19, 23]. While the manipulator is doing the intervention to treat or diagnosis, the haptic feedback between the hands of the manipulators and the organ inside the patients body is needs to be compensated. During the manual catheterization, the surgeon controls the of catheter by rotating the proximal portion of the catheter outside the patients body thus perceived the feedback by his/her hand [24]. Another limitation is steep learning curves associated with endovascular catheterization. There are various modalities for training surgeons including synthetic models, animals, cadavers, and virtual reality (VR) simulators [25, 26, 27].

Not having a proper sense of touch will cause guidewire oversteering and rupture in the vessels or heart chamber [28, 29]. It should be mentioned that despite the two sides of the argument in Robotic-assisted new methods, the number and variety of procedures are increasing [30].

Moreover, for the importance of the force feedback, studies have shown that the effectiveness of RFA is highly dependent on maintaining the catheter-tissue contact force between 20 ± 10 grf [31, 32, 33].

Providing haptic feedback in teleoperations has been addressed by two main solutions, being sensor-based, and model-based, a.k.a. direct feedback and sensorless feedback. The former is mainly realized by installing a sensor (or array sensors) at the catheter tip and measure the forces and torques [34, 35, 36]. Important factors to design force sensors for measuring the contact force include thickness, flexibility, sensitivity, and mass-fabrication capabilities. Such force sensors to be used in RF ablation catheter should be able to detect normal and tangential forces, few studies have been carried out to design such force sensors [37, 38]. Valdastri *et al.* [39] proposed a cutting tool with triaxial force-sensing used in minimally invasive interventions. The outer diameter of the sensor was less than 3 *mm* which enabled the sensor to be inserted through a *9 French* catheter guide. *Ex-vivo* muscular tissue cutting experiments were performed to evaluate the performance of the sensor.

On the other hand, the sensorless approach is based on estimating the force based on computational estimation of the force using mechanistic or heuristic models [19].

1.2 Problem definition

The prime problem in the RCI surgeries has been to estimate the contact force and to control it within the safe and effective range. A steerable catheter shall be flexible enough to make its way through the complicated and tortuous vasculature toward the heart. Also, the catheter control algorithm shall be precise enough to accurately navigate the catheter toward the target site and secondly maintain the contact force during ablation in the desired range, i.e., 20 ± 10 grf.

1.3 Objectives

To tackle the problem of intraoperative force estimation and control for RFA catheters, a force control schema based on estimating the contact force through incorporation of the indentation depth into a displacement-based contact model was investigated. More specifically, the following three objectives were defined and followed:

(1) to propose and validate a displacement-based viscoelastic contact model for the interaction of the catheter tip and the cardiac tissue,

(2) to propose and validate an inverse kinematic-based control system for tracking desired position trajectories with tendon-driven RFA catheters,

(3) to propose and validate a force control schema by incorporating the developed contact model and position control systems for tracking desired force profiles.

1.4 Literature review

1.4.1 Steerable Catheters: Taxonomy

Continuum robots are widely used in different fields such as industrial inspections or medical aspects. Generally this type of robots become handy for navigating devices and materials through complex paths [40, 41], which are inspired by natural continuum structures such as elephant trunks, octopus arms ,squid tentacles, and snakes [42, 43, 44]. Different examples of continuum robotic

6

structures can be found in the medical field, catheters and catheter-like instruments are fine examples of these structures[45, 46]. Catheters are widely used for medical purposes such as cardiology interventions to diagnosis or treatment abnormalities. Today additional tools at the tip of the catheters make these devices able to perform wide ranges of operations treatments including coronary stenting, repair of congenital heart defects, heart valve repair or replacement, and ablation of atrial fibrillation (AF) or ventricular tachycardia [47].

A catheter is a thin and flexible tube that is inserted into the patients body and provides a conduit for fluids as well as the surgical devices to go through it and reach the point of the body which is under surgery. A typical cardiovascular catheter is shown in Fig 1.4. Catheters are used to remove any type of undesired fluid from the body or on the other hand, send fluid to perform treatments and diagnoses. Catheters are devices and channels through the body to send medical devices to a particular part of the body for minimally invasive treatment procedures and diagnosis [48]. One of
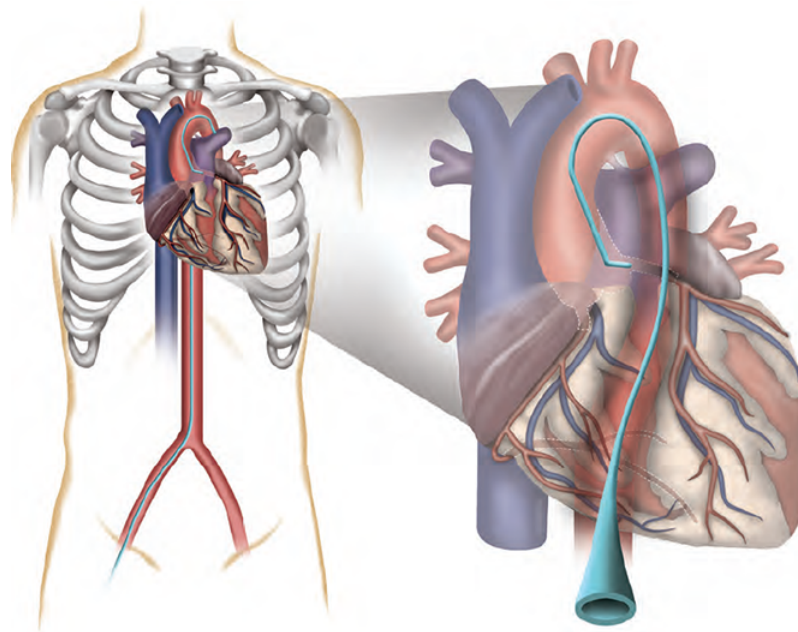
Figure 1.4: A cardiovascular flexible catheter providing a path for fluids and the surgical devices to go through it and reach the under surgery part of the heart [49].

the biggest concerns in interventional cardiology and electrophysiology is to navigate the catheter through the vessels precisely. Heart's continues motion, complex three-dimensional shapes in the

heart and the lack of heart wall support will limit the possibility of precise steering. Steerable catheters were emerged to tackle these very problems. using steerable catheter have shown a huge improvement in procedural time and patient safety [50], as well as greater safety and effectivity as a result of improvement in contact force control [51, 52]. Depending on the level of interaction with humans, different levels of biocompatibility and biomimicry are required for soft materials used in biomedical robotic aspects[53]. Different active soft actuation methods have been postulated by researchers to achieve flexibility, accuracy, safety and dexterity in soft surgical tools. The most effective technologies are cable- driven flexible mechanisms, smart materials and flexible fluidic actuators. There is a wide range of steerable catheters available, Awaz *et al*. [54] proposed a complete review on steerable and force measuring catheters, modelling and methods. Based on this recent report catheters were divided into two main groups of Actuation-Dependent Steering and non-steerable catheters. Actuation-Dependent catheters subsequently were defined as two main groups, catheters with *force generation in tip* and *force transition to tip*.

1.4.2 Steerable Catheters: Driving modalities

Tendon-driven steerable catheters

Tendon-driven mechanisms, are the most common actuation methods for catheters and continuum structure robots [55, 56]. Tendon driven catheters are characterized as soft robots and could be used for various applications [57]. For example, Mehling *et al.* [58], introduced the Tendril robot to be used in surgical procedures performed in space. Flexible catheters provide a wide range of maneuvers inside the body cavities, e.g., atria and ventricles, and are driven with the movement of the tendons connected to the tip of the catheter [59, 60]. Fig. 1.5 depicts a tendon-driven catheter developed by Camarillo *et al.* [61]. Also, a tendon-driven catheter was used to navigate through the frontal sinus [62]. Similarly, another tendon-driven catheter was used for the anterior cruciate ligament (ACL) reconstruction [63]. To find the force at the tip of catheters different models have been proposed, For example, Camarillo *et al.* [61], suggested a linear model for estimating the force at the tip of catheter based on multi-body dynamics and tendon tensions.

In tendon-driven manipulators avoiding slack is one important factor as well as excessive tendon

Figure 1.5: Steerable tendon-driven catheter [61]

loading, redundantly actuated parallel manipulators which are at the same time tendon-driven too, are studied for preventing backlash (slack) but also for minimizing tendon loading [64, 65]. In tendon-driven continuum robots, the number of tendons and the tendon loading distribution are important parameters as well as a sufficient loading model to avoid slack in tendons that cause inaccuracy [66]. Different methods were introduced by Ganji *et al.* [67] to map the changes in lengths of the tendons with the position of the tip of the catheter. Also, Watanabe *et al.* [63] reviewed the history and state of the art of continuous backbone robot manipulators or continuum manipulators. They categorized the catheters based on the actuation mechanism in tendon-based designs, concentric tube designs, locally actuated backbone design, variable backbone stiffness. Tendon-driven was defined as if tendons, were connected along the core backbone to effect bending of the core in several segments [68].

A possible choice for the core backbone is a compressible mechanical spring [69], in some cases to make it more controllable a flexible incompressible rod can be used as the core backbone component [70]. Having said that, the incompressible backbone usage in designs has been a success with numerous implementations [71, 72], however, a spring-loaded design has the advantage of smaller tendon tensions and self reshaping to the resting position.Two important factors in tendon-driven based design are to prevent slack [73] and backlash [74] in tendons to provide precise movement

and desired position control.

Morever, tendon-driven catheters are categorized as catheters with force being transmitted to the catheter tip (single segment design) and force being transmitted to the tip and body (multi-segments design) [52]. Single-segment cable actuation catheters may employ a single cable [75], multiple parallel cables [51, 76] multiple spiraled cables [77] and cable ring [78]. Multi segments catheters could be serial and concentric segments [79, 80]. Cable-driven catheters are scalable and lightweight, but they are hard to sterilize and generally expensive. Other limitations are mechanical limitations such as fatigue, nonlinear friction, backlash, hysteresis and inadequately transmitted forces [81].

Pneumatic-driven steerable catheters

Soft robots with pneumatic actuation (SPA) with internal fluidic channels are normally made of highly stretchable elastomer materials, which deform because of the pressurization of the internal channels to form the desired pose [82]. These actuators have advantages of being lightweight and scalibility [83]. The geometry of the internal fluidic channels and the properties of the materials used in fabrication, define the response of these actuators. The main principle of forming the desired bending in this method is to insert a flexible strain limiting layer in the form of a paper or fabric at the base of SPA and prevent it from elongating [84]. Barrish *et al.* [85] used pneumatically-driven steerable catheter for interventional catheters. This type of bending actuators is adopted as compliant grippers, which are able to passively adopt the complex geometries and dimensional variations and location uncertainty[86, 87]. The deformation exhibited by the nonlinear elastomer materials, which are a common choice to manufacture the SPA based structures, are hard to model and control [88]. Different approaches have been taken into consideration to tackle the problems which are: experimental characterization of the geometry of bending SPAs [89], FEA analysis of cylindrical SPAs for biomedical applications [90] and finally, theoretical modelling of snake robot based on bending of SPAs [91]. Applications that require a highly compliant actuator could take advantage of soft pneumatic actuators (SPAs). The main difference of SPAs from the well known pneumatic actuators (such as the McKibben-type actuators) is that they are made entirely out of soft materials such as the silicone-rubber [92]. Sun *et al.* [92] presented two different geometries of soft pneumatic actuators, to be used in the change in bending or rotary curvature. El-sayed *et*

al. [90] used three different silicone rubbers, i.e., *Ecoflex 0030* and *0050*, and Dragon-skin *0030*, to fabricate a pneumatically actuated silicon module, resembling soft tissue.

Despite the aforementioned advantages, pneumatic catheter drive modality is not favorable for RFA ablation application mainly due to the fact that the risk of air leakage is fatal inside the vessels. Also, as the pneumatic resistance is inversely proportional to the square of catheter diameter, practically-sized catheters, e.g. ϕ6 mm, require high air pressure which increases the leakage and bursting risks.

Magnetic-driven steerable catheters

Magnetic actuated catheters belong to the force generation type of catheters, in which the source of force generation resided on the body of the catheter. Magnetic actuation methods, used for steerable catheters in clinical applications, could be grouped in two main categories: internal magnet actuation and external magnet actuation [52]. Various usage of magnetic catheter localization system, such as Niobe (Stereotaxis, St. Louis, MO, USA) [18], exists in the literature. Another example of magnetic usage in catheterization is in percutaneous coronary intervention (PCI) of complex coronary artery lesions with a magnetic navigation system [93]. For PCI applications, Pappone *et al.* [94] assessed the feasibility of a magnetic navigated catheterization system in patients with atrial fibrillation (AF) and it was shown that it was a safe treatment with a short learning curve method and it can be done by an experienced operator. However, later studies have not ruled out the likelihood of magnetic interference with the medical devices and cardiac activity [19].

Smart material-driven steerable catheters

Smart materials address some of the issues at which tendon-driven technology has lacked on, and as a result, smart materials technologies are used not only for traditional endoscopic or surgical procedures but also for catheter-based procedures that require miniaturization. Shape memory alloys (SMAs) have corrosion resistance, biocompatibility and non-magnetic behaviour and based on these properties are used widely in biomedical fields [53]. They can also be produced in various shapes and dimensions. Smart material usage for actuation in catheters are related to electrical

actuation techniques. Materials which are responding to various ranges of current, so different characteristics can be extracted due to the materials essence.

Electric current is provided to SMA steerable catheters to create a bending force and movement at the tip of the catheter (distal tip) [95]. Electric mechanisms are listed as two main types: 1) direct electric actuation [96], and 2) indirect electric actuation [52, 97]. The direct actuation system is the one with the material itself responding to the electric current by providing the bending motion. In systems with indirect actuation, the material and surrounding medium is responding to the electric current. So far none of the electrical actuation systems are practical in clinical proposes due to the limitation of the bending motion needed in surgeries and the fact that the catheters with electrical actuation systems are yet to become safer to be used in operating rooms and clinical properties. Piezoresistive and strain-gauge sensors were used in different studies to measure both the dynamic and static forces [98, 99]. Despite the primarily good result of this method, it is yet to be improved and is not completely reliable in cardiovascular systems [100]. Because piezoresistive and strain-gauge are susceptible to electromagnetic interference with electrical devices in the operating room. Also, the fact that there is the electrolytic nature of blood running in a cardiovascular sensors working area, limits the reliability and precision of the usage of these materials in this matter [101]. To tackle the problem optical fiber-based sensors for intravascular force-sensing aspects were introduced [102, 100, 103, 104]. In terms of SMAs limitations, it should be mentioned they are resisting limited strain, low speed and control issue (owning to complex thermomechanical behavior) are the other drawbacks [81].

Comparison of driving modalities

To offer a summarized comparison between the presented catheter systems, it is noteworthy that the important aspects of catheterization are steering and positioning to be able to move the catheter to the desired position and keep the constant contact between the catheter and tissue. Commercially available steerable catheters have a tip consisting of one piece as the distal tip and offer the motion in two planes. Increasing the motion area in different planes could be provided by increasing the degree-of-freedom (DoF) of the system. In different actuation systems DoF could be changed by different components, in tendon-driven catheters the number of cables can define the DoF. Having

a higher DoF in the mechanisms will lead to more complexity and more complicated control.

In tendon driven catheters specifically higher DoF will cause new challenges such as preventing friction buckling and wedging of cables with each other or with the surroundings. Even though the behaviour of smart materials is theoretically super-elastic the plastic effects might not be negligible which requires precise rigorous analytical or finite-element analysis (FEA) modeling [105]. The analytical or FEA modeling could be more complicated for the pneumatic catheters. Material and geometric nonlinearities (large deformation) along with the human error in the fabrication process would largely increase the complexity of the modeling. Therefore comparatively and based on the above-mentioned limitations, the tendon-driven catheters is simpler, cheaper, and more practical for the RFA RCI applications.

1.4.3 Steerable Catheters: Modeling as soft robots

Continuum models

Based on the vast design possibilities, Three main groups of possible design strategies were proposed for robots [105]. Discrete robots are the first group that are known as conventional manipulators. DoF and maneuverability of the manipulator increases by increasing the number of discrete joints and form the second group of robots which are known as serpentine robots. This category would include hyper-redundant manipulators. The third group is termed as continuum robots with no discrete joints and rigid links. The manipulator bends continuously along its length the same as biological trunks and tentacles. The motion of the last group is generated through the bending of the robot over a given section despite the traditional robots where the motion generates in discrete joints [73]. Continuum models are grouped as model-based haptic feedback [19], in which the force is estimated through computation, live imaging, boundary conditions of sensors and mechanical model of the catheter. Nakamura *et al.* [106] first introduced a system to estimate the heart motion based on a vision sensor using high-speed cameras and tracking markers fixed on the heart surface. Since the results and the output is directly related to the treatment and patents life, a real-time and accurate solution is needed to avoid any possible damages to the patient [107]. Different continuum models were introduced for continuum robots , e.g., [70], based on the dynamics of a planar, a continuum

backbone section undergoing a large deflection was discussed and a vibration-damping setpoint controller was introduced, based on this very dynamic analysis.

Similarly, Jones *et al.* [108], introduced a new method to the kinematic analysis of the multisection continuum robots. Kinematics enabled the real-time shape control by mapping the input such as tendon lengths or pneumatic pressures with robot shape. The new approach took into consideration bending and different orientation in the final results. Bernoulli-Euler beam theory was used for analyzing the large deflection of a steerable catheter, [109, 110], by neglecting the shear effects and out-of-plane warping of the cross-section due to the high slenderness of the catheters. It was proven that the method introduced in [109], was capable of successful implementation to predict the contact force at the tip of the catheter in steady-state condition and the error reported to be less than 5 %. Their results were promising but their model was could not be extended for the wall contact conditions during RFA. Gao *et al.* [27] developed a reality-based robotic catheter system for training purposes, using a linear finite element model with Bernoulli-Euler elements to estimate the contact force.

Multi-body dynamics models

Among various modeling approaches, the simplicity and computational efficiency make multi-body dynamics models are favorable [19]. A multi-body system is composed of a set of rigid bodies and flexible joints. Multibody dynamics is favorable for the robot control, based on the fact that robot consists of several parts connected by joints. A full review of developments in flexible multibody dynamics was done by Shabana [111]. Their study showed that multibody dynamics is an interdisciplinary field that may incorporate other disciplines such as rigid body dynamics, continuum mechanics, finite element method, and numerical, and tensorial analyses. The methods used in flexible multibody dynamics can be categorized into three different main categories: floating frame of reference formulation, the incremental finite element formulation, and the large rotation vector formulation. Ganji *et al.* [67] proposed a multi-body dynamics model, including rigid links and joints to predict the position of the catheter tip with assuming constant curvature for the catheter.

Particle dynamics models

This method is mainly considered as a proper approach to model the deformation of vascular tissue, and for the catheters and surgical devices also [112]. It can be seen as a macroscopic approximation of a continuous. Angular springs were placed in between consecutive rigid links to lead to a proper approximation of a catheter. To recreate the behaviour of the tissue in contact with the catheter in a robotic surgical interventional, haptic feedback and accuracy control of force feedback are two prominent factors [101]. Normally, vessel segmentation techniques consist of two main groups which are: model-free and model-based methods [113, 114]. A particle-based approach was used to model the complete segmentation of the coronaries [4]. Cotin *et al.* [115] has proposed a physics-based model consists of a set of connected beam elements, which is a particle-based approach to model and analyze the catheter, that is capable of modeling the bending, twisting and compressions in real-time.

Differential geometric models

Mainly the dynamic equations of a deformable structure, either in large or small deformation are highly nonlinear, and due to this nonlinearity and large dimensionality, the use of modern digital computers plays a significant role in analyzing the flexible body structures [111]. Geometric modeling is a method in which the basic assumption is that the whole structure and its shape is dependent on the position of some specific points on the structure which are known as key points, the key points, however, are not entirely placed on the structure and could be anywhere in the space. Piecewise differentiable continuous curves are a fine example of this method to analyze the structure of steerable catheters. Motion equations could be calculated by using the Lagrangian equation of motion based on kinetic, potential and friction or viscoelastic energies according to the defined key points [19]. A flexible beam such as a soft robotic arm or a steerable catheter (which is considered as a beam), in terms of dynamic analysis, has an infinite number of degrees-of-freedom. By modeling the number of DoF is reduced in order to describe displacements and deformations [116, 117]. With this regard, a sequence of connected vertices was used to simulate the guidewire and estimate the final position of the guidewire in [118]. The sets of vertices replicated the guidewire by applying the

same forces on them. By iterating the solution, the equilibrium of forces was achieved with a minimum energy condition. In another effort, Tang *et al.* [119] used the nonlinear Cosserat rod model [120]. Cosserat centerline curve was used to model both bending and twisting of the instrument. The distal tip of the instrument which is shorter and flexible (30 mm) modelled by a generalized bending model that is more computationally efficient.

Comparison

Because of the less susceptibility to noise, low cost and plugging to the currently existing robotic system easily, model-based haptic feedback systems are more popular. Having said that force sensor haptic feedback systems have has less computational cost and shorter response time [101]. To pick the more satisfying model it should be considered that the model is accurate and computationally efficient at the same time [121]. Even though driving a physically meaningful set of equations to define continuity, conservation of momentum and conservation of energy is vital to analyze the catheters and guidewires deformation and motion [122], the continuum mechanics models used for the catheters and guidewires are accurate approaches to be hired [109]. The most noticeable limitations of the model-based haptic feedback are the sensitivity of results based on the mechanical properties of the catheter and vessels [107]. Catheters and guidewires are hyper redundant structures in terms and this factor should be considered in the proposed model [105]. Assumptions should be taken into consideration in order to tackle this problem such as proper geometric constraints in terms of deflections [55], constant radius curvature [123]. The last assumption mentioned above is the main assumption in the presented research.

1.4.4 Steerable Catheters: Control

Teleoperation or robotic surgery on beating heart is challenging due to its motion velocity, i.e., 210 mm/s, and acceleration, i.e., 3800 mm/s^2 [124]. To induce artificial heart arrest, conventional approach was to bypass the hear using a an external heart-lung machine so the surgeons could perform surgery on a still heart. However, this techniquesis not practical in RCI [125].
Various strategies have been proposed to predict and autonomous compensation of organ motion for robotic interactions. Model predictive control (MPC) and visual servoing approaches are examples

of the compensation methods [126, 127, 128]. Dexterous RFA necessitates applying force against tissue at specific points [129, 130], which is a challenge because the flexible catheter structure and heart motion. In an early study, Nakamura *et al.* [106], introduced a new system based on a vision sensor with high-speed cameras to track the fixed markers and estimate the heart's motion. Another vision-based approach was proposed based on model predictive control approach to compensate the heart motion. In their study, a camera was employed to track artificial markers on the heart. However, the artificial markers placed on the heart were not realistic due to the space limitation [131]. Also, Samuel *et al.* [132] proposed and implemented a robotic catheter system with 3D ultrasound image guidance along with a force control method to enable constant contact with a moving tissue. The proposed system was a combination of position tracking, force feedback, and friction and backlash compensation to maintain accurate contact between the catheter tip and tissue. However, their proposed system was slow in terms of realtime operation. More recently, a Gaussian mixture model was used in [133] for sensorless shape sensing and force estimation of the magnetic catheters. However, the spatial resolution of their proposed method was coarse, i.e., ± 2 mm.

Force Control

Force feedback is a control approach in soft robots (steerable catheters). Different force control architectures have been proposed to estimate the force on RFA catheters. Zarrouk *et al.* [134], introduced a force control system based on non-linear state feedback to linearize the dynamics of the robot and a PID controller to track the contact force, respectively. Also, Dominici *et al.* [135] proposed a force control to compensate for physiological motions using a process model for predicting the behavior based on the applied force. The results showed that the proposed control approach was efficient to compensate heart motion along Z-axis.

To control the contact force at the catheter tip, usually a single closed-loop force control architecture is used [133]. Based on the literature, the *in-vivo* experiments, the robotic force tracking has been shown to be feasible in beating heart through feeding forward the target position information in the force control loop. Nevertheless, this has led to that the current studies necessarily rely on direct force sensing **AND** visual tracking of the target anatomy in realtime.

Position control

A cable-driven endoscopic system was proposed by Bardou *et al.* [74]. It was shown that because of the cable slack the position control was not accurate, thus the use of a second sensor was necessary to measure the cable tensions. Normally continuum robots offer compliant and dexterous operations, which make them suitable in unstructured environments. Tendon driven catheters based on their intrinsic and their continuum structure are implemented in MIS such as intracardiac interventions. However, based on the intrinsic nonlinearities and external disturbances, it still is hard to accurately steer the catheter tip to the desired 3D positions. A novel probabilistic kinematic model and a model-based 3D position control scheme for a tendon-driven cardiac catheter was offered [136], which introduced a closed-loop position control.

In an early study, a joint space controller was implemented by Penning *et al.* [137] for a position control of a continuum manipulator. Position control is a method when the focus is solely on the positioning of the catheter tip and not to control either catheter shape or tip rotation. Position and task space control represent a very different structure in control, but with some specific assumptions, they seem to produce nearly identical results. To this end, Penning *et al.* [138] have employed linearization of the inverse kinematics about a target point in the task space. However for the linearization to be accurate their method necessitated that the target point remain within the local neighborhood of the resting (initial) point.

Another important aspect in the position control, is the notion of visual servoing, where the position is controlled based on the live feedback from a vision modality. For example, Smith predictor [139] and Kalman filtering [140] were suggested recently to predict and compensate for the organ motion under the delayed vision and ultrasound images, respectively. However, these visual-based methods have some drawbacks such as: a) requiring a vision and/or ultrasound imager to follow artificial or natural landmarks inside the heart tissue, b) during interactions with the surgical instrument, the hearts soft tissue deforms, which increases errors of the vision systems, and c) the processing of some vision data like the ultrasound images is time-consuming and incur time-lag for the feedback control system.

Also, position sensor embedded on the catheter body have been investigated for measuring the depth

of indentation of the catheter into cardiac tissue as an indicator of the contact force [141]. They also have used a combination of contact force, ablation duration and ablation power to obtain the desired lesion size.

Impedance control

Recently, Sharifi *et al.* [126] proposed a novel bilateral impedance control method for robotic surgeries on the beating heart, using measured interaction force. In this impedance control method, there is no need for heart motion prediction, observation and/or learning. So the surgeon can sense the non-oscillatory part of the interaction force by defining an impedance model for master and slave robot, and it will lead to less fatigue for the surgeon since he/she does not need to compensate for the heart motion manually. Another impedance control method was proposed in [142] which was to explore the difficulties of executing low impedance control on a novel hand-held motion compensation device. To this end, Florez *et al.* [142] proposed and validated a force feedback control system on a simulated surgical scene. In some cases that high dry friction in the contact or inertia cannot be compensated by simple impedance control methods, a sensory function can be used in which the robot shares control of the instrument with the user [143].

1.5 Contributions

The main contribution of this research was that, to the best of author's knowledge, it was the first study to propose a sensorless force control schema for tendon-driven RFA catheters incorporating the tissue contact model. The force estimation, position control, force control, and the developed RCI system are subjected to intellectual property protection by Concordia University and could be used for commercialization purposes. Also, in terms of knowledge dissemination, the following contributions have been made:

(1) "Displacement-based Model for Estimation of Contact Force Between RFA Catheter and Atrial Tissue with ex-vivo Validation" presented and published in *IEEE International Symposium on Robotic and Sensors Environments (ROSE)*, 2019, Ottawa, ON, Canada,

(2) "Position control of a flexible tendon driven catheter: Theory and Validation", presented and published in *30th International Conference on Adaptive Structures and Technologies*, 2019, Montreal, QC, Canada,

(3) "Toward task autonomy in robotic cardiac ablation: learning-based kinematic control of soft tendon-driven catheters", submitted and under review in *Soft Robotics (SORO)* Journal,

(4) "Sensor-free force control of tendon-driven ablation catheters through position control and contact modeling", submitted and under review in *42nd Annual Conference of the IEEE Engineering in Medicine and Biology*, Montreal, QC, Canada.

1.6 Dissertation layout

This thesis is structured in a manuscript-based format and consists of the following five chapters and two appendices:

Chapter 1 provides the introductory materials, i.e., background, problem definition, objectives, literature review, and contributions.

Chapter 2 presents the proposed displacement-based direct and inverse contact models and the implemented solution schema as well as the experimental validation studies.

Chapter 3 includes the proposed method for inverse kinematic-based position control of tendon-driven catheters. Also, it presents the validation studies performed for assessment of the performance of the proposed and developed RCI system.

Chapter 4 is consisted of the control system architecture, system components, and the implementation methodology for the proposed force control schema. Also, the results of the validation studies are presented.

Chapter 5 summarizes the main contributions and achievements of this research. Moreover, the research limitations are acknowledges and mitigation measures are proposed for the future works.

Appendix A summarizes the code developed in Matlab for defining the desired position trajectories.

Appendix B discloses the code developed in Matlab for solving the explicit tissue contact model.

Chapter 2

Displacement-based Model for Estimation of Contact Force Between RFA Catheter and Atrial Tissue with *ex-vivo* Validation

2.1 Abstract

The goal of this study was to investigate the validity of a new contact model for sensor-less estimation of the contact force between RFA catheter and atrial tissue. To this end, a new nonlinear displacement based model was proposed. Also, the model was formulated for forward and inverse problems and two solution schema were proposed. For assessing the model performance, two dynamic *ex-vivo* indentation tests were performed on a freshly excised porcine atrium, i.e. one with sinusoidal and one with triangular indentations. Results of the first test were used for parameter identification and verification of the model, while the second test was the benchmark for the model validation. Displacement range for both tests was 2 ± 1mm, while the frequencies of indentations were 1, 1.5 and 2Hz for the sinusoidal, and 1.25Hz for the triangular indentation. From the sinusoidal test results, model parameters were identified using a particle-swarm optimization method.

Using the optimized parameters, experimental forces were reconstructed. Error analysis revealed that the model was 91.5% accurate in repeating the results of the sinusoidal test. Also, validation results showed an accuracy of 90.9% in model predictions of the contact force in the triangular test. Furthermore, the model could successfully capture the stress relaxation phenomenon, which is of high prominence in contact force control on atrial tissue. In conclusion, this investigation confirmed that the proposed contact model was valid in prediction of dynamic contact force with atrial tissue. Also, the proposed solution schema was fast-enough to be used in real-time surgical applications.

2.2   Introduction

Minimal invasive surgery (MIS) and robot-assisted minimal invasive surgery (RAMIS) approaches have become more popular in recent years. More specifically, these approaches have significantly enhanced the effectiveness of surgeries through decreasing the operation time, incision size, intraoperative bleeding, and post-operative recovery time. In an open surgery (non-MIS), palpation helps the surgeon to distinguish different biologic tissues and identify potential anomalies, e.g. tumor or lump, in a biologic tissue or organ [144]. However, in an MIS (or RAMIS) procedure, since the surgeon utilizes specialized instruments to perform surgery through the skin, palpation is not practical.

The MIS instruments are usually long and thin to pass through a small (2-5cm wide) skin incision. Therefore, due to the indirect touch on the organs, the natural haptic and tactile perception (comprising the sense of touch) is lost [145]. Many investigations have identified the loss of tactile and haptic perception as the main limitation of MIS and RAMIS approaches. Also, there is growing evidence recognizing this limitation among the prominent causes of misdiagnosis and malpractice during MIS and RAMIS surgeries [146].

Tactile perception is of prominent importance in the case of cardiovascular or neurosurgery. Specifically, for cardiac radio-frequency ablation (RFA), the effectiveness of the procedure depends on maintaining the contact between the catheter tip and cardiac wall at a certain state, i.e. 20 ± 10gr-force with a minimum force-time integration (FTI) of 400 gr.sec [31, 147, 148]. Fig.2.1 depicts a typical ablation catheter during RFA procedure. An optimal contact force against the cardiac wall

22
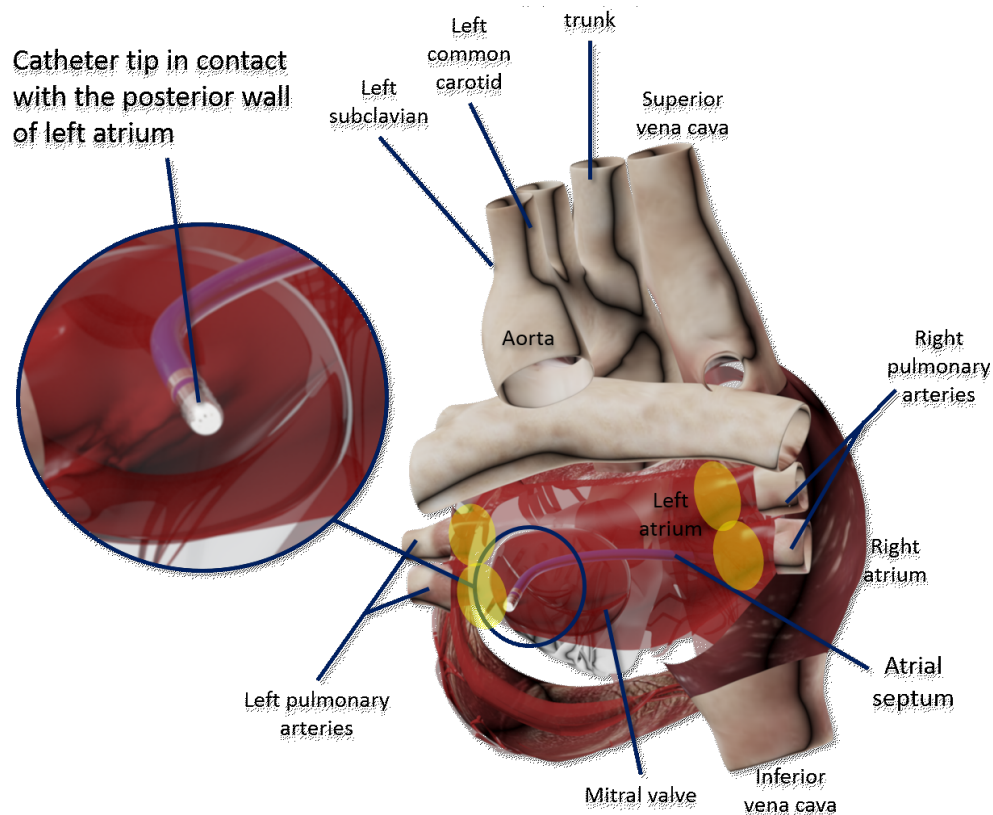
Figure 2.1: To access the ablation target areas (yellow), RFA catheter is passed through the atrial septum, i.e. wall separating left and right atria. Catheter steerability plays a crucial role in both reaching the target areas and maintaining the contact during the ablation procedure.

ensures an optimal contact establishment necessary for transmission of energy to the tissue, while prevents tissue perforation. Tissue perforation has been reported as a sequel to excessive compressive force [149, 31].

In an RFA procedure, surgeon perceives the contact force via sensing the tactile cues at the held end of the ablation catheter (a.k.a. proximal end) [150, 151]. This perception is shown to be inaccurate and simply polluted by dynamic forces acted upon the catheter because of the natural motion of heart [152, 151] and the friction between catheter, vasculature and introducer sheath [152]. Also since the RFA catheter is very floppy, maintaining the contact force solely via proximal insertion is cumbersome.

On the other hand, flexibility is essential for maneuverability of the catheter inside the vasculature. For the catheter being flexible yet sturdy-enough to push against the cardiac wall, researchers have

(a)

(b)

(c)
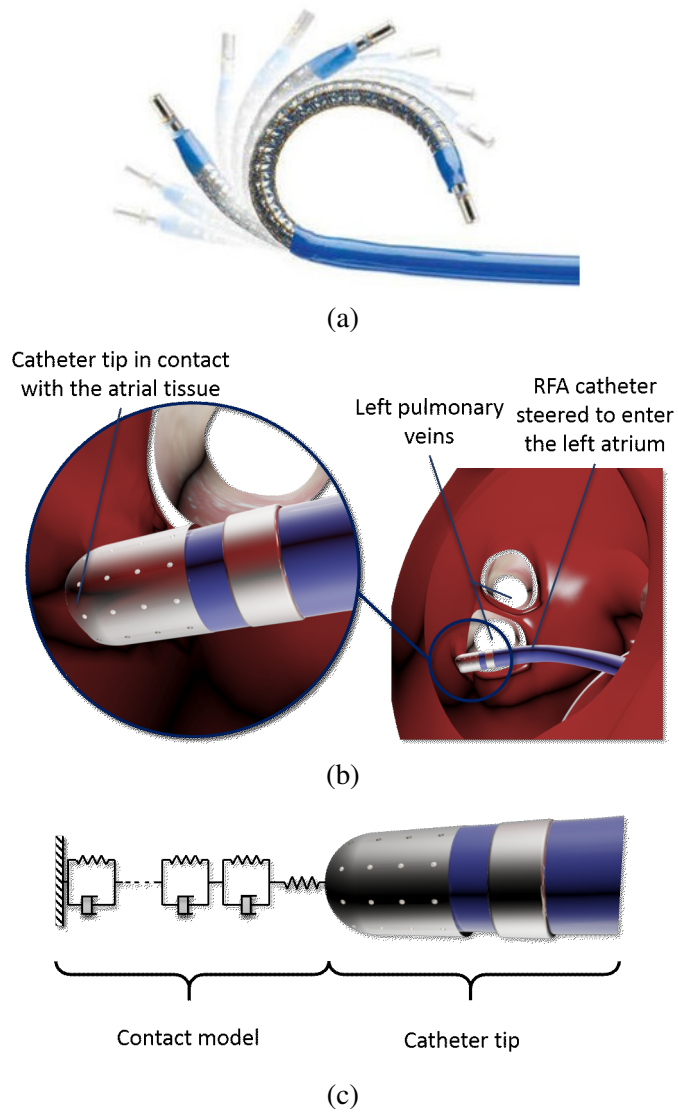
Figure 2.2: (a) a typical steerable catheter, Artisan® steerable catheter (Hansen Medical Inc., subsidiary of Auris Health, Inc.), (b) schematic internal view of the left atrium with RFA ablation in place, and (c) mechanical model of the contact between the atrial tissue and RFA catheter.

suggested the use of steerable catheters, e.g. Fig.2.2(a) [52]. The shape of the distal end of a steerable catheter is changed through a mechanistic pulling and releasing a series of cables (tendons) at its handle. Extensive reviews of the taxonomy and mechanisms of steerable catheters are provided in [68, 153].

For better monitoring of the contact force during an RFA, different sensors have been explored to be embedded at the tip of steerable catheters. Researchers have postulated sensing principles of piezo-resistive [154], piezo-electric [155, 156] and optical-based sensors [157, 100, 158] for this purpose.

To this end, sensor-embedded catheters have been commercialized and successfully used in the clinical setup, e.g. *TactiCath^{TM}* (Abbot Vascular, CA, US) and *Carto® SmartTouch^{TM}*, (Biosense Webster, CA, US). Despite the superior clinical performance [159], such catheters are yet to be widely accepted in the clinics. Researchers have indicated different reasons for that, including the complexity of embedding sensors on the catheters, its relatively high cost for clinics, the compromised maneuverability of the distal end due to added weight and the stiffness of sensor, and its high susceptibility to noise and uncertain conditions inside atrial chamber[160].

Alternatively and by emergence of the robot-assisted cardiovascular intervention, researchers have postulated robotic force control of steerable catheters base on the real-time force sensor information [161]. However as stated earlier, the use of sensor-embedded catheters is of particular limitations. As an alternative, Kesner *et al.* demonstrated the feasibility of maintaining the contact force on a sensor-embedded catheter inside a mitral valve phantom based on real-time mitral motion detection using ultrasound [162]. Also, Khoshnam *et al.* postulated a 3R mechanical model for mapping the position of the tip of a catheter to the force at its tip [163]. However, they adopted a shape-sensing algorithm which entailed an inverse dynamic model to estimate forces based on real-time catheter shape detection.

To overcome the limitation of dependency on real-time data from a force sensor, it was hypothesized that the contact force could be controlled adopting a sensorless force control strategy. Fig.2.2(c) depicts this concept schematically. Advantages of this postulation would be to limit the use of sensor data to merely the characterization of the tissue; while the force control is performed based on a displacement-based model. Researchers have postulated various fast algorithms for the real-time

(a)

(b)
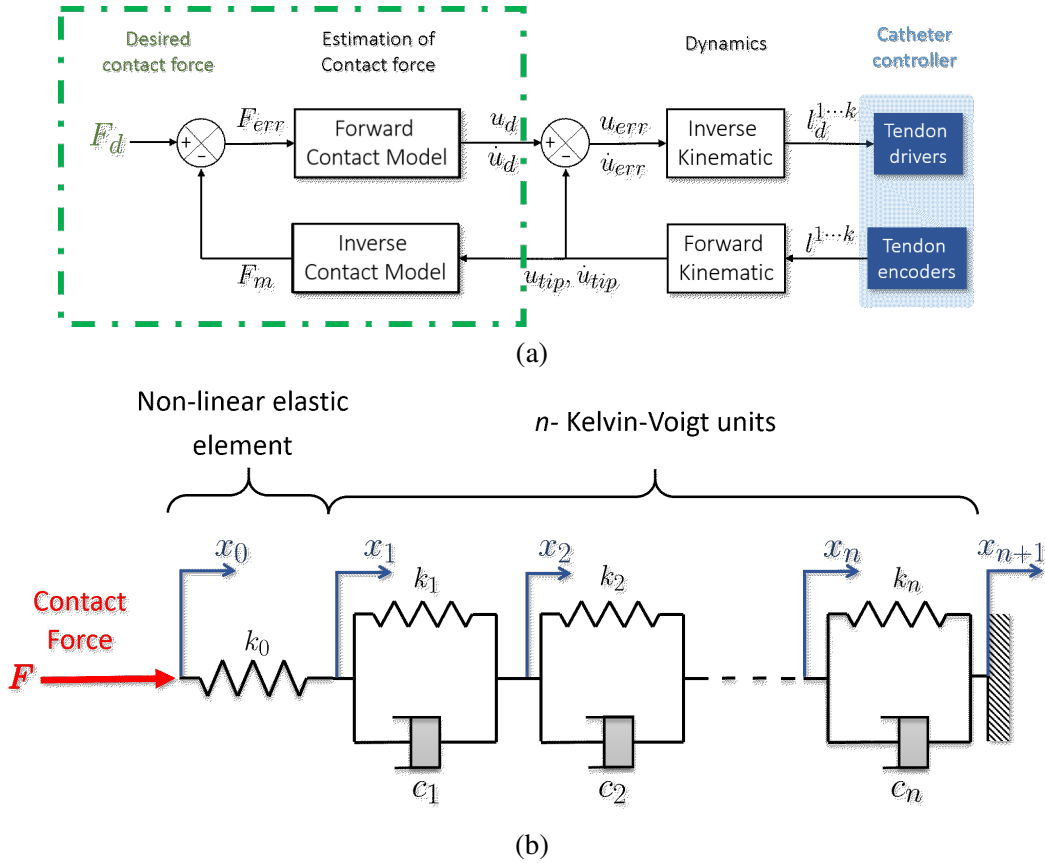
Figure 2.3: (a) high-level control system for maintaining catheter-tissue contact force at a desired level F_d, (b) nonlinear viscoelastic contact model at the catheter-tissue interaction point.

characterization of the viscoelastic properties of soft tissue [164]. In this regard, recently Hooshiar *et al.* [165] have suggested and validated a class of generalized Kelvin-Voigt models for real-time viscoelastic characterization of myocardial tissue. However, this study would improve their principal assumption of linear viscoelasticity aiming in a better accuracy [166, 167, 168].

In the present paper, a nonlinear viscoelastic frictionless contact model was adopted. A generalized non-linear Kelvin-Voigt model was proposed and verified. Furthermore, the implicit formulation was derived, its parameters were identified, the system of equations was solved and experimentally validated. In the following, Sec.2.3 summarizes the modeling, solution schema, parameter identification, model verification, and experimental validation. Sec.2.4 summarize the results and discussion, and Sec.2.5 closes the article with concluding remarks.

2.3   Method

In order to estimate and control the contact force at the catheter-tissue interface, a nonlinear viscoelastic material model of tissue is proposed. Also, both forward and inverse models were formulated and, for each, an implicit solution schema is postulated. Furthermore, model parameter identification, model verification, and validation were performed for an *ex-vivo* porcine atrial tissue model.

Fig.2.3 (a) depicts a conceptual high-level control system for maintaining tissue-catheter contact force at a desired level F_d through driving k tendon lengths, $l^{1\cdots k}$. Labels F, u, and l denote the contact force, tip displacement, and length of tendons, while d, m, and err stand for desired, model estimation, and error, respectively. For the force control system to perform accurately, an accurate and fast contact model is desirable. To this end, a contact model was proposed and validated as follows.

2.3.1   Contact Model

For modeling the contact with tissue, the *n*-unit generalized Kelvin-Voigt (n-GKV) model introduced in [165] was adopted and improved (see Fig.2.3(b)). As depicted in Fig.2.3(b), this improved model incorporates a nonlinear elastic element with parameter k_0 and n serial linear Kelvin-Voigt units with stiffness constants k_i and viscous constants c_i. Also, the inertial effects of the heart wall motion were neglected for the sake of simplicity. The latter assumption is in agreement with the findings in [165] that structural forces dominate the inertial forces at low-frequency heart-beat, e.g. $1 - 2$Hz.

The elastic element was considered as a power-law spring with the force-length equation described by Eq.1.

$$F = -k_0(x_1 - x_0)^p, \tag{1}$$

Similarly and due to the serialization, force balance condition for an arbitrary *i*-th Kelvin-Voigt unit was formulated as:

$$F = -k_i(x_{i+1} - x_i) - c_i(\dot{x}_{i+1} - \dot{x}_i) \quad i = 1, 2, \cdots n, \tag{2}$$

subjected to two homogenous Dirichlet and Neumann boundary conditions:

$$x_{n+1}(t) = 0, \tag{3}$$

$$\dot{x}_{n+1}(t) = 0, \tag{4}$$

and $2n$ initial conditions:

$$\dot{x}_i(0) = 0 \quad i = 1, 2, \cdots n. \tag{5}$$

The model was assumed at initial rest with all the springs and dash-pots at their resting lengths. Using Eq.2 for all i-s, a system of n ordinary differential equations (ODE) with n unknowns was formed and re-arranged in the form of Eq.2.

$$\mathbf{K}x(t) + \mathbf{C}\dot{x}(t) = -f(t), \tag{6}$$

where $\mathbf{K}_{n \times n}$, was the stiffness matrix and, $\mathbf{C}_{n \times n}$ was the viscous matrix, $x(t)_{n \times 1}$ and $\dot{x}(t)_{n \times 1}$ was the displacement and velocity vectors, *a.k.a.* state vectors, and $f(t)_{n \times 1}$ was the force vector. State vectors were defined as:

$$x(t) = [x_1(t), x_2(t), \cdots, x_n(t)]^T, \tag{7}$$

$$\dot{x}(t) = [\dot{x}_1(t), \dot{x}_2(t), \cdots, \dot{x}_n(t)]^T, \tag{8}$$

and force vector was as follows:

$$f(t) = [F(t), F(t), \cdots, F(t)]^T, \tag{9}$$

where $(.)^T$ denotes transpose operator. Also, the elements of stiffness and viscous matrices were obtained as:

$$K_{ij} = \begin{cases} k_i & i = j \\ -k_i & i = j - 1 \\ 0 & otherwise \end{cases} \quad i, j = 1 \cdots n, \tag{10}$$

$$
C_{ij} = \begin{cases} c_i & i = j \\ -c_i & i = j - 1 \\ 0 & otherwise \end{cases} \quad i,j = 1 \cdots n. \tag{11}
$$

2.3.2 Solution Schema

The forward model was solved using a fourth order Runge-Kutta (RK4) method to find x_is where $F(t)$ was known. Consequently, x_0 was obtained using the following re-arranged form of Eq.1:

$$
x_0(t) = x_1(t) + \left(\frac{F(t)}{k_0} \right)^{\frac{1}{p}}, \tag{12}
$$

For the inverse model, the time-history of $x_0(t)$ was assumed as known. However, knowledge of the displacement state $(x(t), \dot{x}(t))$ was necessary for solving Eq.6 for $f(t)$. To this end, the displacement state reconstruction was performed incrementally. Incremental (explicit) form of Eq.6 was obtained as follows, considering a two-term forward difference definition for $\dot{x}(t)$:

$$
x(t + \delta t) = x(t) - \delta t \mathbf{C}^{-1} \left(f(t) + \mathbf{K}x(t) \right). \tag{13}
$$

Since c_is are non-zero and $\mathbf{C}$ is lower-triangular, per Eq.26, $\mathbf{C}$ was unconditionally non-singular; therefore, Eq.13 was unconditionally convergent. Time-step δt was set to 0.005sec in this study. In contrast to the forward model, in the inverse model, each increment initiated with finding the contact force in Eq.1. Substituting $x_0(t)$ from the input and $x_1(t)$ from the last increment solution revealed $F(t)$ in each iteration. $F(t)$ was further used to predict the displacements in the next time instance.

2.3.3 Ex-vivo indentation on porcine atrial tissue

Fig.2.4 shows the experimental setup used for the *ex-vivo* indentation test. A cylindrical probe with a spherical tip and 10Fr ($\frac{10}{3}$mm) outer diameter was 3D printed and used to apply the indentation. The chosen outer diameter resembled the clinically used RFA catheters. A freshly excised porcine heart was used and its left atrium was excised using a surgical 10-blade. It was afterward
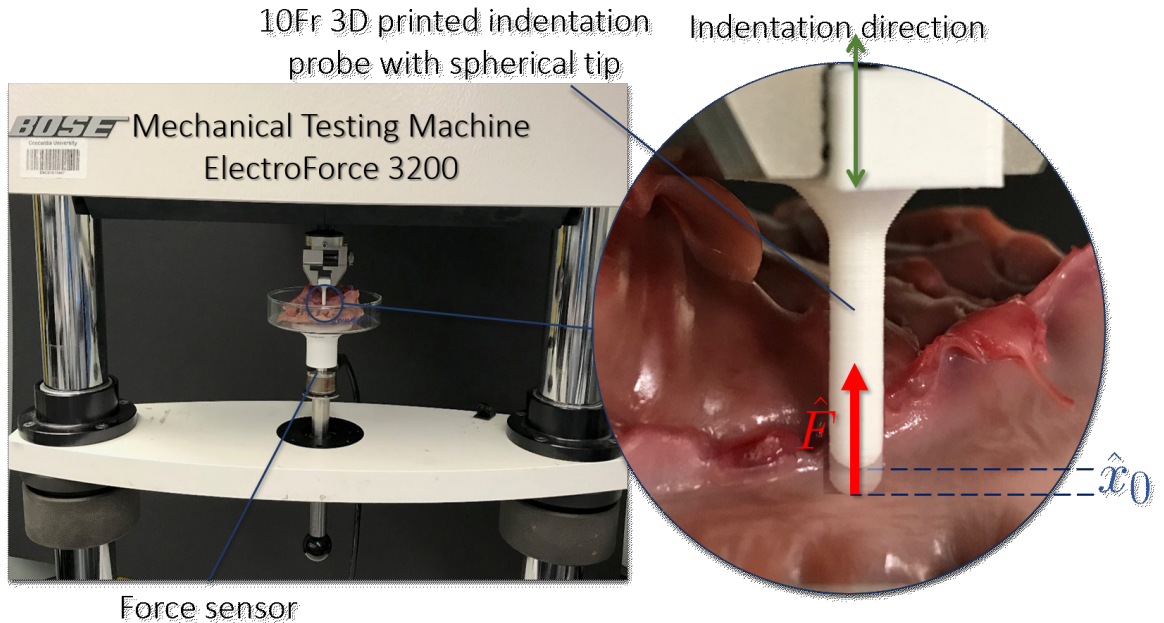
Figure 2.4: Experimental setup for ex-vivo indentation using a 10Fr probe on a porcine atrial tissue.

fixed on a glass plate and placed on the mechanical testing machine. The probe was adjusted to slightly touch the atrial tissue (initial contact force 0.05N).

The test procedure was to apply three consecutive sinusoidal indentations, 20 cycles each, on the tissue under displacement control. The range of the indentations was 2mm with an average of 2mm (2 ± 1mm), while the frequencies of indentations were $1, 1.5$, and 2Hz, consecutively. These frequencies covered the frequency range of normal heart-beat, i.e. $60 - 120$bpm.

2.3.4 Parameter Identification and Model Verification

The proposed n-GKV contact model incorporated a total of $2(n + 1)$ parameters, i.e. $2n$ for k_is and c_is, and two additional parameters of p, and k_0. To reduce the search space for finding the optimized model parameters, the following constraints were imposed. Power-law parameter p was constrained to be larger than 1, to meet the nonlinearity assumption. Also, p was assumed as an odd number so that Eq.1 becomes sign-preserving and compliant to the preservation of energy principle.

In order to select a sufficient n and obtain optimized parameter values, a parameter optimization was performed on the results of the *ex-vivo* indentation test. Eq.14 describes the goal function

Table 2.1: Search-space for the model parameters used for the optimization.

Parameter	Search-space
n[165]	1, 3, 5, 7
p	3, 5, 7, 9
k_0	$\mathbb{R}^+$
k_i	$\mathbb{R}^+$
c_i	$\mathbb{R}^+$

as the difference between the model estimated work and the calculated work from the experiment. The goal function was minimized using a particle-swarm optimization (PSO) algorithm. Optimization was performed utilizing Matlab® R2018a (MathWorks Inc., MA, US). Since PSO is a global optimization method, the resulting parameters were deemed as the global optimums.

$$\min_{n,p,k_0,k_i,c_i} \left\| \int_0^{t_1} F(t)dx_0(t) - \int_0^{t_1} \hat{F}(t)d\hat{x}_0(t) \right\|^2.$$

$$\text{subjected to} \quad \text{Table 2.1}$$

(14)

Model verification was performed by calculating the maximum absolute error E_{max} and root-mean-square (RMS) error of force E_{rms} between the experimental and estimated force of the optimized model.

2.3.5 Model Validation

To validate the optimized model, a dynamic triangular test with a similar range to the sinusoidal test and a frequency of 1.25Hz (75bpm) was performed on another spot with 5mm distance to the original spot. Similar to the verification test, E_{max} and E_{rms} were used to assess the model performance.

2.4 Results and Discussion

To find the optimized model parameters for a valid contact model, a dynamic indentation test on a freshly excised porcine atrial tissue was performed. Fig.2.5(a) shows the displacement of probe-tip $\hat{x}_0$, during the *ex-vivo* test. Also, it depicts a comparison of the measured contact force $\hat{F}$ and model-estimated contact force F.

31

Model Verification Results
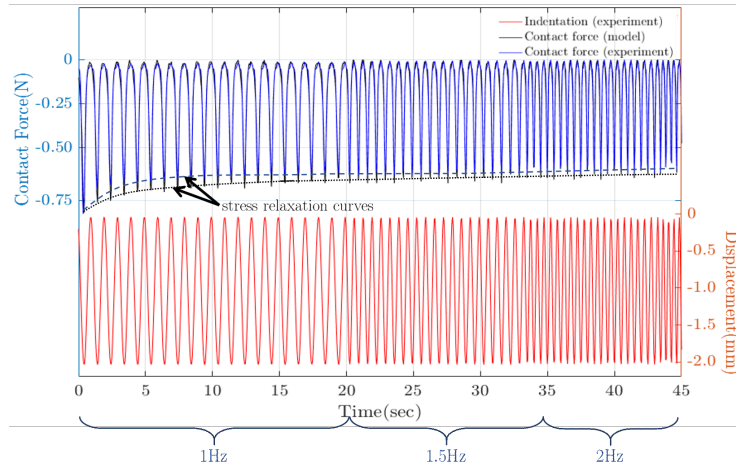
(a)

Minimum force estimation error vs. n, and p
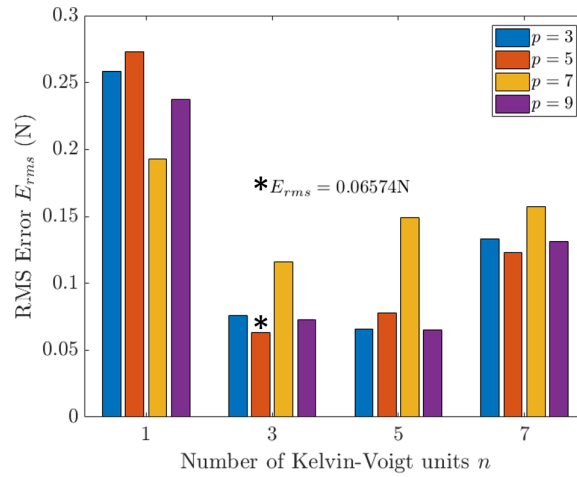
(b)

Figure 2.5: (a) comparison of the contact force and displacement measured during *ex-vivo* experiment (blue) and from the optimized contact model, (b) change in the optimization landscape for E_{rms} with respect to the number of Kelvin-Voigt units n, and power of the nonlinear elastic element, p.

The optimization process was performed on a Windows® PC, equipped with a 3.3GHz CPU and 32GB of RAM. Also, with the use of 200 parallel threads, the optimization time decreased significantly. Total computation time for finding the optimized model was 850msec and for estimating the contact force using the optimized model was 5msec. Considering the fact that finding the optimized model is needed only once for a specific ablation spot, results suggest that the proposed model and solution schema are fast-enough for RFA procedures. Table 2.2 summarizes the computation time break-down.

Table 2.2: Break-down of the computation time.

Procedure	Computation-time (msec)
Model optimization	850
Displacement acquisition (per time-increment)	5
Force estimation (per time-increment)	5

Contact force F was estimated using the optimized contact model. As Fig.2.5(b) depicts, PSO minimization indicated the best force estimation was obtained with $n = 3$ and $p = 5$. RMS-error of force-estimation with this model was $E_{rms} = 0.06574$N and maximum absolute error $E_{max} = 0.09144$N. As Fig.2.5(b) indicates, RMS-error decreased by increasing the number of K-V unites from 1 to 3, however models performed worse by further employing K-V units, i.e. $n = 7, 9$. Such a trend has previously been reported in [165] and is known as associated with the over-fitting and error accumulation.

As for the power-law parameter p, not a specific trend of change in the error was observed. In the process of finding the best performing model, the same order of RMS-error was observed with $(n = 3, p = 5)$, $(n = 5, p = 3)$, and $(n = 5, p = 9)$. However, considering the fact that larger n would result in a larger and more complicated model, the 3-GKV model with $p = 5$, i.e. $(n = 3, p = 5)$ was selected as the optimal model. Table2.3 summarizes the optimum parameters associated with the optimal contact model.

Considering the acceptable level of errors, i.e. E_{rms} and E_{max}, in model estimations and the

Table 2.3: Optimized model parameters for 3-GKV,

	$k_0(\frac{N}{mm})$		
	0.2212		
$n = 3$	$k_1(\frac{N}{mm})$	$k_2(\frac{N}{mm})$	$k_3(\frac{N}{mm})$
$p = 5$	0.5476	0.4713	0.7032
	$c_1(\frac{Ns}{mm})$	$c_2(\frac{Ns}{mm})$	$c_3(\frac{Ns}{mm})$
	15.9645	9.5157	1.7820

ability of the model to capture the stress relation phenomenon verified the utilization of the optimized 3-GKV model.

In addition, Fig.2.6(a) depicts the results of the validation test with triangular indentation test. Similar to the verification test, results of the optimal model were in fair agreement with experiment. Maximum absolute error E_{max} was 0.1141N and RMS-error E_{rms} was 0.0544N. Further error analysis revealed that the average absolute error was 0.0520 ± 0.0662. It also showed that error $F - \hat{F}$ had a normal distribution around its average. Also, from the fact that the average error is positive, it is inferred that the proposed model overestimated the contact force by a maximum percentage of nearly 15%. However, further investigation revealed that the maximum overestimation occurred at near-zero displacements. The model predicted the maximum contact force with an acceptable error ($E_{rms} < 5\%$). Fig.2.6(b) depicts the distributions of error and its associated normal fit.

2.5   Conclusions

In this study, initially a control system for displacement-based force control of the steerable RFA catheters was conceptualized. The proposed system necessitated utilization of a valid and accurate yet fairly fast and simple contact model for the catheter-tissue contact model. to this end, an $n-$ generalized Kelvin-Voigt viscoelastic model was proposed. The proposed model was formulated for both direct and inverse model solution modalities and the model parameters were optimized using the particle-swarm optimization (PSO) technique.
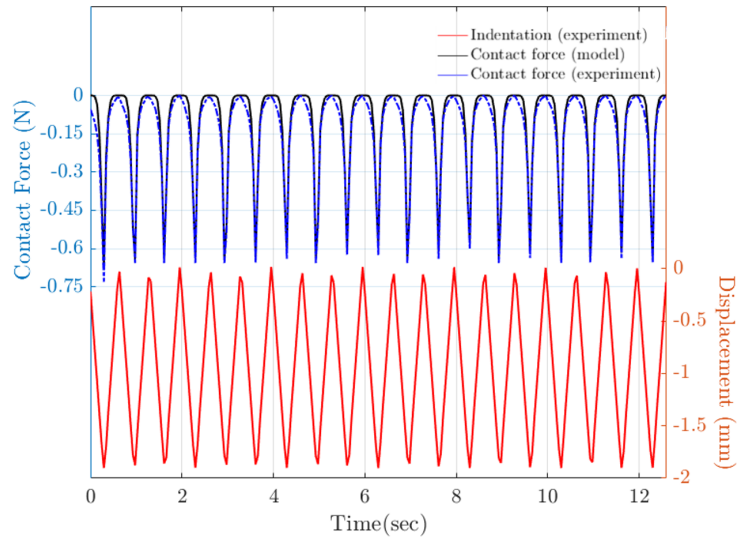
(a)
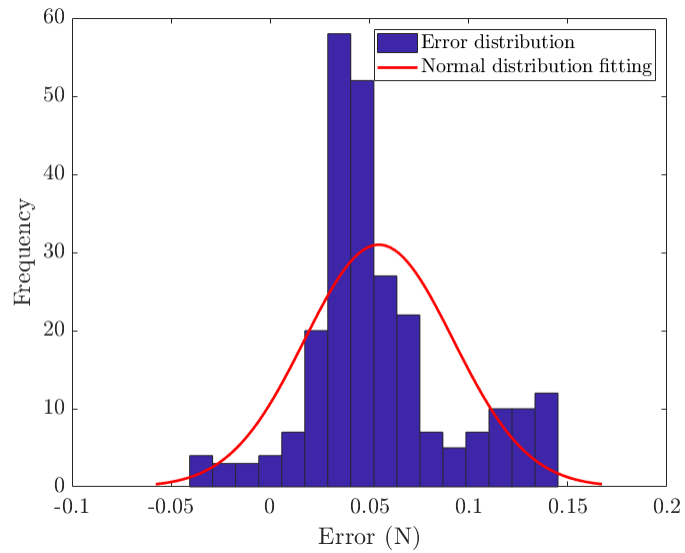
(b)

Figure 2.6: (a) results of contact force estimation for the model validation, (b) raw and fitted distribution of error between experiment and model estimation for the validation test.

Both verification and validation studies revealed low computational surplus for the proposed solution schema. Furthermore, model estimations were in fair agreement with experiments. Therefore, author would consider the postulated contact model and its associated solution schema as reliable-enough for utilization in the proposed force control system.

In addition, utilization of the energy goal-function guaranteed that the energetic behavior of the model replicates that of the tested tissue. Since stress-relaxation is an energy drift mechanism, one would suggest the agreement of model stress-relaxation with the experiment as a supporting evidence.

This study was the first step towards the model-based control of the contact force during RFA procedure. Author would suggest further exploration of the frequency response of the model with that of the tissue. Also, the combination of a series of indentation tests on the tissue with various depth and wider frequency-range, e.g. chirp, would be another improvement of this study.

Chapter 3

Toward Task Autonomy in Robotic Cardiac Ablation: Learning-based Kinematic Control of Soft Tendon-driven Catheters

3.1   Abstract

The goal of this study was to propose and validate a control framework with level-2 autonomy (task autonomy) for the control of flexible ablation catheters. To this end, a kinematic model for the flexible portion of typical ablation catheters was developed and a 40mm-long spring-loaded flexible catheter was fabricated. The feasible space of the catheter was obtained experimentally. Furthermore, a robotic catheter intervention system was prototyped for controlling the length of the catheter tendons. The proposed control framework employed a support-vector-machine classifier, to determine the tendons to be driven, and a fully-connected neural network regressor to determine the length of the tendons. The classifier and regressors were trained with the data from the feasible space. The control system was implemented in parallel at user-interface and firmware and exhibited 0.4s lag in following the input. The validation studies were four trajectory tracking and four target

37

reaching experiments. The system was capable of tracking trajectories with an error of 0.49 ± 0.32mm and 0.62 ± 0.36mm in slow and fast trajectories, respectively. Also, it exhibited sub-millimeter accuracy in reaching to three pre-planned targets and ruling out one non-feasible target autonomously. The results showed improvement compared to the recent literature.

3.2 Introduction

3.2.1 Background

Catheterization has become the standard-of-care for the treatment of cardiac atrial fibrillation (AFib) [169]. AFib causes cardiac arrhythmia and is the most common cardiology reason for hospitalizations [169]. Inactivating the cardiac cells which cause the arrhythmia by heating, i.e., radio-frequency ablation (RFA), or freezing, cryo-ablation (CRA) are the well-established options interventions with catheter-based techniques to treat the AFib. Fig. 3.1 depicts the catheter-based intervention for cardiac ablation schematically. For this treatment, a long thin and flexible catheter, on the tip of which a burner or freezer unit is embedded, is used. The catheter is surgically inserted into the patient's femoral vein and is steered toward the right or left atrium. Once the tip of the catheter is inside the atrium and in contact with the desired location on the atrial wall (usually medial and posterior walls), the surgeon turns on the radio-frequency pulse generator for burning (ablating) the cells.

 The pulse generating cells are mainly scattered on the posterior and medial wall of the atria. Therefore, the surgeon needs to manipulate the tip of catheter from its handle outside the body to reach multiple spots inside the atria for burning enough cells to manage the AFib favorably.

Maintain stable contact between the tip of the catheter and the atrial wall is challenging due the motion of the heart [31]. Also, the blood flow in the atrium may displace the tip of catheter, unless it is in secure contact with the wall. Studies have shown that to obtain optimal treatment, maintaining the contact force in the range of 0.2 ± 0.1 N is crucial [19, 31]. Whereas the excessive force would puncture the cardiac wall and insufficient force would lead to an ineffective treatment [31].

Another factor challenging the success of RFA, is that the surgeon merely relies on the 2D visual
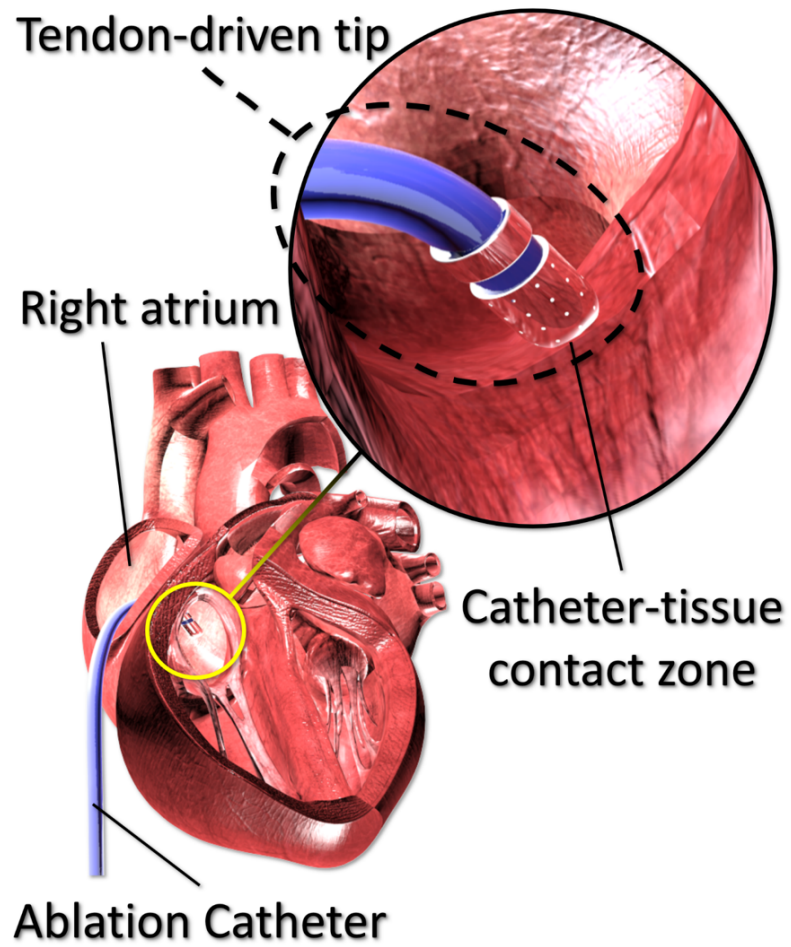
Figure 3.1: Intra-cardiac intervention procedure.

feedback of the catheter shape obtained from the X-ray fluoroscopy. Whereas, in open surgery surgeon has both visual and tactile feedback on the surgical site. In this regard, a recent study has shown that the surgeon's tactile perception happens three times faster than the visual perception in cardiovascular interventions [170]. Therefore, the surgeon's situational awareness is limited during the RFA procedure due to the compromised sense of touch and variability of the contact between the catheter and the cardiac wall [19].

For more robust and dexterous manipulation of the catheters inside the atria, tendon driven catheters were developed. A steerable catheter is comprised of a shape-controllable tip portion (4–10 cm), a non-steerable body (80–150 cm), and a control handle. The handle typically has a knob mechanism to wind/unwind the tendons which are internally connected to the tip portion. Usually, the steerable catheters are single- or double-curved, depending on the number of curves their tip portion could possess [79]. The steerable catheters have enhanced the surgeon's ability in establishing and maintaining contact between the catheter and atrial wall. Also, thanks to the high maneuverability of catheters, accessing the inferior and posterior wall of the atria has become possible [79].

Despite the advantages of the steerable catheters, precise manipulation and targeting inside the dynamically moving atria is still a challenge. As an option, the robotic catheter intervention (RCI) systems have added unprecedented dexterity and precision to the electrophysiologic intervention [19]. The currently available RCI systems, such as Sensei and Magellan Robotic System (Auris Health, CA, USA), provide robotic catheter manipulation with level-0 (no autonomy) and level-1 (robot assistance) autonomy. A detailed definition of the levels of autonomy is provided in [171].

3.2.2 Motivation and contributions

With the current RCI technology, maintaining the tip of the catheter in constant contact with the atrial wall is a surgical task that needs repeated correction of the tip position by the surgeon through the master module of the RCI. This has been reported to be cumbersome and increasing the cognitive load of the surgeon [19, 172]. Therefore, an RCI system with level-2 autonomy (task autonomy) capable of autonomous tip position control of the catheter for establishing and maintaining contact with the atrial wall is favorable.
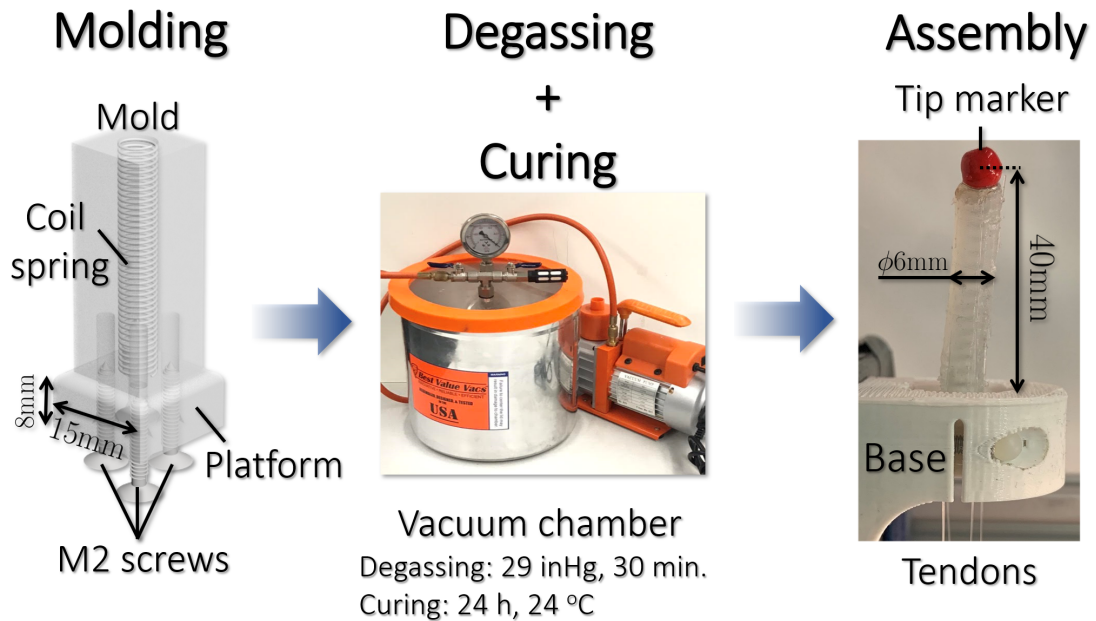
Figure 3.2: Molding, degassing, curing, and assembly steps for prototyping the flexible catheter *MiFlex*.

With the task autonomy, the surgeon would determine the position of the catheter tip (for example from a previously 3D map of the heart) and the robot would control the shape of catheter to reach the target position. Also, the surgeon would be monitoring the maneuver of the robot and interfere if the need would be. A similar control schema has been proposed in [126] for extra-cardiac needle insertion.

In the present study, an inverse kinematics-based schema for the position control of the tip of a tendon driven catheter was proposed and validated. The catheter was custom-designed and fabricated with a four-tendon actuation mechanism. The main contribution of the proposed schema was that it was based on a nonlinear learning-based (artificial neural network) inverse kinematics. Such a learning-based approach would allow for implementing the control schema with low computational surplus, which is a well-known limitation of the mechanistic models, e.g. continuum mechanics-based models [19]. Also, it would allow for intrinsic compensation of internal friction and backlash, as the learning-based model would be trained by the actuation data from the catheter prior to the task performance. In practice, since the catheters are single-use, such a model training (a.k.a calibration) can be automatized as a part of the system setup.

Another challenge was to resolve the redundancy of the catheter actuation. The catheter tip had two degrees-of-freedom (DoF) in the task-space while it had four actuation DoFs (one DoF for each tendon). Such a configuration made the catheter over-actuated and actuation redundant. Utilizing a learning-based classifier, and by limiting the number of tendons to be simultaneously driven to only two, the redundancy was resolved and the catheter model was incrementally treated as a fully-actuated system.

Based on the favorable validation results, the proposed learning-based kinematic model and feed-forward position control would provide a low-maintenance, fast, and accurate alternative to the currently available model-based and sensor-based control schema. To model and control the steerable catheters, researchers have adopted continuum mechanics [173], differential geometry [174], particle-based [112, 175, 176], and multi-body dynamics [163, 150] approaches. In the following a review of the pertinent studies is presented.

3.2.3 Related studies

The previous research on modeling the dynamics and kinematics of flexible catheters can be categorized as mechanistic and heuristic (statistical) models. As for the mechanistic models, previous studies have modeled the deformation of flexible catheters under external load with [66] and without [173] internal tendon actuation. Theoretically, a flexible catheter has infinite DoFs. However, for simplification, the catheter shape of the catheter has been modeled as a curve [174, 177, 150, 107] with a finite number of DoFs, or a set of small rigid segments with flexible joints [101, 178, 163, 179, 180]. In the curve-based models, the piecewise constant curvature (PCC) has been widely adopted [163]. Despite its wide adoption, the PCC assumption needs validation in each study. Since the mechanistic models often involve simplifying assumption on the catheter shape or the external loading, intrinsic nonlinearities such as dead-zones, friction, slack of the tendons, and material nonlinearities (e.g., hyperelasticity) are usually neglected. Tendons can support merely tension but not compression. Therefore, tendon slacking is a common phenomenon observed in tendon-driven catheters. To compensate for the slack, researchers have used symmetric agonist-antagonist tendon configurations [64, 79]. The backlash caused by the tendon slack is a source of nonlinearity and must be compensated. Also, high tension in tendons results in non-negligible friction [46, 181] and

tendon elongation. Considering such nonlinearities in the mechanistic models, such as Cosserat's rod model [174, 177, 182, 183] would complicate the model and incur high computational cost, especially for inverse kinematics, e.g. [184, 185, 186, 187].

On the other hand, heuristic models such as Gaussian Mixture Models (GMM) and neural networks (NN) have shown to be a favorable option for realtime applications as offer a low computational cost and the ability to capture the nonlinear effects such as dead-zone and friction [19]. In an early study, Rafii-Tari *et al.* [188] utilized a GMM to obtain the kinematics of catheter maneuvers in an RCI setup. In another effort, Khoshnam *et al.* [189] proposed a Gaussian Mixture Model to estimate the external force on RFA catheters using curvature analysis. Recently, Chi *et al.* [190] encoded the catheter kinematics in a GMM model and used it for kinematic control of catheters. Although GMMs offer the inclusion of nonlinearities, such models need rigorous data preparation. Neural networks, as another heuristic option, were first used to acquire the kinematics of soft robots for compensating for the material nonlinearities [191]. Giorelli *et al.* utilized a neural network for obtaining the kinematic Jacobians [192] of a soft robot in realtime. Neural networks have also been employed as a look-up table for obtaining the kinematics of soft robots obtain from other methods, e.g., finite element method [193] for realtime applications. A comprehensive methodological review of the methods on the taxonomy of steerable catheters and the modeling techniques can be found in [79] and [19], respectively. Generally, in tendon-driven catheters, the tip is connected to a series of parallel tendons which are aligned with the catheter's body and at the other end, are connected to motors. The motors change the length of the tendons that consequently change the position and orientation of the tip. For quasi-static applications, i.e., where the intertial effects are negligible due to slow maneuvers or low ratio of external forces to the weight of the catheters, the kinematic modeling is favorable. In kinematic models, the aim is to map the change of the length of the tendons (joint-space) to the changes of the tip pose (task-space) [68, 56, 194].

In the following first a kinematic model of a tendon driven catheter is proposed and validated. Afterward, the overview of the RCI robotic system developed for the experiments is described. Furthermore, the details of the tendon selection classification, NN-based inverse kinematics, and the proposed catheter position controller are presented. In the end, the results of the validation studies on assessing the performance of the hypothesized level-2 autonomy in an *ex-vivo* setup will

1. Base plate
2. Microprocessor and motor drivers (x2 Arduino Uno)
3. Potentiometers (x4)
4. USB Cameras (x2 C920 Logitec)
5. Stepper motors (x4 200 PPR)
6. USB cables to PC
7. Aluminum frame
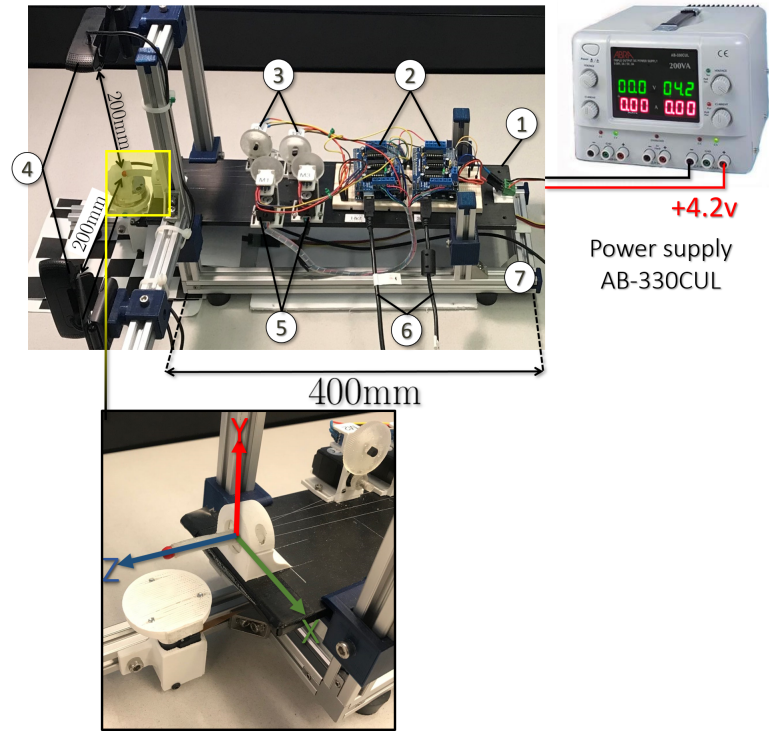
(a)
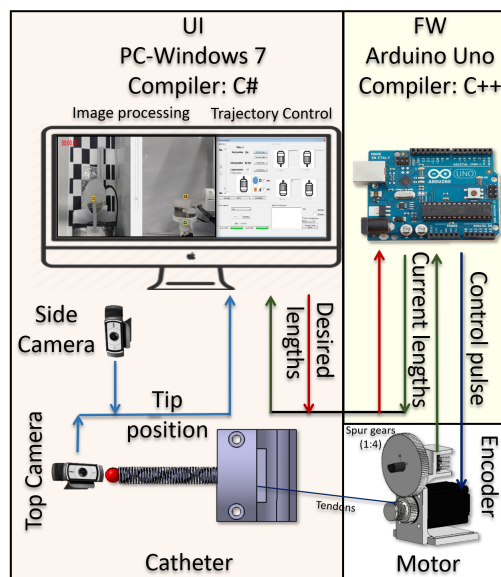
(b)

Figure 3.3: (a) components of the mechanical and electrical modules in the prototyped RCI device, and (b) software architecture of the user interface (UI) and firmware (FW).

44

be discussed, followed by the concluding remarks.

3.3 Material and Methods

In this section, an overview of the catheter fabrication and the RCI mechanism used in this study is provided. Afterward, the theoretical workspace of the catheter based on the constant bending radius assumption is obtained and its validity is investigated by experimental comparison. Furthermore, the proposed learning-based forward and inverse kinematic model of the catheter is described and the accuracy of those are investigated. In the end, the experimental tests procedures and setups for studying the performance of the proposed trajectory tracking are described.

3.3.1 Catheter fabrication and assembly

The prototyped catheter in this study, named as *MiFlex*, is a tendon driven catheter with four inextensible tendons. Fig. 3.2 shows the fabrication steps and final the size and assembly of the catheter. The selected dimensions for the catheter prototype was 6 mm in diameter and 40 mm in length. The selected diameter was to replicate an 18-Fr ($1Fr = \frac{1}{3}$ mm) catheter and 40 mm length was according to [195, 196] for the average transversal diameter of the right atrium in adults diagnosed with AFib.

For the fabrication, a cylindrical mold was rapid prototyped with a 3D printer (Replicator+, Maker-Bot, NY, USA). Also, a square platform ($16 \times 16 \times 8$ mm), housing four through holes, was 3D-printed to provide a platform for the fixed end of the catheter. The through holes were used to accommodate anchorage M2 screws for fixing the mold to the platform and later were used as guides for the four tendons.

The catheter was comprised of a steel compression coil spring with a nominal outer diameter of 5 mm and a compressive stiffness of 0.35 $\frac{N}{mm}$. The spring was installed at the center of the cylindrical mold while silicon rubber material for the body of the catheter (Ecoflex™ 00-20, Smooth-on Inc., PA, USA) was filled in the mold. The use of coil spring would enhance the ability of the catheter to recover to its original shape by compensating for the viscous energy damping in the rubber material. After filling the mold, it was rested still in a vacuum chamber (Best Value Vacs, IL, USA) under
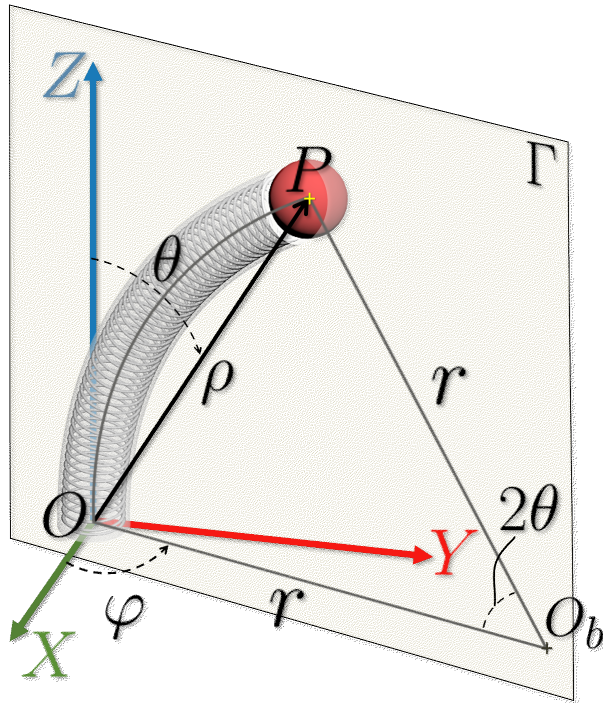
Figure 3.4: Representative deformed shape of the catheter with constant bending radius.

29 mmHg vacuum pressure for discarding the air bubbles (degassing). Furthermore, the degassed mold was rested for 24 hours at $24°C$ for final curing. After curing, the platform was secured in a 3D-printed base. The reason for the base was to make the assembly modular and facilitate the replacement of the catheter and base. In practical cases, the catheter would be a single-patient use disposable thus such a modular design could help in replacing the catheter.

3.3.2 RCI system overview

At the system level, the RCI system in this study was designed with three modules, i.e., mechanical, electrical, and software modules. Fig. 3.3(a) shows the components of the prototyped RCI system. Four independent stepper motors, identified as M_{1-4}, were used to control the length of the tendons, i.e., L_{1-4}. The motors were controlled using two independent stepper motor drivers stacked on two ATMEGA microprocessor (Uno, Arduino Co., MA, USA). Each microprocessors was also connected to two potentiometers (as rotary encoders) to measure the angle of the shaft of the motors.

Fig. 3.3(b) depicts the software architecture used for the feedback control of the motors, trajectory error estimation, and data storage. The software was composed of two components: the user interface (UI), running on the PC, and the firmware (FW), and loaded on the microprocessors. The UI was used to acquire the user inputs, i.e., the desired trajectory and the target within the workspace. The FW role was to receive the desired tendon lengths from UI and relaying the current tendon lengths back to UI. The control framework, described in Sec. 3.3.3, was implemented in the FW (low-level implementation) and the trajectory generation and task-space to joint-space mapping (inverse kinematic) were implemented in the UI (high-level implementation). Also, for validation purposes, the trajectory of the tip marker (red sphere at the tip of the catheter) was tracked in realtime using the two USB cameras (800×600 pixels resolution, model C920, Logitec, Lausanne, Switzerland) with a stereo-calibration adopted from [197, 198]. The stereo-vision verification on a chess-board template (depicted in Fig. 3.3(b)) showed an error of ± 0.26 mm in detecting the corners of the squares in the template. It is noteworthy that the position feedback from the camera tracking served merely as a reference and was not used in the control framework.

3.3.3 Control framework

In order to enable the RCI system to exhibit task autonomy for trajectory following tasks, the presented control system in 3.5 was proposed. The control goal was to attain and hold a given desired position, $P^\star$ in the task-space (global Cartesian) through changing the length of tendons. For the user's intuitive inference, the choice of Cartesian task-space was favorable. However, the kinematics of the catheter were less complicated in spherical coordinates thus a mapping $\mathfrak{M} : \mathrm{R}^3 \to \mathrm{R}^2$ from Cartesian to spherical coordinates was used. Afterward, the control system would determine the desired length of a set of tendons (control state) by which the tip of the catheter would reach $P^\star$. The proposed control framework is a feed-forward system. The utilization of an internal motor shaft position feedback in the motor drivers M_{1-4} ensures that the desired tendons lengths are attained. The same technique has been successfully implemented in [185]. Such a control framework necessitated a mapping between the desired kinematic state in task-space $(\theta^\star, \varphi^\star)$ and the joint-space variables $L_{1-4}^\star$. Such a mapping constituted an inverse kinematic problem. Mechanistic modeling
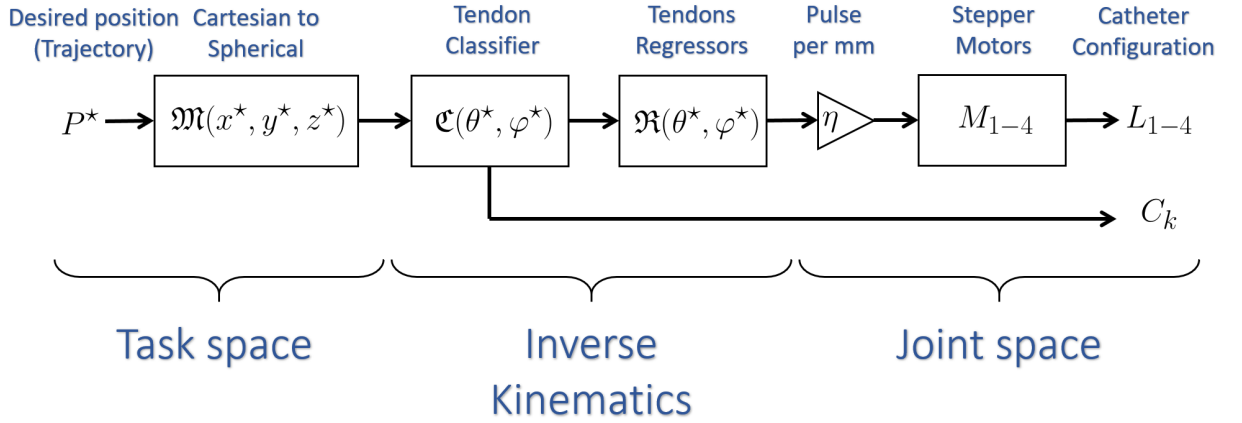
Figure 3.5: The proposed learning-based feed-forward control system for position control of the tip of the catheter.

of the problem involves nonlinearities such as material nonlinearity, internal friction between the tendons and the body of the catheter, and tendon slacking. As an alternative to the mechanistic approach, the inverse kinematic problem was divided into learning-based classification and regression problems. For a given desired position $P^\star$, the classifier, i.e., $\mathfrak{C}(\theta^\star, \varphi^\star)$ would determine tendon(s) to be pulled, while the regressor would determine length of the said tendon(s) (desired lengths). Therefore, the objective of the inverse kinematics would be to determine the catheter configuration, i.e. $(C_k : i - j, L_i, L_j)$ in joint space, for a given desired position $P^\star$ in the task space.

3.3.4 Inverse kinematics

Degrees of freedom

Fig. 3.4 depicts a representative deformation of the catheter, where the Cartesian coordination system $\begin{pmatrix} X & Y & Z \end{pmatrix}^T$ represents the fixed global frame, P is the position of the tip of the catheter, i.e., the center of the red tip marker marked by the bright +), r is the bending radius, Γ is the bending plane, and O_b is the center of the bending arc $\widehat{OP}$.

Due to the relatively larger longitudinal stiffness compared to the bending stiffness, the compression of the catheter along its spine was neglected. Therefore,

48

$$\left|\widehat{OP}\right| = 2r\theta = 40\text{mm} \qquad \text{constant.} \tag{15}$$

Also, $\vec{P} := \vec{OP}$ was presented in the global Cartesian coordinates and spherical coordinates as

$$\vec{P} = \begin{pmatrix} x & y & z \end{pmatrix}^T \quad \in S^+, \tag{16}$$

and

$$\vec{P} = \begin{pmatrix} \rho & \theta & \varphi \end{pmatrix}^T \quad \in S^\circ, \tag{17}$$

where, $S^+ \in \mathrm{R}^3$ and , $S^\circ \in \mathrm{R}^3$ are the Cartesian and spherical representation of the working space (surface) of the catheter, and $\rho \in \mathrm{R}$, $\theta \in [0, \pi]$, and $\varphi \in (-\pi, \pi]$. The mapping from the Cartesian coordinates to the spherical and its *versa* were obtained as:

$$\begin{pmatrix} \rho \\ \theta \\ \varphi \end{pmatrix} = \begin{pmatrix} \sqrt{x^2 + y^2 + z^2} \\ \arccos\left(\frac{z}{\sqrt{x^2+y^2+z^2}}\right) \\ \arctan 2(y, x) \end{pmatrix}, \tag{18}$$

$$\begin{pmatrix} x \\ y \\ z \end{pmatrix} = \begin{pmatrix} \rho \sin\theta \cos\varphi \\ \rho \sin\theta \sin\varphi \\ \rho \cos\theta \end{pmatrix}, \tag{19}$$

where, $\arctan 2(y, x)$ is the two-parameter non-singular tangent inverse function defined as

$$\arctan 2(y, x) = \begin{cases} 2\arctan\left(\frac{y}{\sqrt{x^2+y^2}+x}\right) & x > 0 \\ 2\arctan\left(\frac{\sqrt{x^2+y^2}-x}{y}\right) & x \leq 0, y \neq 0 \\ \pi & x < 0, y = 0 \end{cases} \tag{20}$$

Since the single plane bending condition necessitates $O_b \in \Gamma$ and given that $\overline{O_bO} \perp \widehat{OP}$, O_b would unconditionally remain on the XY-plane throughout the bending. Also, in $O\overset{\triangle}{O_b}P$,

$$\rho = 2r\sin\theta. \tag{21}$$

Substituting r from Eq. 15 in Eq. 21, yields the following kinematic constraint between ρ and θ:

$$\rho\frac{\theta}{\sin\theta} = 40\text{mm} \quad \text{constant.} \tag{22}$$

In fact Eq. 22 describes the locus of the theoretical workspace of the tip of catheter in terms of the spherical coordinates ρ and θ. Moreover, it shows that the workspace is independent of φ. Given that O_b coincides on the $z = 0$ plane, the workspace would necessarily be axisymmetric with respect to Z-axis.

Fig. 3.6(a) depicts the theoretical workspace of the catheter at various θs. The shape of the constructed workspace is in accordance with the experimental findings in other studies, e.g., [107, 136]. Another deduction of Eq. 22 was that the minimum number of independent coordinates to fully describe the catheter tip position were (ρ, φ) or (θ, φ). Therefore, the catheter had two degrees of freedom. Fig. 3.6(a) depicts the feasible workspace of the catheter overlaid on the theoretical workspace. The feasible workspace of the catheter was obtained by sequentially pulling the tendons in all the possible dual tendon configurations, labeled as tendon classes $C_1 : 1 - 2, C_2 : 2 - 3, C_3 : 3 - 4, C_4 : 4 - 1, C_5 : 2 - 4, C_6 : 3 - 1$. To obtain a complete feasible space, for each $C_k : i - j$, tendon i would increment for 1 mm (up to 10 mm) while tendon j would complete a 10 mm sweep. Meanwhile, the position of the tip of the catheter was tracked using the stereo cameras.

Tendon selection: support-vector-machine classification

It was observed that for a given point in the feasible space, the tendon configuration might not be unique. In other words, for some points in the feasible region, multiple combinations of tendons and lengths would lead the tip of the catheter to a similar position. Such circumstances defined a
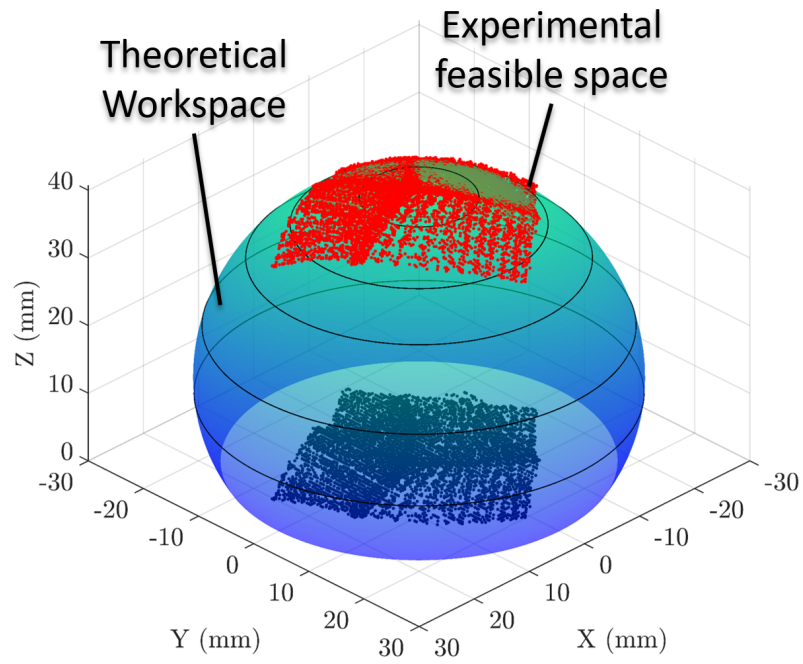
(a)
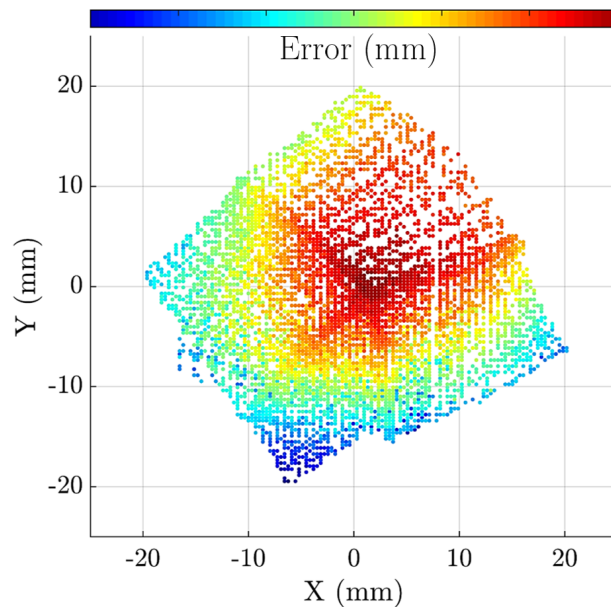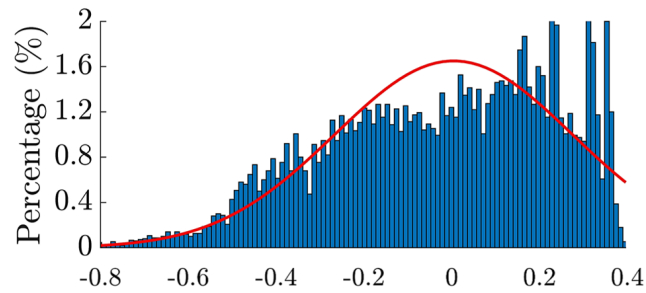
(b)

Figure 3.6: (a) comparison of the theoretical workspace and the feasible workspace of the catheter, and (b) the distribution of the minimum distance between the experimental tip positions and the theoretical workspace.

redundant control space that needed to be resolved. The redundancy was resolved by selecting the tendon classes C_{1-4}. The selection was performed based on the obtained subspaces for C_ks (Fig. 3.7 (a)), such that the least overlap would be observed.

Afterward, a support vector machine (SVM) classifier with a linear kernel was trained with θ and ϕ as the features and $C_1 - 4$) as the categories. The dataset of the feasible space, containing the spherical coordinates of the feasible space ($n = 16100$), was divided into training and validation data with a $70 : 30$ ratio. The model training and validation was performed using Matlab Classification Toolbox (Matlab R2019b, Mathworks, MA, USA). Fig. 3.7 depicts the features space of the training data, the contour of the classified subspaces on XY-plane, and the confusion matrix of the SVM classification. With adopting the accuracy metric defined as

$$accuracy = \left(1 - \frac{\sum \text{off-diagonal components}}{\sum \text{all components}} \right) \times 100, \tag{23}$$

the accuracy of the classifier for tendon class prediction was estimated as 97.3%.

Tendon length estimation: neural network regression

In the control framework, the next step was to determine the desired length of each tendon through neural network regression. To this end, four individual neural networks, denoted as NN_k, ($k = 1 \cdots 4$), were trained with the classified $(\theta, \varphi)^T$ as input and $(L_i, L_j)^T$ as output for the four tendon classes, i.e., $C_k : i - j$. In addition to the input and output layers, each NN_k network had ten hidden layers (with five neurons each) with fully connected architecture. The training was performed using the damped least-square method, a.k.a. Marquard-Levenberg algorithm in Matlab Neural Network ToolBox (Matlab R2019b, Mathworks Inc., MA, USA). Similar to the classification, the dataset was divided with $70 : 30$ ratio for training and validation, respectively. Table 3.1 summarizes the adjusted goodness-of-fit (adj-R^2) and error of prediction for each NN_k.

Figure 3.7: (a) Feature space constructed by θ and ϕ. The figure shows that at relatively large θ, ϕ determines the choice of tendon class, (b) the contour of the classified feasible space on XY-plane, and (c) confusion matrix for tendon class prediction resulting from the validation data ($n = 4830$).

Table 3.1: Goodness-of-fit (adj-R^2) and average percentage of prediction error ($\bar{E}_\%$) for the neural networks NN_{1-4}.

| $C_k:$ | adj-R^2 | | $\bar{E}_\%$ | |
$i-j$	L_i	L_j	L_i (mean $\pm$ SD)	L_j (mean $\pm$ SD)
$NN_1: 1-2$	0.97	0.97	3.1 ± 0.5	3.5 ± 0.4
$NN_2: 2-3$	0.99	0.94	2.8 ± 0.4	4.2 ± 0.3
$NN_3: 3-4$	0.94	0.98	4.4 ± 0.6	4.7 ± 0.6
$NN_4: 4-1$	0.97	0.98	3.6 ± 0.2	4.3 ± 0.3

Control loop implementation

A robotic system with level-2 autonomy should keep the surgeon in the control loop for supervisory privileges, i.e., task initiation and termination, and trajectory selection. To meet this requirement, the proposed control framework was implemented in the user interface (UI) software using object-oriented and multi-thread programming techniques. In order to increase the computational efficiency of the control loop, the SVM classifier $\mathfrak{C}(\phi^\star, \varphi^\star)$, four neural networks NN_{1-4}, and trajectory update loop were implemented in parallel. Thanks to the parallelization, the control loop in UI exhibited an average refresh-rate of 164 ± 12Hz. Also, at the microprocessor level, the refresh-rate of the tendon length control loop was set to 1 kHz.

3.4 Experimental Validation

Experiment I: trajectory tracking

To study the performance of the proposed position control framework, the system was tested in tracking four desired trajectories. The trajectories were of circular, triangular, infinity sign, and spiral shapes and were denoted by $T_\circ, T_\triangle, T_\infty, T_\partial$, respectively. Also, two time periods of 5s and 10s per repetition were set to simulate slow and fast tasks, respectively. Each trajectory was repeated ten times at each speed. The trajectories were defined in preprocessing with fifty intermediary points in the Cartesian task-space such that the XY-projection of the intermediary points would be within the XY-projection of the feasible workspace (Fig. 3.6(b)). Coding lines to define the trajectories

are presented in Appendix A.

Each trajectory was tested in an individual test session such that the test sessions would include ten repetitions of the slow tasks followed by ten repetitions of the fast task. During the tests, the UI would update the desired position $P^\star$ on-line according to the temporal sequence of the intermediary points in each trajectory and the control loop would solve the inverse kinematics for each of the intermediary points in realtime. As a reference for comparison, the position of tip of the catheter was tracked with the stereo cameras during the tests.

Fig. 3.8 depicts the desired and experimental trajectories demonstrated by the proposed RCI system and Table 3.2 presents the performance of the control system in terms of root-mean-square (RMS)-error (average of five repetitions), error range, and time-lag in the fast and slow tasks for the four trajectories. Also, Fig. 3.9 depicts the change of the length of tendons L_{1-4} for one repetition of $T_\circ$ task with slow speed.
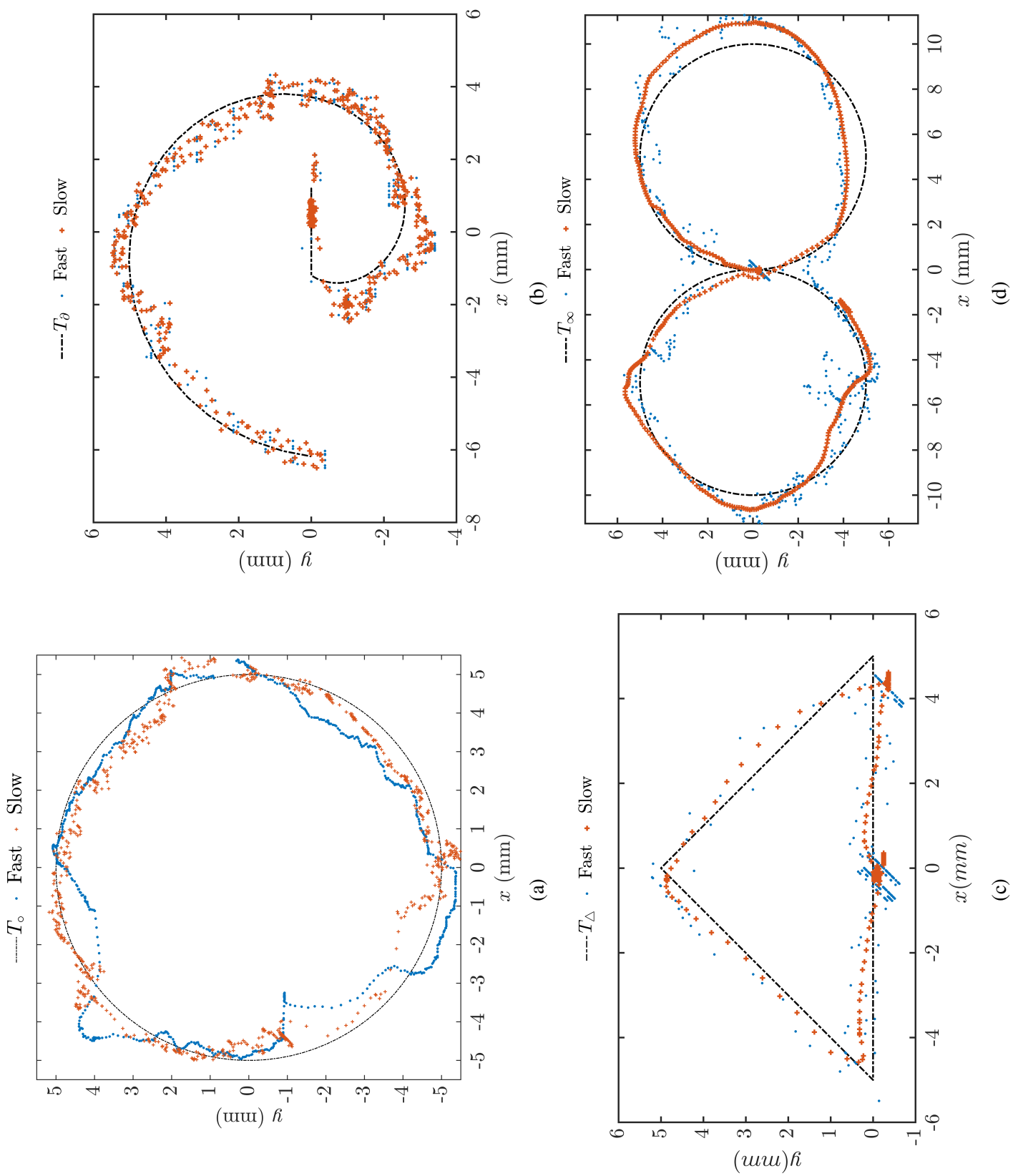
Figure 3.8: Desired and experimental trajectories for (a) circular, (b) spiral, (c) triangular, and (d) infinity-shape trajectories.

Table 3.2: Summary of the performance of the control system for the tip position of the catheter in four trajectories with slow and fast speeds.

Trajectory		RMS-error (mm)	Error range (mm)	Time-lag (s)
$T_\circ$	Slow	0.56 ± 0.41	(-0.84,1.07)	0.41
	Fast	0.73 ± 0.43	(-1.24,1.4)	0.38
$T_\triangle$	Slow	0.31 ± 0.24	(-0.35,0.47)	0.37
	Fast	0.40 ± 0.20	(-0.54,0.81)	0.43
T_∞	Slow	0.62 ± 0.54	(-1.05,1.14)	0.44
	Fast	0.84 ± 0.44	(-2.31,1.24)	0.41
T_∂	Slow	0.46 ± 0.39	(-0.89,1.26)	0.34
	Fast	0.52 ± 0.31	(-0.76,1.21)	0.40
Average	Slow	0.49 ± 0.48	$(-0.78, 0.99)$	0.39
	Fast	0.62 ± 0.35	$(-1.17, 1.16)$	0.41

The results showed that the system was fairly accurate in following the desired trajectories as the average RMS-error for the four trajectories was 0.49 ± 0.32 and 0.62 ± 0.36 mm for the slow and fast speeds, respectively. Also, the time-lag between the input and output was consistent among the trajectories with an average of 0.4s for all trajectories. A limiting factor in estimating the time-lags was the frame-rate of the cameras, i.e., 33 ± 5 Hz, as the image frame time-stamps were used as the synchronization benchmark. Therefore, the computed time-lag might have been smaller than the reported values. Another finding in this experiment was that the system was more accurate at slow speeds than fast speed trajectories.

However, for both the speeds the accuracy was within the acceptable practical precision of ± 1 mm, [19]. Moreover, small spikes in the temporal variation of the tip position of the catheter, e.g. Fig. 3.9 at $t = 4$s and $t = 8$s, were due to the change of tendon classes. At these time instances, the controller switched the classes thus, the tendon lengths before and after these instances was estimated by different neural networks. Nevertheless, the spikes are relatively small and decreased with the trajectory progressing farther from the tendon class boundaries. Author sought such switches between the tendon classes as a source of deviations from the planned trajectory observed in the experiments.

Experiment 2: target reaching

The second experiment was performed on a freshly excised bovine myocardial tissue. Four arbitrary target points denoted as P_{1-4} in Fig. 3.10(a), were selected and marked manually. Afterward, each point was selected on the top- and side-view live images in the user interface software and registered as a target. The test procedure was that after selecting each specific point the UI would determine if the point is within the catheter's reach and if so it would plan a direct path. Upon the user's approval, the system would initiate the task to hit the point, i.e., P_{1-4}, maintain the target position for three seconds, return to its resting position, i.e., $P_o = (0, 0, 40)^T$, and repeat the task for four repetitions.

This experiment was to replicate a robot-assisted ablation intervention with level-2 autonomy, where the surgeon would only specify the pre-planned location of the target point(s) on intraoperative images for ablation, based on which the robot would reach to the position, hold the position for the period on ablation (typically less than 30s) and move to a resting position.

Fig. 3.10(b) shows the variation of tip position of the catheter in Cartesian task space for a representative point P_3 and Table 3.3 summarizes the position of P_{1-4}, temporal average maintained positions in repetitions, RMS-error of in reaching tasks, and the repeatability of reached positions (standard deviation of the accumulative average reached positions for all repetitions).

The results of experiment II showed that the RCI system was successful in autonomous reaching to the pre-planned targets with a spatial error of 0.75 mm, i.e., the norm of the average RMS-error for P_{1-3}. Also, the system was capable of ignoring P_4 as being out of the feasible zone of the catheter. Moreover, the system showed fairly repeatable target hits with a spatial repeatability of ± 0.52 mm ,i.e., the norm of repeatability of x, y, and z.
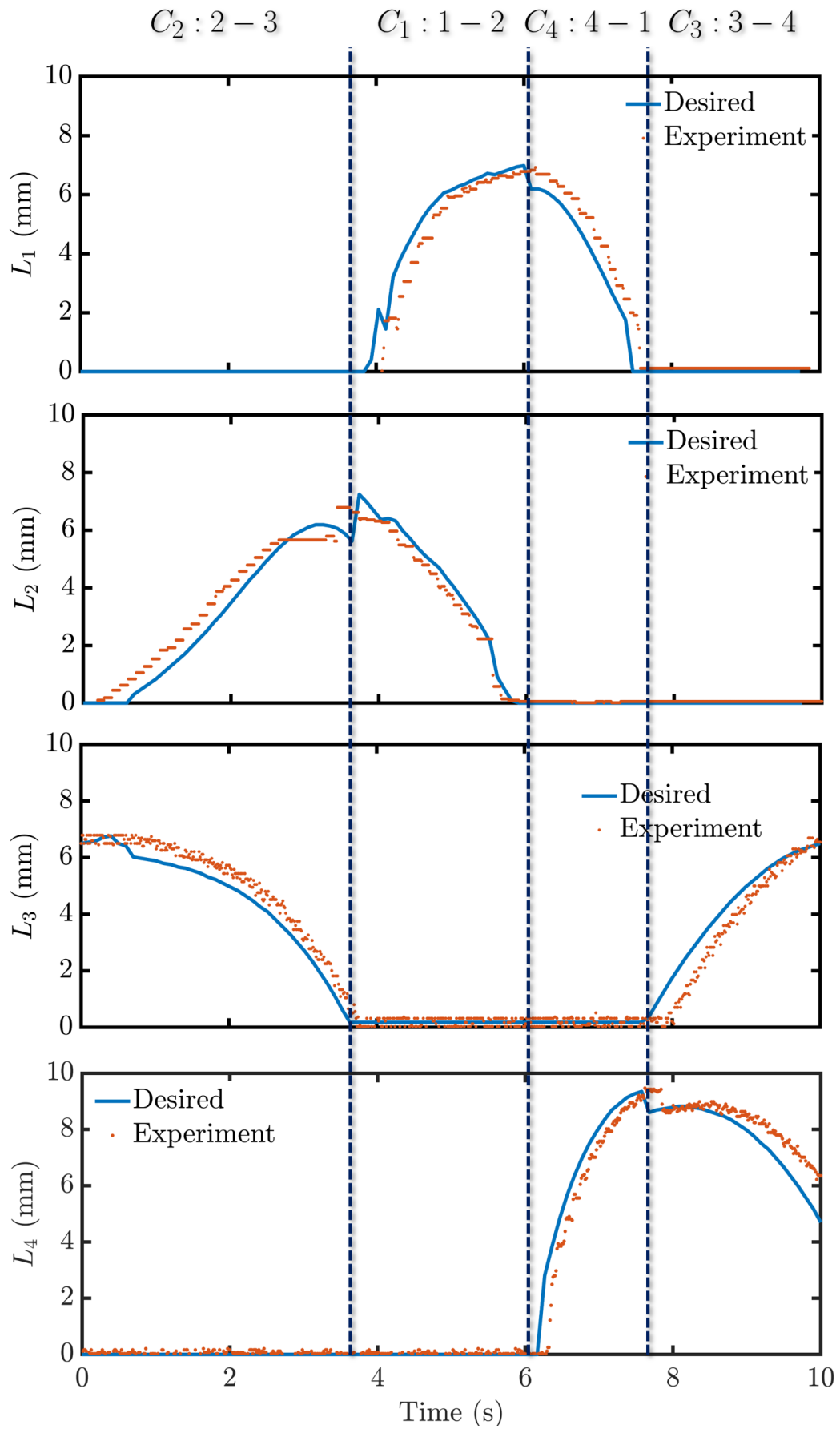
Figure 3.9: The desired and attained change in the length of the tendons for $T_\circ$ task. Tendon classes were automatically selected by the classifier so as to follow a full circle.
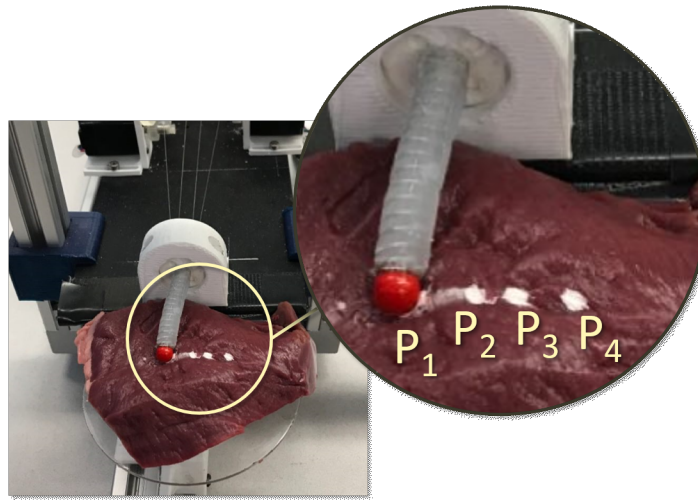
(a)
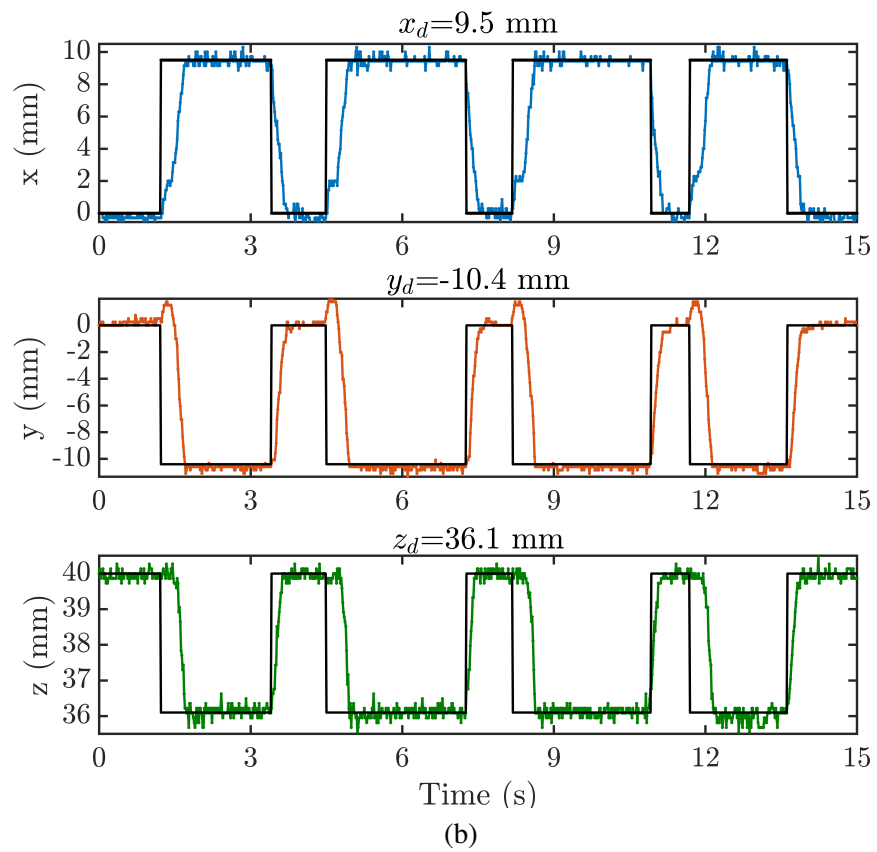
(b)

Figure 3.10: (a) marked positions on the bovine myocardial tissue for reaching tasks, P_{1-4}, and (b) Cartesian tip position of the catheter in four repetitions to reach P_3.

Table 3.3: Performance of the RCI in autonomous reaching to the targets P_{1-4} selected by the user in live images.

Target	Position (mm)	Reached Position (mm)	RMS-error (mm)	Repeatability (mm)
P_1	$(-6.9 \quad -9.7 \quad 37.4)^T$	$(-7.1 \quad -9.0 \quad 37.0)^T$	$(0.39 \quad 0.47 \quad 0.42)^T$	$\pm(0.3 \quad 0.3 \quad 0.3)$
P_2	$(5.2 \quad -8.4 \quad -35.7)^T$	$(5.9 \quad -8.1 \quad -34.9)^T$	$(0.37 \quad 0.52 \quad 0.44)^T$	$\pm(0.3 \quad 0.3 \quad 0.3)$
P_3	$(9.5 \quad -10.4 \quad -36.1)^T$	$(9.1 \quad -10.7 \quad -36.7)^T$	$(0.43 \quad 0.36 \quad 0.51)^T$	$\pm(0.3 \quad 0.3 \quad 0.3)$
$P_4^\star$	$(18.7 \quad -9.5 \quad -37.2)^T$	–	–	–
Average	–	–	$(0.4 \quad 0.45 \quad 0.46)^T$	$\pm(0.3 \quad 0.3 \quad 0.3)$

$\star$: User interface software overruled P_4 as it was out of the feasible space of the catheter.

3.5   Conclusions

The goal of this study was to propose and validate a control framework with level-2 autonomy (task autonomy) for kinematic control of flexible ablation catheters. Also, it was hypothesized that through learning-based classification and regression, the inverse kinematics of the soft catheter could be captured within the practical precision, i.e., ± 1 mm. Also, with a one-time preoperative calibration (training), the material and geometric nonlinearities involved in the deformation of the catheter, e.g., friction, large deformation, were captured and compensated. Thus, simplifying the catheter model.

All the modules of the RCI system in this study were developed in-house thus allowed for maximal software-hardware integration. Author believes that such integration was a key in the observed accuracy of the system. The validation study for the trajectory tracking and target reaching also showed fair accuracy and repeatability for position control of the catheter. More specifically, this study exhibited better spatial accuracy and repeatability compared to [136, 146, 199, 200, 187], where in all the cases the accuracy and repeatability were not sub-millimeter. Another promising finding was that the proposed control system did not exhibit a dead-zone at the proximity of the resting position. Such a dead-zone has been reported in other studies, e.g., [136] and have been sought related to the slack of the tendons. Moreover, the distributed implementation of the control system, i.e., the inverse kinematics in the user interface module and tendon length control in the firmware, allowed for multi-thread computation parallelization of the control system. Such a multi-thread parallelization was crucial in reaching the small time-lag.

For further improvement of this study, researchers are encouraged to replace the stepper motors with servo-motors which would facilitate dynamic torque control on the catheter. Also, releasing the two-tendon drive condition and allowing for more tendons to be pulled simultaneously would increase the feasible space of the catheter. Nevertheless, the latter may incur considerable compression in the catheter's spine and violate the constant bending radius assumption. Furthermore, increasing the number of tendons would have a double effect worth the investigation. On one side more tendons would potentially lead to finer control of the pose of the catheter. Nevertheless, more tendons would worsen the redundancy of the catheter. Consequently, it would increase the tendon driving classes

and the occurrence of the switching between the classes factorially. The latter was sought as a source of deviation from the planned trajectories in this study.

Another extension of this work would be adding a linear degree of freedom to the base of the catheter, e.g., as proposed in [136]), or adding a second set of tendons terminated midspan of the catheter length. Such extensions would expand the feasible space of the catheter spatially, however would increase the degrees of freedom and might change the kinematics of the catheter.

Chapter 4

Sensor-free Force Control of Tendon-driven Ablation Catheters through Position Control and Contact Modeling

4.1 Abstract

In the present study a sensorless force control framework for tendon-driven steerable catheters was proposed and validated. The hypothesis of this study was that the contact force between the catheter tip and the tissue could be controlled using the estimated force with a previously validated displacement-based viscoelastic tissue model. The tissue model was used in a feedback control loop. The model estimated the contact force based on a realtime estimation of catheter-tissue indentation depth performed by a data-driven inverse kinematic model. To test the hypothesis, a tendon-driven catheter ($\phi 6 \times 40$mm) and a robotic catheter intervention system were prototyped and characterized. Three validation studies were performed to test the performance of the proposed system with static and dynamic inputs. The results showed that the system was capable of reaching to the desired force with a root-mean-square error of 0.03 ± 0.02N for static tests and 0.05 ± 0.04N for dynamic inputs.

The main contribution of this study was providing a computationally cheap and sensor-free force control schema for the tendon-driven catheters with ablation applications.

4.2 Introduction

4.2.1 Background

Cardiac arrhythmia is known as the prime cause of heart disorders and hospitalization [201]. Catheter ablation procedure has been widely adopted as an effective interventional treatment for cardiac arrhythmia [202]. Thanks to its minimally invasive approach and long-term effectiveness, ablation therapies are adopted at an increasing pace globally [202]. Fig. 4.1 shows a schematic view of the ablation catheter inside the right ventricle. During this procedure, arrhythmatic cardiac cells are inactivated through freezing (cryo-ablation) or burning (radio-frequency ablation). Studies have shown that maintaining contact force between 0.1–0.3 N, is necessary for effective ablation and to avoid tissue perforation [31, 19]. However, with the state-of-the-art robotic catheter intervention (RCI) systems, surgeons lose the direct touch on the catheter and are less situation-aware of the catheter-tissue interaction forces [172].

With the emergence of semi-autonomous RCI, the role of force-estimation methods has become more prominent, as the the need for force control of the catheter has increased. To this end, researchers have proposed various force estimation methods based on beam theory [173], differential geometry [174], and multi-body dynamics [203] approaches. Also, heuristic models such as neural networks [193] and Gaussian mixture models [136] have been investigated for force estimation on flexible catheters. While mechanistic models offer high accuracy and mechanical plausible results, they are often computationally expensive and sensitive to nonlinearities such as dead-zone and material hyperelasticity. On the other hand, heuristic models are often computationally fast and easy to implement. Nevertheless, training of the models and physical interpretation of the model parameters is demanding [19].

Moreover, utilization of sensors on the catheter is not favorable as it complicates the manufacturing process, limits the range of motion of the catheters, and increases the cost of disposal catheters
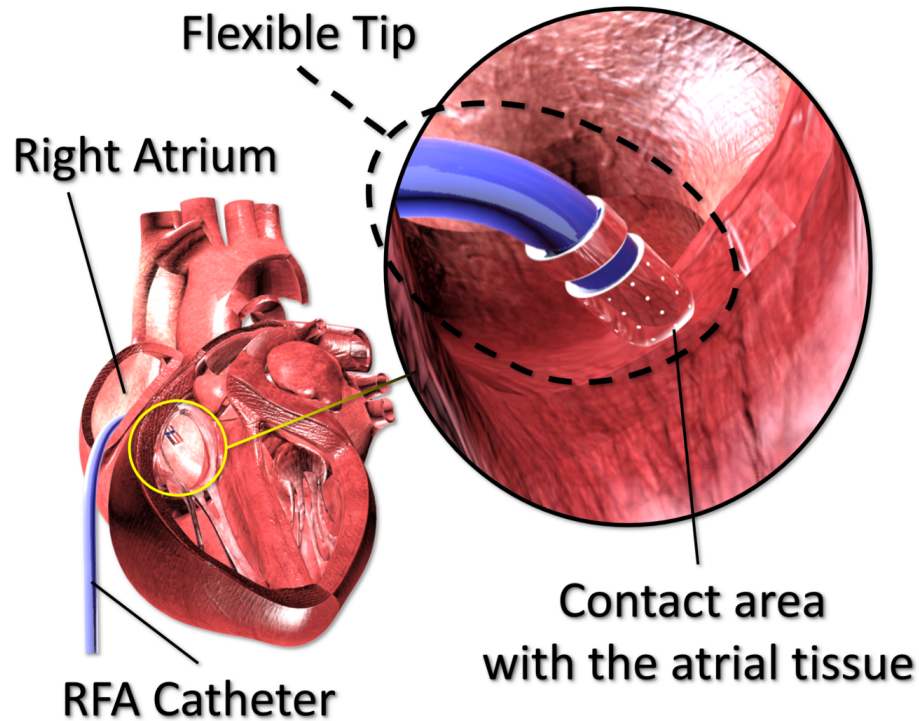
Figure 4.1: The schematic shape of steerable ablation catheters in the right atrium during ablation interventions.

[172]. As an alternative, sensor-free, a.k.a. sensorless, force estimation methods have been developed. Such methods, e.g., [189], rely on shape sensing of the catheter and relating the tip forces on it. The shape sensing necessitates utilization of image processing or embedding sensors in the catheter body [19]. Studies have shown that shape-based methods may be highly sensitive to the shape estimation errors [172].

4.2.2 Contributions

Alternatively in this study, a sensor-free force control schema was proposed and validated. The proposed method builds upon our previous studies on estimating the contact force with a displacement-based viscoelastic model in [17] and kinematic control of the flexible catheter with a learning-based inverse kinematic method in [204]. The main contribution of this study was proposing a computationally, sensor-free, and displacement-based force control schema with accounting
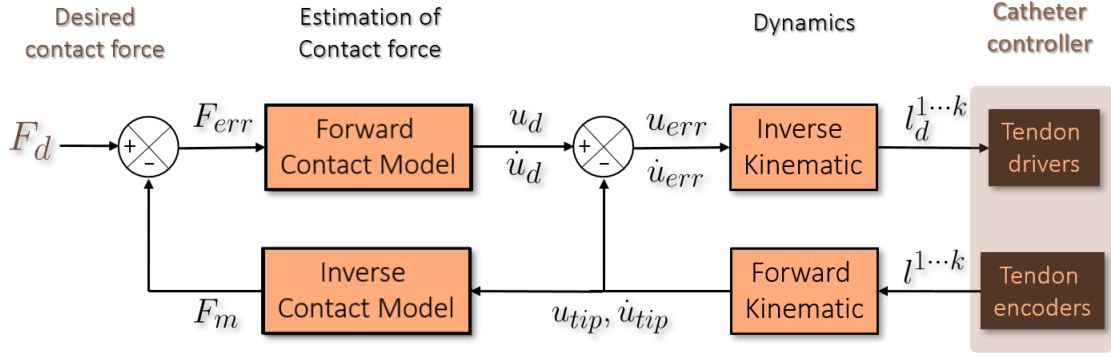
Figure 4.2: Proposed contact force control schema.

for the mechanical properties of the tissue. A realtime accurate viscoelastic contact model estimation schema was proposed and validated in [165, 17].

4.3 Material and Methods

4.3.1 Contact Model

The proposed force control schema is depicted in Fig. 4.2. The catheter was assumed to be in an initial contact with the tissue and the force control schema was based on finding the desired indentation depth, u_d, to generate a desired force, F_d, from the catheter-tissue contact model. The contact model was adopted from [17] and was a generalized Kelvin-Voigt (GKV) viscoelastic model with three GKV units and with the nonlinearity power of $p = 5$. The displacement-based contact model is presented in Eq. 24.

$$\mathbf{K}x(t) + \mathbf{C}\dot{x}(t) = -f(t), \tag{24}$$

where, $\mathbf{K}$ and $\mathbf{C}$ are the stiffness and viscous friction material matrices, $f(t)$ was the contact force, and $x(t) = \left(u(t) \quad x_1(t) \quad x_2(t) \quad x_3(t) \right)^T$, was the state displacements. Contact for necessitated model parameter identification to obtain the tissue-specific material matrices.

To this end and to simulate the myocardial tissue, a 14mm-thick sheet of viscoelastic silicon-rubber material with shore hardness of 20-OO (Ecoflex$^{\text{TM}}$ 00-20, Smooth-on Inc., PA, USA) was fabricated. Same material has been used in similar studies as myocardial tissue phantom, e.g., [165]. Adopting the optimization schema proposed in [17], the mechanical properties of the phantom tissue, i.e.,

contact model parameters, were identified with a goodness-of-fit of $R^2 = 0.94\%$ and root-mean-square (RMS) error of 0.03 ± 0.02 (Eq. 25–26).

$$K = \begin{pmatrix} 0.25 & 0 & 0 & 0 \\ -0.47 & 0.47 & 0 & 0 \\ 0 & -0.52 & 0.52 & 0 \\ 0 & 0 & -0.74 & 0.73 \end{pmatrix} \frac{N}{mm} \tag{25}$$

$$C = \begin{pmatrix} 0 & 0 & 0 & 0 \\ -16.46 & 16.46 & 0 & 0 \\ 0 & -8.72 & 8.72 & 0 \\ 0 & 0 & -1.98 & 1.98 \end{pmatrix} \frac{Ns}{mm} \tag{26}$$

4.3.2 Catheter Tip Position Control

For the experimental tests, a spring loaded catheter with silicon rubber body was fabricated with 40 mm length and 6 mm diameter. These dimensions were selected so as to cover the required workspace inside the right atrium [196]. Fig. 4.3(a) shows the assembly of the fabricated catheter. Precise controlling the catheter tip to reach a desired indentation state, $(u_d, \dot{u}_d)^T$, was essential for the force control. Therefore, a neural network learning-based schema based on the findings of [204] was adopted to determine the desired length of each tendon, $(l_d^{1-4}, \dot{l}_d^{1-4})^T$, for a given desired indentation depth, $(u_d, \dot{u}_d)^T$. The desired indentation depth, i.e., as tip position $\left(0, -u_d(t), 0)^T\right)$ was the input to the neural network and the tendons length were the output. The fitting was performed between the input and output using a fully connected architecture with ten hidden layers and five nodes per layer. The training dataset was based on the Cartesian feasible space obtained in [204]. The cross-validation showed a goodness-of-fit of $R^2 = 0.98$ for the neural network fitting.
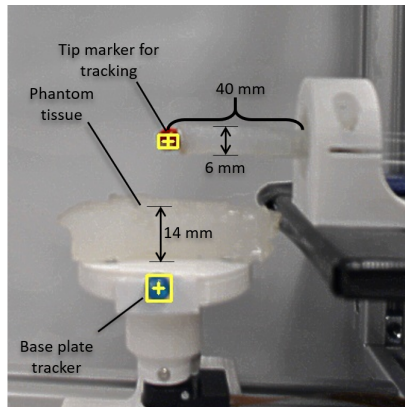
(a)

(b)

1. Base plate
2. Microprocessor and motor drivers (x2 Arduino Uno)
3. Potentiometers (x4)

4. USB Cameras (x2 C920 Logitec)
5. Stepper motors (x4 200 PPR)
6. USB cables to PC
7. Aluminum frame
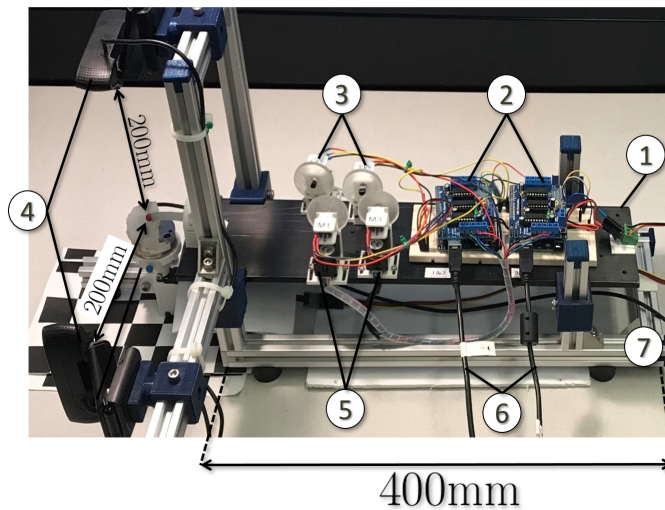
+4.2v

Power supply
AB-330CUL

400mm

(c)

Figure 4.3: (a) assembly of the fabricated spring-loaded catheter and the driving tendons, (b) the fabricated catheter under cantilever bending test, (c) the system architecture used for the validation studies, (d) the RCI system used for the validation studies.

4.3.3   Force Estimation and Control

For a given desired force, F_d, Eq. 24 was solved incrementally for a time step of δt. The incremental expression of Eq. 24 was

$$x(t + \delta t) = x(t) - \delta t \mathbf{C}^{-1} \left((0 \quad F_d \quad 0)^T + \mathbf{K}x(t) \right). \tag{27}$$

The time step was determined in realtime as the absolute time difference between two indentation evaluations. Time step was constant 0.01s as the indentation refresh frequency was set to 100Hz in the control loop. Feeding the updated $u_d(t + \delta t)$ to the tendon length control loop, the RCI system would follow the incremental changes in the tendon lengths. Also, as for calculating the force feedback for compensation, Eq. 27 would be directly evaluated with the current lengths of the tendons $l_k^{k=1-4}$ and estimated force F_m would be compared with the desired force for compensation. Furthermore, the apparent compressive stiffness of the phantom tissue was estimated as $k_t = 0.10$ Nmm^{-1} using Eq. 28, while a cantilever bending test depicted in Fig. 4.3(b) showed that the bending stiffness of the catheter at its tip was $k_b = 1.1$Nmm^{-1}. The comparison validated the negligible contact-induced bending deflection of the catheter.

$$k_t = \left(\sum_{i=0}^{3} \frac{1}{K_{ii}} \right)^{-1} \tag{28}$$

4.4   Experimental Validation

4.4.1   Experimental setup

Fig. 4.3(c) shows the RCI system developed for the experimental validations. The control system was implemented in parallel in two Arduino Uno microprocessors hooked to four rotational encoders for the tendons length feedbacks and stepper motor driving. Also, the neural network and image acquisition systems (used for documentation) were implemented in the user interface in .Net C# environment. Also, a six-DoF ATI Mini40 force sensor was used as the benchmark for the comparison. Moreover, a linear motor was used to change the height of the phantom tissue to simulate the motion of the heart. Two markers, red and blue, were used to measure the relative
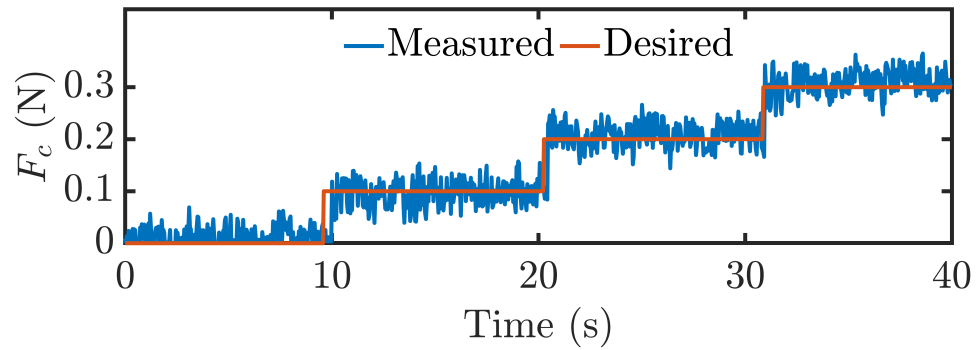
Figure 4.4: The desired force and the desired force for Experiment I.

distance of the catheter tip (as a measure of indentation) in realtime.

4.4.2 Experiment I: constant force

To test the system, three validation studies were performed. In the first study, the desired force value was changed from 0N to 0.1, 0.2, and 0.3N at 10s intervals. The system would change the indentation depth autonomously to achieve the desired force. Fig. 4.4 shows the desired and achieved contact forces for Experiement I. The system exhibited fair following of the desired input with an RMS-error of 0.03 ± 0.02 N. Also, the maximum absolute error was 0.07 N. Moreover, the output shows a lag of 0.24s at the stepping times, i.e., 10s, 21s, and 32s.

4.4.3 Experiment II: sinusoidal force

In the second experiment, the desired force was sinusoidal with 0.5, 1, and 1.5Hz frequency, 0.2N mean, and 0.1N amplitude. These frequencies were selected to cover the lower bound and upper bound of the arrhythmatic heart beating frequencies, i.e., 30 and 90 beat-per-minute, respectively. Fig. 4.5 depicts the desired and achieved forces. The RMS-error for 0.5, 1, and 1.5Hz inputs were 0.04 ± 0.02, 0.03 ± 0.02, and 0.05 ± 0.03 N, respectively, while the maximum errors were 0.06, 0.07, and 0.15 N, respectively. The average lag time estimated at the peaks of the curves were 0.13, 0.27, and 0.31 s, respectively.
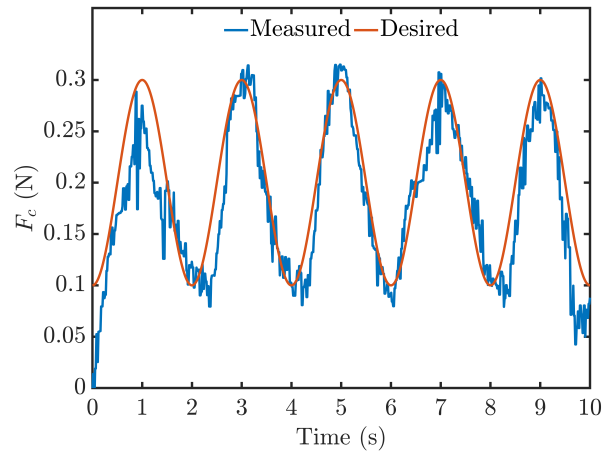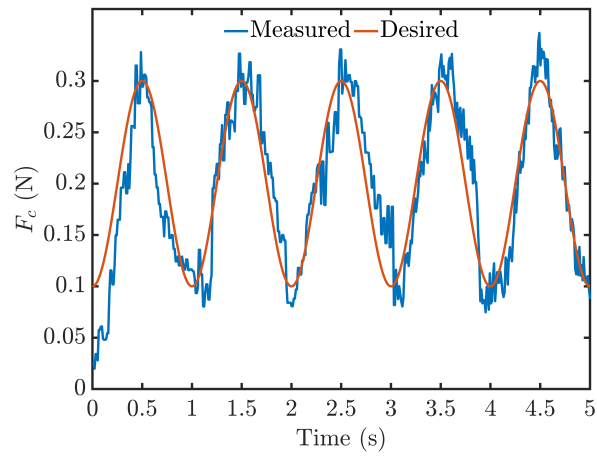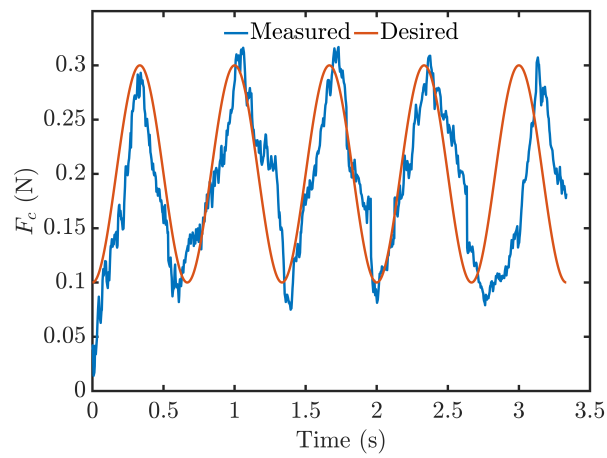
Figure 4.5: Desired versus the achieved contact force for (a) 0.5Hz, (b) 1Hz, and (c) 1.5Hz sinusoidal input.

4.4.4 Experiment III: constant force on a moving tissue

In the third study, the linear stage was moved sinusoidally with 1 and 1.5Hz frequency and 10mm amplitude. This study was to simulate the heart motion. As in practice, ultrasound imaging is available and the heart motion is monitored, video imaging was used as a replication of the ultrasound. The objective of the third study was to achieve and maintain a constant desired force of 0.2N. Fig. 4.6 shows the achieved contact force and indentation depth (obtained from the video cameras). The system achieved the average force of 0.19N and maintained it with ± 0.04 N variation for 1Hz and achieved 0.23 N and maintained ± 0.04 N for 1.5Hz test.

4.5 Conclusions

The aim of this study was to propose and validate a sensor-free force control schema for tendon-driven ablation catheters. The validation results showed that the system was capable of controlling the contact force with an average rms-error of 0.04 ± 0.05N for constant and sinusoidal desired forces and with 0.02 ± 0.04 N RMS-error on the moving sample. Since the required control range of the force is 0.2 ± 0.1N, authors sought the performance acceptable for the intended application.
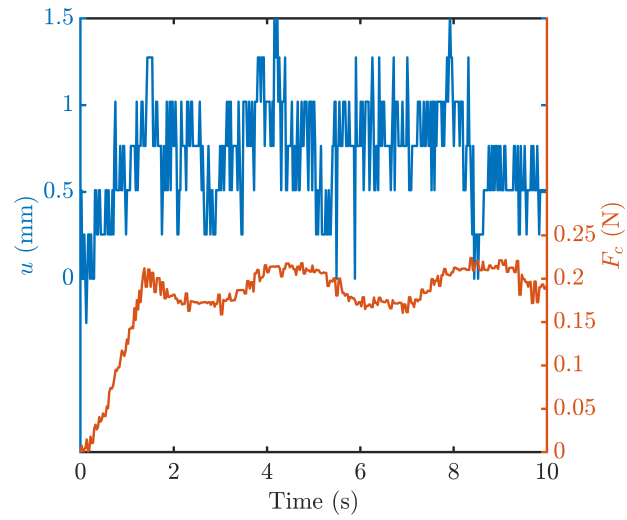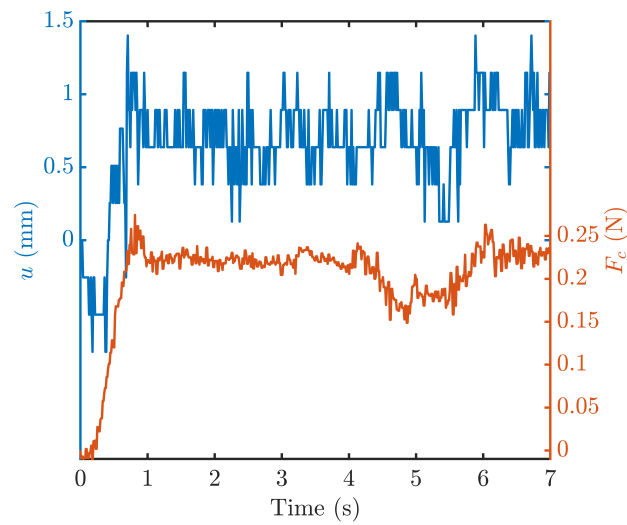
Figure 4.6: Results of force control while the contacting phantom tissue moves sinusoidally with (a) 1Hz, and (b) 1.5Hz frequency. The desired force for both the cases was 0.2 N.

Chapter 5

Conclusion and Future Works

5.1 Conclusions

In this thesis, a $n-$ generalized Kelvin-Voigt viscoelastic model was developed and introduced in chapter 2, to estimate the viscoelastic behaviour of the heart wall tissue. The referred mechanical model could be optimized and characterized for any desired viscoelastic-like tissue to adopt the behaviour and estimate either the displacement induced by a known force or the amount of force in the result of a known displacement input. The forward and inverse solutions were presented and the results were validated by comparing the results in an *ex-vivo* test. The optimization method was postulated a particle swarm optimization (PSO) technique which is a global optimization method. The results indicated that the proposed contact model was computationally cheap and favorable for realtime applications.

Next, a steerable flexible tendon-driven catheter and a robotic catheter intervention system were designed and developed. The learning-based inverse kinematic schema was shown to be a favorable option for achieving a level-2 autonomy (task autonomy) for RFA catheters. The system showed sub-millimeter position resolution and accuracy. Also, the proposed learning-based classification and regression, successfully resolved the redundancy of the proposed robotic system.

From a practical point of view, with a one-time preoperative calibration (training), the material and geometric nonlinearities involved in the deformation of the catheter, e.g., friction, large deformation, could be captured pre-operatively.

All the modules of the RCI system in this study were developed in-house thus allowed for maximal software-hardware integration. The author believes that such integration was key in the observed accuracy of the system. The validation studies for the position control and force control demonstrated fair accuracy and repeatability of the proposed RCI system. More specifically, this study exhibited better spatial accuracy and repeatability compared to the similar reported studies, wherein all the cases the accuracy and repeatability were not sub-millimeter. Also, the system was capable of attaining and maintaining the desired force profiles in both static and dynamic conditions. Another promising finding was that the proposed control system did not exhibit a dead-zone at the proximity of the resting position, which is unprecedented. Moreover, the distributed implementation of the control system, i.e., the inverse kinematics in the user interface module and tendon length control in the firmware, allowed for multi-thread computation parallelization of the control system. Such a multi-thread parallelization was crucial in reaching the small time-lag.

In summary, with this research a generalized force control schema for the RFA catheters was proposed and validated. The proposed system is accurate within required the practical force range, i.e. 0.2 ± 0.1 N and spatial position resolution, i.e., 1mm. It is also easy to implement and does not require employment of sophisticated mechanical models and/or force sensors. Most importantly, the author sought this study as a demonstration of the level-2 autonomy for the next generation RCI systems.

5.2 Future Studies

To the best of author's knowledge, this work was the first to propose a force control schema for the tendon-driven RFA catheters. Therefore the author acknowledges its limitations in assumptions and implementations. A summary of the propositions for the future work to address the limitations are as follows:

(i) the dynamic model validated in chapter 2, was developed based on experimental measurement of the force-displacement response of the myocardial tissue. Although Hooshiar *et al.* [165] have proposed a low profile sensor for obtaining the required force information in realtime, in

practice, such a force sensor might increase the complexity of the catheter and include measurement uncertainties. Therefore, an extension of this work could be to include an online parameter estimation module to the system to correct the estimated model parameters intraoperatively using an adaptive schema, e.g., such as proposed in [126].

(ii) another improvement would be to investigate the feasibility of impedance-matching optimization procedure, as an alternative to the force-displacement matching, for parameter identification. Such an impedance model would decrease the number of contact model parameter to three, i.e., inductive, resistive, and capacitive impedances, thus further simplify the contact model.

(iii) another improvement of this study would be to replace the stepper motors with servo-motors which would facilitate dynamic torque control on the catheter. Also, releasing the two-tendon drive condition and allowing for more tendons to be pulled simultaneously would increase the feasible space of the catheter. Nevertheless, the latter may incur considerable compression in the catheter's spine and violate the constant bending radius assumption. Furthermore, increasing the number of tendons would have a double effect worth the investigation. On one side more tendons would potentially lead to finer control of the pose of the catheter. Nevertheless, more tendons would worsen the redundancy of the catheter. Consequently, it would increase the tendon driving classes and the occurrence of the switching between the classes factorially. The latter was sought as a source of deviation from the planned trajectories in this study.

(iv) Another extension of this work would be adding a linear degree of freedom to the base of the catheter, or adding a second set of tendons terminated midspan of the catheter length. Such extensions would expand the feasible space of the catheter spatially, however, would increase the degrees of freedom and might change the kinematics of the catheter.

Bibliography

[1] W. H. O. (WHO). Cardiovascular diseases (cvds) factsheets. http://www.who.int/mediacentre/factsheets/fs317/en, September 2016.

[2] Ed. K. Chatterjee. *Cardiology:An Illustrated Text/Reference , vol. 1. Baltimore, MD*. Lippincott, 1991.

[3] Philip J Podrid and Robert J Myerburg. Epidemiology and stratification of risk for sudden cardiac death. *Clinical Cardiology: An International Indexed and Peer-Reviewed Journal for Advances in the Treatment of Cardiovascular Disease*, 28(S1):3–11, 2005.

[4] Charles Florin, Nikos Paragios, and Jim Williams. Particle filters, a quasi-monte carlo solution for segmentation of coronaries. In *International Conference on Medical Image Computing and Computer-Assisted Intervention*, pages 246–253. Springer, 2005.

[5] Alan S Go, Elaine M Hylek, Kathleen A Phillips, YuChiao Chang, Lori E Henault, Joe V Selby, and Daniel E Singer. Prevalence of diagnosed atrial fibrillation in adults: national implications for rhythm management and stroke prevention: the anticoagulation and risk factors in atrial fibrillation (atria) study. *Jama*, 285(18):2370–2375, 2001.

[6] Emelia J Benjamin, Philip A Wolf, Ralph B DAgostino, Halit Silbershatz, William B Kannel, and Daniel Levy. Impact of atrial fibrillation on the risk of death: the framingham heart study. *Circulation*, 98(10):946–952, 1998.

[7] Simon Stewart, Carole L Hart, David J Hole, and John JV McMurray. A population-based study of the long-term risks associated with atrial fibrillation: 20-year follow-up of the renfrew/paisley study. *The American journal of medicine*, 113(5):359–364, 2002.

[8] leehealth. Cardiology: About your heart,how does the heart beat? the heartbeat, 2019. http://www.leehealth.org/cardiaccare/about/heartbeat.asp,.

[9] Susan Colilla, Ann Crow, William Petkun, Daniel E Singer, Teresa Simon, and Xianchen Liu. Estimates of current and future incidence and prevalence of atrial fibrillation in the us adult population. *The American journal of cardiology*, 112(8):1142–1147, 2013.

[10] Rashid Ghorbani Afkhami, Ghanbar Azarnia, and Mohammad Ali Tinati. Cardiac arrhythmia classification using statistical and mixture modeling features of ecg signals. *Pattern Recognition Letters*, 70:45–51, 2016.

[11] Xiu-Shan Wu, Wanwan Cai, Ping Zhu, and Wuzhou Yuan. New strategies for arrhythmia treatment. *Journal of Cardiology and Therapy*, 5(1):756–763, 2018.

[12] Ahmed AlTurki, Riccardo Proietti, Vincenzo Russo, Tarvinder Dhanjal, Prithwish Banerjee, and Vidal Essebag. Anti-arrhythmic drug therapy in implantable cardioverter-defibrillator recipients. *Pharmacological research*, 2019.

[13] Ian D McRury and David E Haines. Ablation for the treatment of arrhythmias. *Proceedings of the IEEE*, 84(3):404–416, 1996.

[14] ROY Beinart, Suhny Abbara, Andrew Blum, Maros Ferencik, Kevin Heist, Jeremy Ruskin, and Moussa Mansour. Left atrial wall thickness variability measured by ct scans in patients undergoing pulmonary vein isolation. *Journal of cardiovascular electrophysiology*, 22(11):1232–1236, 2011.

[15] Burr Hall, Vinodh Jeevanantham, Rochelle Simon, John Filippone, Gabriel Vorobiof, and James Daubert. Variation in left atrial transmural wall thickness at sites commonly targeted for ablation of atrial fibrillation. *Journal of Interventional Cardiac Electrophysiology*, 17(2):127–132, 2006.

[16] Abhishek Bhaskaran, William Chik, Jim Pouliopoulos, Chrishan Nalliah, Pierre Qian, Tony Barry, Fazlur Nadri, Rahul Samanta, Ying Tran, Stuart Thomas, et al. Five seconds of 50–60

w radio frequency atrial ablations were transmural and safe: an in vitro mechanistic assessment and force-controlled in vivo validation. *Europace*, 19(5):874–880, 2016.

[17] Mohammad Jolaei, Amir Hooshiar, and Javad Dargahi. Displacement-based model for estimation of contact force between rfa catheter and atrial tissue with ex-vivo validation. In *2019 IEEE International Symposium on Robotic and Sensors Environments (ROSE)*, pages 1–7. IEEE, 2019.

[18] Sabine Ernst, Feifan Ouyang, Christian Linder, Klaus Hertting, Fabian Stahl, Julian Chun, Hitoshi Hachiya, Dietmar Bansch, Matthias Antz, and Karl-Heinz Kuck. Initial experience with remote catheter ablation using a novel magnetic navigation system: magnetic remote catheter ablation. *Circulation*, 109(12):1472–1475, 2004.

[19] Amir Hooshiar, Siamak Najarian, and Javad Dargahi. Haptic telerobotic cardiovascular intervention: a review of approaches, methods, and future perspectives. *IEEE Reviews in Biomedical Engineering*, 2019.

[20] Rochester University Medical center. Robotic-assisted cardiac surgery. http://www.urmc.rochester.edu/encyclopedia/, September 2016.

[21] Giora Weisz, D Christopher Metzger, Ronald P Caputo, Juan A Delgado, J Jeffrey Marshall, George W Vetrovec, Mark Reisman, Ron Waksman, Juan F Granada, Victor Novack, et al. Safety and feasibility of robotic percutaneous coronary intervention: Precise (percutaneous robotically-enhanced coronary intervention) study. *Journal of the American College of Cardiology*, 61(15):1596–1600, 2013.

[22] Nathaniel R Smilowitz, Jeffrey W Moses, Fernando A Sosa, Benjamin Lerman, Yasir Qureshi, Kate E Dalton, Lauren T Privitera, Diane Canone-Weber, Varinder Singh, Martin B Leon, et al. Robotic-enhanced pci compared to the traditional manual approach. *J Invasive Cardiol*, 26(7):318–21, 2014.

[23] Arnold H Seto and Morton J Kern. Robotic-assist pci: Precision guided pci or a rube goldberg solution? *Catheterization and Cardiovascular Interventions*, 83(6):922–923, 2014.

[24] Hedyeh Rafii-Tari, Christopher J Payne, Colin Bicknell, Ka-Wai Kwok, Nicholas JW Cheshire, Celia Riga, and Guang-Zhong Yang. Objective assessment of endovascular navigation skills with force sensing. *Annals of biomedical engineering*, 45(5):1315–1327, 2017.

[25] Simon K Neequaye, Rajesh Aggarwal, Isabelle Van Herzeele, Ara Darzi, and Nicholas J Cheshire. Endovascular skills training and assessment. *Journal of vascular surgery*, 46(5):1055–1064, 2007.

[26] Timothy R Coles, Dwight Meglan, and Nigel W John. The role of haptics in medical training simulators: A survey of the state of the art. *IEEE Transactions on haptics*, 4(1):51–66, 2010.

[27] Baofeng Gao, Shuxiang Guo, Nan Xiao, and Jin Guo. Design of the virtual reality based robotic catheter system for minimally invasive surgery training. In *2012 IEEE International Conference on Automation and Logistics*, pages 611–616. IEEE, 2012.

[28] Klaus A Hausegger, Peter Schedlbauer, Hannes A Deutschmann, and Kurt Tiesenhausen. Complications in endoluminal repair of abdominal aortic aneurysms. *European journal of radiology*, 39(1):22–33, 2001.

[29] Tsuyoshi Kaneko and Walter Randolph Chitwood Jr. Current readings: status of robotic cardiac surgery. In *Seminars in thoracic and cardiovascular surgery*, volume 25, pages 165–170. Elsevier, 2013.

[30] Ryan Madder, Paul Campbell, Ehtisham Mahmud, David Wohns, Tomasz Stys, Ronald Caputo, Mark Leimbach, Manish Parikh, Vijaykumar Kasi, and Giora Weisz. Multi-center post-market registry for the evaluation of robotic assisted pci. *Journal of the American College of Cardiology*, 67(13 Supplement):224, 2016.

[31] Dipen C Shah, Hendrik Lambert, Hiroshi Nakagawa, Arne Langenkamp, Nicolas Aeby, and Giovanni Leo. Area under the real-time contact force curve (force–time integral) predicts radiofrequency lesion size in an in vitro contractile model. *Journal of cardiovascular electrophysiology*, 21(9):1038–1043, 2010.

[32] Yasuo Okumura, Susan B Johnson, T Jared Bunch, Benhur D Henz, CHRISTINE J O'BRIEN, and Douglas L Packer. A systematical analysis of in vivo contact forces on virtual catheter tip/tissue surface contact during cardiac mapping and intervention. *Journal of cardiovascular electrophysiology*, 19(6):632–640, 2008.

[33] Luigi Di Biase, Andrea Natale, Conor Barrett, Carmela Tan, Claude S Elayi, Chi Keong Ching, Paul Wang, AMIN AL-AHMAD, Mauricio Arruda, J David Burkhardt, et al. Relationship between catheter forces, lesion characteristics,popping, and char formation: experience with robotic navigation system. *Journal of cardiovascular electrophysiology*, 20(4):436–440, 2009.

[34] Hardik J Pandya, Jun Sheng, and Jaydev P Desai. Mems-based flexible force sensor for tri-axial catheter contact force measurement. *Journal of Microelectromechanical Systems*, 26(1):264–272, 2016.

[35] John A Hauck. Cardiac tissue elasticity sensing, March 6 2012. US Patent 8,131,379.

[36] Hendrik Lambert, Stuart J Olstad, and Olivier B Fremont. Prediction of atrial wall electrical reconnection based on contact force measured during rf ablation, October 6 2015. US Patent 9,149,327.

[37] R Surapaneni, Q Guo, Y Xie, DJ Young, and CH Mastrangelo. A three-axis high-resolution capacitive tactile imager system based on floating comb electrodes. *Journal of Micromechanics and Microengineering*, 23(7):075004, 2013.

[38] N. Bandari, J. Dargahi, and M. Packirisamy. Tactile sensors for minimally invasive surgery: a review of the state-of-the-art, applications, and perspectives. *IEEE Access*, pages 1–1, 2019.

[39] Pietro Valdastri, Keith Houston, Arianna Menciassi, Paolo Dario, Arne Sieber, Masaru Yanagihara, and Masakatsu Fujie. Miniaturized cutting tool with triaxial force sensing capabilities for minimally invasive surgery. *Journal of Medical Devices*, 1(3):206–211, 2007.

[40] Yong-Jae Kim, Shanbao Cheng, Sangbae Kim, and Karl Iagnemma. A novel layer jamming mechanism with tunable stiffness capability for minimally invasive surgery. *IEEE Transactions on Robotics*, 29(4):1031–1042, 2013.

[41] Hunter B Gilbert, Joseph Neimat, and Robert J Webster. Concentric tube robots as steerable needles: Achieving follow-the-leader deployment. *IEEE Transactions on Robotics*, 31(2):246–258, 2015.

[42] Radosław Cieślak and Adam Morecki. Elephant trunk type elastic manipulator-a tool for bulk and liquid materials transportation. *Robotica*, 17(1):11–16, 1999.

[43] Ian D Walker, Darren M Dawson, Tamar Flash, Frank W Grasso, Roger T Hanlon, Binyamin Hochner, William M Kier, Christopher C Pagano, Christopher D Rahn, and Qiming M Zhang. Continuum robot arms inspired by cephalopods. In *Unmanned Ground Vehicle Technology VII*, volume 5804, pages 303–314. International Society for Optics and Photonics, 2005.

[44] William M Kier. The functional morphology of the musculature of squid (loliginidae) arms and tentacles. *Journal of Morphology*, 172(2):179–192, 1982.

[45] Christos Bergeles, Andrew H Gosline, Nikolay V Vasilyev, Patrick J Codd, J Pedro, and Pierre E Dupont. Concentric tube robot design and optimization based on task and anatomical constraints. *IEEE Transactions on Robotics*, 31(1):67–84, 2015.

[46] Yong-Jae Kim, Shanbao Cheng, Sangbae Kim, and Karl Iagnemma. A stiffness-adjustable hyperredundant manipulator using a variable neutral-line mechanism for minimally invasive surgery. *IEEE transactions on robotics*, 30(2):382–395, 2013.

[47] Jonathan Marvin Tobis and Islam Abudayyeh. New devices and technology in interventional cardiology. *Journal of cardiology*, 65(1):5–16, 2015.

[48] Tina Shoa, John D Madden, Nigel R Munce, and Victor XD Yang. Steerable catheters. *Biomedical Applications of Electroactive Polymer Actuators*, pages 229–246, 2009.

[49] Ottawa Cardiovascular Center. Cardiac Catheterization (referral), year = 2019, url = http://www.ottawacvcentre.com/services-cardiac-catheterization.html, urldate = 2010-09-30.

[50] Mathew D Hutchinson, Fermin C Garcia, Jeff E Mandel, Nabil Elkassabany, Erica S Zado, Michael P Riley, Joshua M Cooper, Rupa Bala, David S Frankel, David Lin, et al. Efforts to enhance catheter stability improve atrial fibrillation ablation outcome. *Heart Rhythm*, 10(3):347–353, 2013.

[51] Takehiro Kimura, Seiji Takatsuki, Ako Oishi, Masachika Negishi, Shin Kashimura, Yoshinori Katsumata, Takahiko Nishiyama, Nobuhiro Nishiyama, Yoko Tanimoto, Yoshiyasu Aizawa, et al. Operator-blinded contact force monitoring during pulmonary vein isolation using conventional and steerable sheaths. *International journal of cardiology*, 177(3):970–976, 2014.

[52] Awaz Ali, Dick H Plettenburg, and Paul Breedveld. Steerable catheters in cardiology: Classifying steerability and assessing future challenges. *IEEE Transactions on Biomedical Engineering*, 63(4):679–693, 2016.

[53] Matteo Cianchetti, Cecilia Laschi, Arianna Menciassi, and Paolo Dario. Biomedical applications of soft robotics. *Nature Reviews Materials*, 3(6):143, 2018.

[54] Stephen C Brown, Derize E Boshoff, Benedicte Eyskens, Luc Mertens, and Marc Gewillig. Use of a microcatheter in a telescopic system to reach difficult targets in complex congenital heart disease. *Catheterization and Cardiovascular Interventions*, 73(5):676–681, 2009.

[55] Robert J Webster III and Bryan A Jones. Design and kinematic modeling of constant curvature continuum robots: A review. *The International Journal of Robotics Research*, 29(13):1661–1683, 2010.

[56] David B Camarillo, Christopher R Carlson, and J Kenneth Salisbury. Configuration tracking for continuum manipulators with coupled tendon drive. *IEEE Transactions on Robotics*, 25(4):798–808, 2009.

[57] Victor C Anderson and Ronald C Horn. Tensor arm manipulator, February 24 1970. US Patent 3,497,083.

[58] Joshua S Mehling, Myron A Diftler, Mars Chu, and Michael Valvo. A minimally invasive tendril robot for in-space inspection. In *The First IEEE/RAS-EMBS International Conference*

on Biomedical Robotics and Biomechatronics, 2006. BioRob 2006., pages 690–695. IEEE, 2006.

[59] Jianzhong Shang, Christopher J Payne, James Clark, David P Noonan, Ka-Wai Kwok, Ara Darzi, and Guang-Zhong Yang. Design of a multitasking robotic platform with flexible arms and articulated head for minimally invasive surgery. In *2012 IEEE/RSJ International Conference on Intelligent Robots and Systems*, pages 1988–1993. IEEE, 2012.

[60] G Chen. Design and modeling of a micro-robotic manipulator for colonoscopy. In *Proc. 5th Int. Workshop on Research and Education in Mechatronics, Annecy, 2005*, pages 109–114, 2005.

[61] David B Camarillo, Christopher F Milne, Christopher R Carlson, Michael R Zinn, and J Kenneth Salisbury. Mechanics modeling of tendon-driven continuum manipulators. *IEEE Transactions on Robotics*, 24(6):1262–1273, 2008.

[62] Hyun-Soo Yoon, Se Min Oh, Jin Hyeok Jeong, Seung Hwan Lee, Kyung Tae, Kyoung-Chul Koh, and Byung-Ju Yi. Active bending endoscope robot system for navigation through sinus area. In *2011 IEEE/RSJ International Conference on Intelligent Robots and Systems*, pages 967–972. IEEE, 2011.

[63] Hiroki Watanabe, Kazuki Kanou, Yo Kobayashi, and Masakatsu G Fujie. Development of a steerable drill for acl reconstruction to create the arbitrary trajectory of a bone tunnel. In *2011 IEEE/RSJ International Conference on Intelligent Robots and Systems*, pages 955–960. IEEE, 2011.

[64] Andreas Muller. Internal preload control of redundantly actuated parallel manipulatorsits application to backlash avoiding control. *IEEE Transactions on Robotics*, 21(4):668–677, 2005.

[65] Guilin Yang, Cong Bang Pham, and Song Huat Yeo. Workspace performance optimization of fully restrained cable-driven parallel manipulators. In *2006 IEEE/RSJ International Conference on Intelligent Robots and Systems*, pages 85–90. IEEE, 2006.

[66] Mohsen Moradi Dalvand, Saeid Nahavandi, and Robert D Howe. An analytical loading model for n-tendon continuum robots. *IEEE Transactions on Robotics*, 34(5):1215–1225, 2018.

[67] Yusof Ganji, Farrokh Janabi-Sharifi, et al. Catheter kinematics for intracardiac navigation. *IEEE Transactions on Biomedical Engineering*, 56(3):621–632, 2009.

[68] Ian D Walker. Continuous backbone continuum robot manipulators. *Isrn robotics*, 2013, 2013.

[69] S. Hirose. *Biologically Inspired Robots,Oxford University Press*. Oxford University Press, 1993.

[70] Ian A Gravagne, Christopher D Rahn, and Ian D Walker. Large deflection dynamics and control for planar continuum robots. *IEEE/ASME transactions on mechatronics*, 8(2):299–307, 2003.

[71] Stephen Tully, Andrea Bajo, George Kantor, Howie Choset, and Nabil Simaan. Constrained filtering with contact detection data for the localization and registration of continuum robots in flexible environments. In *2012 IEEE International Conference on Robotics and Automation*, pages 3388–3394. IEEE, 2012.

[72] D Caleb Rucker and Robert J Webster. Deflection-based force sensing for continuum robots: A probabilistic approach. In *2011 IEEE/RSJ International Conference on Intelligent Robots and Systems*, pages 3764–3769. IEEE, 2011.

[73] Michael W Hannan and Ian D Walker. Kinematics and the implementation of an elephant's trunk manipulator and other continuum style robots. *Journal of robotic systems*, 20(2):45–63, 2003.

[74] Berengere Bardou, Philippe Zanne, Florent Nageotte, and Michel de Mathelin. Control of a multiple sections flexible endoscopic system. In *2010 IEEE/RSJ International Conference on Intelligent Robots and Systems*, pages 2345–2350. IEEE, 2010.

[75] Xiaoping Guo, Troy T Tegg, and Richard E Stehr. Deflectable catheter with distal deflectable segment, July 26 2011. US Patent 7,985,215.

[76] [online]. http://www.stereotaxis.com/index.php, 2016.

[77] Giada Gerboni, Paul WJ Henselmans, Ewout A Arkenbout, Wouter R van Furth, and Paul Breedveld. Helixflex: bioinspired maneuverable instrument for skull base surgery. *Bioinspiration & biomimetics*, 10(6):066013, 2015.

[78] Paul Breedveld and Jules Serge Scheltes. Instrument for fine-mechanical or surgical applications, September 22 2015. US Patent 9,138,133.

[79] Filip Jelínek, Ewout A Arkenbout, Paul WJ Henselmans, Rob Pessers, and Paul Breedveld. Classification of joints used in steerable instruments for minimally invasive surgerya review of the state of the art. *Journal of Medical Devices*, 9(1):010801, 2015.

[80] Mina Chow. Deflectable catheter assembly, February 21 2012. US Patent 8,118,803.

[81] Huu Minh Le, Thanh Nho Do, and Soo Jay Phee. A survey on actuators-driven surgical robots. *Sensors and Actuators A: Physical*, 247:323–354, 2016.

[82] Filip Ilievski, Aaron D Mazzeo, Robert F Shepherd, Xin Chen, and George M Whitesides. Soft robotics for chemists. *Angewandte Chemie International Edition*, 50(8):1890–1895, 2011.

[83] Jamie K Paik and Robert J Wood. A bidirectional shape memory alloy folding actuator. *Smart materials and structures*, 21(6):065013, 2012.

[84] Khaled Elgeneidy, Niels Lohse, and Michael Jackson. Bending angle prediction and control of soft pneumatic actuators with embedded flex sensors–a data-driven approach. *Mechatronics*, 50:234–247, 2018.

[85] Mark D Barrish and Keith Phillip Laby. Arrhythmia diagnostic and/or therapy delivery methods and devices, and robotic systems for other uses, September 20 2018. US Patent App. 15/719,120.

[86] Raphael Deimel and Oliver Brock. A novel type of compliant and underactuated robotic hand for dexterous grasping. *The International Journal of Robotics Research*, 35(1-3):161–185, 2016.

[87] Raphael Deimel and Oliver Brock. A compliant hand based on a novel pneumatic actuator. In *2013 IEEE International Conference on Robotics and Automation*, pages 2047–2053. IEEE, 2013.

[88] Hod Lipson. Challenges and opportunities for design, simulation, and fabrication of soft robots. *Soft Robotics*, 1(1):21–27, 2014.

[89] Ahmed El-Geneidy, David Levinson, Ehab Diab, Genevieve Boisjoly, David Verbich, and Charis Loong. The cost of equity: Assessing transit accessibility and social disparity using total travel cost. *Transportation Research Part A: Policy and Practice*, 91:302–316, 2016.

[90] Yahya Elsayed, Augusto Vincensi, Constantina Lekakou, Tao Geng, CM Saaj, Tommaso Ranzani, Matteo Cianchetti, and Arianna Menciassi. Finite element analysis and design optimization of a pneumatically actuating silicone module for robotic surgery applications. *Soft Robotics*, 1(4):255–262, 2014.

[91] Ming Luo, Mahdi Agheli, and Cagdas D Onal. Theoretical modeling and experimental analysis of a pressure-operated soft robotic snake. *Soft Robotics*, 1(2):136–146, 2014.

[92] Yi Sun, Yun Seong Song, and Jamie Paik. Characterization of silicone rubber based soft pneumatic actuators. In *2013 IEEE/RSJ International Conference on Intelligent Robots and Systems*, pages 4446–4453. Ieee, 2013.

[93] Satya Reddy Atmakuri, Eli I Lev, Carlos Alviar, Edward Ibarra, Albert E Raizner, Stuart L Solomon, and Neal S Kleiman. Initial experience with a magnetic navigation system for percutaneous coronary intervention in complex coronary artery lesions. *Journal of the American College of Cardiology*, 47(3):515–521, 2006.

[94] Carlo Pappone, Gabriele Vicedomini, Francesco Manguso, Filippo Gugliotta, Patrizio Mazzone, Simone Gulletta, Nicoleta Sora, Simone Sala, Alessandra Marzi, Giuseppe Augello,

et al. Robotic magnetic navigation for atrial fibrillation ablation. *Journal of the American College of Cardiology*, 47(7):1390–1400, 2006.

[95] S Deladi, G Krijnen, and Michael Curt Elwenspoek. Parallel-beams/lever electrothermal out-of-plane actuator. *Microsystem technologies*, 10(5):393–399, 2004.

[96] Geoffrey W Rogers. Piezoelectric ultrasonic micro-motor system for minimally invasive surgery-the intellimotor. In *AIP Conference Proceedings*, volume 1433, pages 705–708. AIP, 2012.

[97] Shuxiang Guo, Toshio Fukuda, Tatsuya Nakamura, Fumihito Arai, Keisuke Oguro, and Makoto Negoro. Micro active guide wire catheter system-characteristic evaluation, electrical model and operability evaluation of micro active catheter. In *Proceedings of IEEE International Conference on Robotics and Automation*, volume 3, pages 2226–2231. IEEE, 1996.

[98] Linshuai Zhang, Shuxiang Guo, Huadong Yu, and Yu Song. Performance evaluation of a strain-gauge force sensor for a haptic robot-assisted catheter operating system. *Microsystem Technologies*, 23(10):5041–5050, 2017.

[99] Yili Fu, Anzhu Gao, Hao Liu, and Shuxiang Guo. The master-slave catheterisation system for positioning the steerable catheter. *International Journal of Mechatronics and Automation*, 1(3-4):143–152, 2011.

[100] Naghmeh M Bandari, Roozbeh Ahmadi, Amir Hooshiar, Javad Dargahi, and Muthukumaran Packirisamy. Hybrid piezoresistive-optical tactile sensor for simultaneous measurement of tissue stiffness and detection of tissue discontinuity in robot-assisted minimally invasive surgery. *Journal of biomedical optics*, 22(7):077002, 2017.

[101] Shuxiang Guo, Mingyang Qin, Nan Xiao, Yuan Wang, Weili Peng, and Xianqiang Bao. High precise haptic device for the robotic catheter navigation system. In *2016 IEEE International Conference on Mechatronics and Automation*, pages 2524–2529. IEEE, 2016.

[102] Naghmeh M Bandari, Amir Hooshair, Muthukumaran Packirisamy, and Javad Dargahi. Bending-based formulation of light intensity modulation for miniaturization of optical tactile sensors. In *Optical Sensors*, pages SeM2E–3. Optical Society of America, 2018.

[103] Hao Su, Iulian I Iordachita, Junichi Tokuda, Nobuhiko Hata, Xuan Liu, Reza Seifabadi, Sheng Xu, Bradford Wood, and Gregory S Fischer. Fiber-optic force sensors for mri-guided interventions and rehabilitation: a review. *IEEE sensors journal*, 17(7):1952–1963, 2017.

[104] N. Bandari, J. Dargahi, and M. Packirisamy. Miniaturized optical force sensor for minimally invasive surgery with learning-based nonlinear calibration. *IEEE Sensors Journal*, pages 1–1, 2019.

[105] Graham Robinson and J Bruce C Davies. Continuum robots-a state of the art. In *Proceedings 1999 IEEE international conference on robotics and automation (Cat. No. 99CH36288C)*, volume 4, pages 2849–2854. IEEE, 1999.

[106] Yoshihiko Nakamura, Kousuke Kishi, and Hiro Kawakami. Heartbeat synchronization for robotic cardiac surgery. In *Proceedings 2001 ICRA. IEEE International Conference on Robotics and Automation (Cat. No. 01CH37164)*, volume 2, pages 2014–2019. IEEE, 2001.

[107] Shahir Hasanzadeh and Farrokh Janabi-Sharifi. Model-based force estimation for intracardiac catheters. *IEEE/ASME Transactions on Mechatronics*, 21(1):154–162, 2015.

[108] Bryan A Jones and Ian D Walker. Kinematics for multisection continuum robots. *IEEE Transactions on Robotics*, 22(1):43–55, 2006.

[109] Mahta Khoshnam, Mahdi Azizian, and Rajni V Patel. Modeling of a steerable catheter based on beam theory. In *2012 IEEE International Conference on Robotics and Automation*, pages 4681–4686. IEEE, 2012.

[110] Larry L Howell. *Compliant mechanisms*. John Wiley & Sons, 2001.

[111] Ahmed A Shabana. Flexible multibody dynamics: review of past and recent developments. *Multibody system dynamics*, 1(2):189–222, 1997.

[112] Julien Lenoir, Stephane Cotin, Christian Duriez, and Paul Neumann. Interactive physically-based simulation of catheter and guidewire. *Computers & Graphics*, 30(3):416–422, 2006.

[113] Erich Sorantin, Csongor Halmai, B Erdohelyi, Kálmán Palágyi, László G Nyúl, Krisztián Ollé, Bernhard Geiger, Franz Lindbichler, Gerhard Friedrich, and Karl Kiesler. Spiral-ct-based assessment of tracheal stenoses using 3-d-skeletonization. *IEEE transactions on Medical Imaging*, 21(3):263–273, 2002.

[114] Alejandro F Frangi, Wiro J Niessen, Paul J Nederkoorn, Otto EH Elgersma, and Max A Viergever. Three-dimensional model-based stenosis quantification of the carotid arteries from contrast-enhanced mr angiography. In *Proceedings IEEE Workshop on Mathematical Methods in Biomedical Image Analysis. MMBIA-2000 (Cat. No. PR00737)*, pages 110–118. IEEE, 2000.

[115] Stéphane Cotin, Christian Duriez, Julien Lenoir, Paul Neumann, and Steven Dawson. New approaches to catheter navigation for interventional radiology simulation. In *International Conference on Medical Image Computing and Computer-Assisted Intervention*, pages 534–542. Springer, 2005.

[116] RE Valembois, Paul Fisette, and Jean-Claude Samin. Comparison of various techniques for modelling flexible beams in multibody dynamics. *Nonlinear Dynamics*, 12(4):367–397, 1997.

[117] Pier Paolo Valentini and Ettore Pennestrì. Modeling elastic beams using dynamic splines. *Multibody system dynamics*, 25(3):271–284, 2011.

[118] Fernando M Cardoso and Sergio S Furuie. Guidewire path determination for intravascular applications. *Computer methods in biomechanics and biomedical engineering*, 19(6):628–638, 2016.

[119] Wen Tang, Tao Ruan Wan, Derek A Gould, Thien How, and Nigel W John. A stable and real-time nonlinear elastic approach to simulating guidewire and catheter insertions based on cosserat rod. *IEEE Transactions on Biomedical Engineering*, 59(8):2211–2218, 2012.

[120] Stuart S Antman. Nonlinear plasticity. In *Nonlinear Problems of Elasticity*, pages 603–628. Springer, 1995.

[121] Jean-Claude Samin and Paul Fisette. *Symbolic modeling of multibody systems*, volume 112. Springer Science & Business Media, 2013.

[122] Klaus-Jürgen Bathe and Said Bolourchi. Large displacement analysis of three-dimensional beam structures. *International journal for numerical methods in engineering*, 14(7):961–986, 1979.

[123] Alperen Degirmenci, Paul M Loschak, Cory M Tschabrunn, Elad Anter, and Robert D Howe. Compensation for unconstrained catheter shaft motion in cardiac catheters. In *2016 IEEE International Conference on Robotics and Automation (ICRA)*, pages 4436–4442. IEEE, 2016.

[124] Daniel T Kettler, Richard D Plowes, Paul M Novotny, Nikolay V Vasilyev, J Pedro, and Robert D Howe. An active motion compensation instrument for beating heart mitral valve surgery. In *2007 IEEE/RSJ International Conference on Intelligent Robots and Systems*, pages 1290–1295. IEEE, 2007.

[125] Allison M Okamura, Lawton N Verner, CE Reiley, and Mohsen Mahvash. Haptics for robot-assisted minimally invasive surgery. In *Robotics research*, pages 361–372. Springer, 2010.

[126] Mojtaba Sharifi, Hassan Salarieh, Saeed Behzadipour, and Mahdi Tavakoli. Beating-heart robotic surgery using bilateral impedance control: Theory and experiments. *Biomedical Signal Processing and Control*, 45:256–266, 2018.

[127] Mojtaba Sharifi, Saeed Behzadipour, and Hassan Salarieh. Nonlinear bilateral adaptive impedance control with applications in telesurgery and telerehabilitation. *Journal of Dynamic Systems, Measurement, and Control*, 138(11):111010, 2016.

[128] Farzad Hashemzadeh, Mojtaba Sharifi, and Mahdi Tavakoli. Nonlinear trilateral teleoperation stability analysis subjected to time-varying delays. *Control Engineering Practice*, 56:123–135, 2016.

[129] Samuel B Kesner and Robert D Howe. Position control of motion compensation cardiac catheters. *IEEE Transactions on Robotics*, 27(6):1045–1055, 2011.

[130] Omar Al-Ahmad, Mouloud Ourak, Johan Vlekken, and Emmanuel Vander Poorten. Contact force compensation of a catheter tip for minimally invasive cardiovascular surgery. In *Joint Workshop on Computer/Robot Assisted Surgery, Date: 2019/03/21-2019/03/22, Location: Genoa, Italy*, 2019.

[131] Jacques Gangloff, Romuald Ginhoux, Michel de Mathelin, Luc Soler, and Jacques Marescaux. Model predictive control for compensation of cyclic organ motions in teleoperated laparoscopic surgery. *IEEE Transactions on Control Systems Technology*, 14(2):235–246, 2006.

[132] Samuel B Kesner and Robert D Howe. Robotic catheter cardiac ablation combining ultrasound guidance and force control. *The International Journal of Robotics Research*, 33(4):631–644, 2014.

[133] Shelten G Yuen, Douglas P Perrin, Nikolay V Vasilyev, J Pedro, and Robert D Howe. Force tracking with feed-forward motion estimation for beating heart surgery. *IEEE Transactions on Robotics*, 26(5):888–896, 2010.

[134] Zeineb Zarrouk, Ahmed Chemori, and Philippe Poignet. Force feedback control for compensation of physiological motions in beating heart surgery with real-time experiments. In *3rd International Conference on Systems and Control*, pages 956–961. IEEE, 2013.

[135] Michel Dominici, Philippe Poignet, and Etienne Dombre. Compensation of physiological motion using linear predictive force control. In *2008 IEEE/RSJ International Conference on Intelligent Robots and Systems*, pages 1173–1178. IEEE, 2008.

[136] Bingbin Yu, José de Gea Fernández, and Tao Tan. Probabilistic kinematic model of a robotic catheter for 3d position control. *Soft robotics*, 6(2):184–194, 2019.

[137] Ryan S Penning, Jinwoo Jung, Justin A Borgstadt, Nicola J Ferrier, and Michael R Zinn. Towards closed loop control of a continuum robotic manipulator for medical applications. In

2011 IEEE International Conference on Robotics and Automation, pages 4822–4827. IEEE, 2011.

[138] Ryan S Penning, Jinwoo Jung, Nicola J Ferrier, and Michael R Zinn. An evaluation of closed-loop control options for continuum manipulators. In *2012 IEEE International Conference on Robotics and Automation*, pages 5392–5397. IEEE, 2012.

[139] Meaghan Bowthorpe, Mahdi Tavakoli, Harald Becher, and Robert Howe. Smith predictor-based robot control for ultrasound-guided teleoperated beating-heart surgery. *IEEE Journal of biomedical and Health Informatics*, 18(1):157–166, 2013.

[140] Meaghan Bowthorpe and Mahdi Tavakoli. Physiological organ motion prediction and compensation based on multirate, delayed, and unregistered measurements in robot-assisted surgery and therapy. *IEEE/ASME Transactions on Mechatronics*, 21(2):900–911, 2015.

[141] Assaf Govari and Athanassios Papaioannou. Ablation power control based on contact force, April 10 2014. US Patent App. 13/648,449.

[142] Juan Manuel Florez, Jérôme Szewczyk, and Guillaume Morel. An impedance control strategy for a hand-held instrument to compensate for physiological motion. In *2012 IEEE International Conference on Robotics and Automation*, pages 1952–1957. IEEE, 2012.

[143] Neville Hogan and Stephen P Buerger. Impedance and interaction control. In *Robotics and automation handbook*, pages 375–398. CRC press, 2018.

[144] Pinyo Puangmali, Kaspar Althoefer, Lakmal D Seneviratne, Declan Murphy, and Prokar Dasgupta. State-of-the-art in force and tactile sensing for minimally invasive surgery. *IEEE Sensors Journal*, 8(4):371–381, 2008.

[145] H Xin, JS Zelek, and H Carnahan. Laparoscopic surgery, perceptual limitations and force: A review. In *First Canadian student conference on biomedical computing*, volume 144, 2006.

[146] Yangming Li, Muneaki Miyasaka, Mohammad Haghighipanah, Lei Cheng, and Blake Hannaford. Dynamic modeling of cable driven elongated surgical instruments for sensorless grip

force estimation. In *Robotics and Automation (ICRA), 2016 IEEE International Conference on*, pages 4128–4134. IEEE, 2016.

[147] Jean-Benoît Le Polain De Waroux, Rukshen Weerasooriya, Kalilur Anvardeen, Cynthia Barbraud, Sebastien Marchandise, Christophe De Meester, Cedric Goesaert, Ivone Reis, and Christophe Scavee. Low contact force and force–time integral predict early recovery and dormant conduction revealed by adenosine after pulmonary vein isolation. *EP Europace*, 17(6):877–883, 2015.

[148] Fabien Squara, Decebal Gabriel Latcu, Youssef Massaad, Marouane Mahjoub, Sok-Sithikun Bun, and Nadir Saoudi. Contact force and force-time integral in atrial radiofrequency ablation predict transmurality of lesions. *Europace*, 16(5):660–667, 2014.

[149] Gregory Tholey, Jaydev P Desai, and Andres E Castellanos. Force feedback plays a significant role in minimally invasive surgery: results and analysis. *Annals of surgery*, 241(1):102, 2005.

[150] Mahta Khoshnam, Allan C Skanes, and Rajni V Patel. Modeling and estimation of tip contact force for steerable ablation catheters. *IEEE Transactions on Biomedical Engineering*, 62(5):1404–1415, 2015.

[151] A. Hooshiar, S. Najarian, and J. Dargahi. Haptic telerobotic cardiovascular intervention: a review of approaches, methods, and future perspectives. *IEEE Reviews in Biomedical Engineering*, pages 1–1, 2019.

[152] Hedyeh Rafii-Tari, Christopher J Payne, and Guang-Zhong Yang. Current and emerging robot-assisted endovascular catheterization technologies: a review. *Annals of biomedical engineering*, 42(4):697–715, 2014.

[153] Xiaohua Hu, Ang Chen, Yigang Luo, Chris Zhang, and Edwin Zhang. Steerable catheters for minimally invasive surgery: a review and future directions. *Computer Assisted Surgery*, 23(1):21–41, 2018.

[154] Anish S Naidu, Rajni V Patel, and Michael D Naish. Low-cost disposable tactile sensors for palpation in minimally invasive surgery. *IEEE/ASME Transactions on Mechatronics*, 22(1):127–137, 2017.

[155] Javad Dargahi and Siamak Najarian. Theoretical and experimental analysis of a piezoelectric tactile sensor for use in endoscopic surgery. *Sensor Review*, 24(1):74–83, 2004.

[156] Meysam T Chorsi, Eli J Curry, Hamid T Chorsi, Ritopa Das, Jeffrey Baroody, Prashant K Purohit, Horea Ilies, and Thanh D Nguyen. Piezoelectric biomaterials for sensors and actuators. *Advanced Materials*, page 1802084, 2018.

[157] Michael C Yip, Shelten G Yuen, and Robert D Howe. A robust uniaxial force sensor for minimally invasive surgery. *IEEE transactions on biomedical engineering*, 57(5):1008–1011, 2010.

[158] E. Aranda-Michel, J. Yi, J. Wirekoh, N. Kumar, C. N. Riviere, D. S. Schwartzman, and Y. Park. Miniaturized robotic end-effector with piezoelectric actuation and fiber optic sensing for minimally invasive cardiac procedures. *IEEE Sensors Journal*, 18(12):4961–4968, June 2018.

[159] Andrea Natale, Vivek Y Reddy, George Monir, David J Wilber, Bruce D Lindsay, H Thomas McElderry, Charan Kantipudi, Moussa C Mansour, Daniel P Melby, Douglas L Packer, et al. Paroxysmal af catheter ablation with a contact force sensing catheter: results of the prospective, multicenter smart-af trial. *Journal of the American College of Cardiology*, 64(7):647–656, 2014.

[160] Panagiotis Polygerinos, Tobias Schaeffter, Lakmal Seneviratne, and Kaspar Althoefer. A fibre-optic catheter-tip force sensor with mri compatibility: A feasibility study. In *Engineering in Medicine and Biology Society, 2009. EMBC 2009. Annual International Conference of the IEEE*, pages 1501–1054. IEEE, 2009.

[161] Jagadeesan Jayender, Rajnikant V Patel, and Suwas Nikumb. Robot-assisted catheter insertion using hybrid impedance control. In *Proceedings 2006 IEEE International Conference on Robotics and Automation, 2006. ICRA 2006.*, pages 607–612. IEEE, 2006.

[162] Samuel B Kesner and Robert D Howe. Force control of flexible catheter robots for beating heart surgery. In *IEEE International Conference on Robotics and Automation: ICRA:[proceedings] IEEE International Conference on Robotics and Automation*, page 1589. NIH Public Access, 2011.

[163] Mahta Khoshnam and Rajni V Patel. A pseudo-rigid-body 3r model for a steerable ablation catheter. In *Robotics and Automation (ICRA), 2013 IEEE International Conference on*, pages 4427–4432. IEEE, 2013.

[164] Mert Sedef, Evren Samur, and Cagatay Basdogan. Real-time finite-element simulation of linear viscoelastic tissue behavior based on experimental data. *IEEE Computer Graphics and Applications*, 26(6), 2006.

[165] Amir Hooshiar, Masoud Razban, Naghmeh M Bandari, and Javad Dargahi. Sensing principle for real-time characterization of viscoelasticity in the beating myocardial tissue. In *Computational Intelligence and Virtual Environments for Measurement Systems and Applications (CIVEMSA), 2017 IEEE International Conference on*, pages 72–77. IEEE, 2017.

[166] L Gao, KJ Parker, RM Lerner, and SF Levinson. Imaging of the elastic properties of tissuea review. *Ultrasound in medicine & biology*, 22(8):959–977, 1996.

[167] Miklos Z Kiss, Tomy Varghese, and Timothy J Hall. Viscoelastic characterization of in vitro canine tissue. *Physics in Medicine & Biology*, 49(18):4207, 2004.

[168] Lawrence S Taylor, Amy L Lerner, Deborah J Rubens, and Kevin J Parker. A kelvin-voight fractional derivative model for viscoelastic characterization of liver tissue. In *ASME 2002 International Mechanical Engineering Congress and Exposition*, pages 447–448. American Society of Mechanical Engineers, 2002.

[169] END AB RCA. 376 vi n catheter ablation of accessory atrioventricular connections. *Catheter Ablation of Cardiac Arrhythmias E-book: Expert Consult–Online and Print*, page 375, 2010.

[170] Stuart Schecter, Wei Lin, Aasha Gopal, Roger Fan, and Eric Rashba. Haptics and the heart: Force and tactile feedback system for cardiovascular interventions. *Cardiovascular Revascularization Medicine*, 19(6):36–40, 2018.

[171] Guang-Zhong Yang, James Cambias, Kevin Cleary, Eric Daimler, James Drake, Pierre E Dupont, Nobuhiko Hata, Peter Kazanzides, Sylvain Martel, Rajni V Patel, et al. Medical roboticsregulatory, ethical, and legal considerations for increasing levels of autonomy. *Sci. Robot*, 2(4):8638, 2017.

[172] Faisal Hasan and Johannes Bonatti. Robotically assisted percutaneous coronary intervention: benefits to the patient and the cardiologist, 2015.

[173] Amir Hooshiar, Naghmeh Bandari, and Javad Dargahi. Image-based estimation of contact forces on catheters for robot-assisted cardiovascular intervention. In *Hamlyn Symposium on Medical Robotics*, pages 119–120. The Hamlyn Center-Imperial College London, 2018.

[174] John Till, Vincent Aloi, and Caleb Rucker. Real-time dynamics of soft and continuum robots based on cosserat rod models. *The International Journal of Robotics Research*, 38(6):723–746, 2019.

[175] Wenpeng Gao, Lili Chu, Yili Fu, and Shuguo Wang. A non-linear, anisotropic mass spring model based simulation for soft tissue deformation. In *Ubiquitous Robots and Ambient Intelligence (URAI), 2014 11th International Conference on*, pages 7–10. IEEE, 2014.

[176] Rongjie Kang, David T Branson, Tianjiang Zheng, Emanuele Guglielmino, and Darwin G Caldwell. Design, modeling and control of a pneumatically actuated manipulator inspired by biological continuum structures. *Bioinspiration & biomimetics*, 8(3):036008, 2013.

[177] Vincent A Aloi and D Caleb Rucker. Estimating loads along elastic rods. In *2019 International Conference on Robotics and Automation (ICRA)*, pages 2867–2873. IEEE, 2019.

[178] Xianqiang Bao, Shuxiang Guo, Nan Xiao, Youxiang Li, and Liwei Shi. Compensatory force measurement and multimodal force feedback for remote-controlled vascular interventional robot. *Biomedical microdevices*, 20(3):74, 2018.

[179] Robert K Katzschmann, Cosimo Della Santina, Yasunori Toshimitsu, Antonio Bicchi, and Daniela Rus. Dynamic motion control of multi-segment soft robots using piecewise constant curvature matched with an augmented rigid body model. In *2019 2nd IEEE International Conference on Soft Robotics (RoboSoft)*, pages 454–461. IEEE, 2019.

[180] Byungjeon Kang, Risto Kojcev, and Edoardo Sinibaldi. The first interlaced continuum robot, devised to intrinsically follow the leader. *PloS one*, 11(2):e0150278, 2016.

[181] Yi Chen, Jean H Chang, Alison S Greenlee, Kenneth C Cheung, Alex H Slocum, and Rajiv Gupta. Multi-turn, tension-stiffening catheter navigation system. In *2010 IEEE International Conference on Robotics and Automation*, pages 5570–5575. IEEE, 2010.

[182] Minou Kouh Soltani, Sohrab Khanmohammadi, Farzan Ghalichi, and Farrokh Janabi-Sharifi. A soft robotics nonlinear hybrid position/force control for tendon driven catheters. *International Journal of Control, Automation and Systems*, 15(1):54–63, 2017.

[183] Junghwan Back, Thomas Manwell, Rashed Karim, Kawal Rhode, Kaspar Althoefer, and Hongbin Liu. Catheter contact force estimation from shape detection using a real-time cosserat rod model. In *Intelligent Robots and Systems (IROS), 2015 IEEE/RSJ International Conference on*, pages 2037–2042. IEEE, 2015.

[184] Takahisa Kato, Ichiro Okumura, Hidekazu Kose, Kiyoshi Takagi, and Nobuhiko Hata. Tendon-driven continuum robot for neuroendoscopy: validation of extended kinematic mapping for hysteresis operation. *International journal of computer assisted radiology and surgery*, 11(4):589–602, 2016.

[185] Hong-Jian Yu, Wen-Long Yang, Zheng-Xin Yang, Wei Dong, Zhi-Jiang Du, and Zhi-Yuan Yan. Hysteresis analysis of a notched continuum manipulator driven by tendon. *Mechanical Sciences*, 9(1):211–219, 2018.

[186] Kaiwen Hsiao and Hiromi Mochiyama. A wire-driven continuum manipulator model without assuming shape curvature constancy. In *2017 IEEE/RSJ International Conference on Intelligent Robots and Systems (IROS)*, pages 436–443. IEEE, 2017.

[187] Ning Tan, Xiaoyi Gu, and Hongliang Ren. Pose characterization and analysis of soft continuum robots with modeling uncertainties based on interval arithmetic. *IEEE Transactions on Automation Science and Engineering*, 16(2):570–584, 2018.

[188] Hedyeh Rafii-Tari, Jindong Liu, Su-Lin Lee, Colin Bicknell, and Guang-Zhong Yang. Learning-based modeling of endovascular navigation for collaborative robotic catheterization. In *International conference on medical image computing and computer-assisted intervention*, pages 369–377. Springer, 2013.

[189] Mahta Khoshnam and Rajni V Patel. Estimating contact force for steerable ablation catheters based on shape analysis. In *2014 IEEE/RSJ International Conference on Intelligent Robots and Systems*, pages 3509–3514. IEEE, 2014.

[190] Wenqiang Chi, Jindong Liu, Hedyeh Rafii-Tari, Celia Riga, Colin Bicknell, and Guang-Zhong Yang. Learning-based endovascular navigation through the use of non-rigid registration for collaborative robotic catheterization. *International journal of computer assisted radiology and surgery*, 13(6):855–864, 2018.

[191] D Braganza, DM Dawson, ID Walker, and N Nath. Neural network grasping controller for continuum robots. In *Proceedings of the 45th IEEE Conference on Decision and Control*, pages 6445–6449. IEEE, 2006.

[192] Michele Giorelli, Federico Renda, Marcello Calisti, Andrea Arienti, Gabriele Ferri, and Cecilia Laschi. Neural network and jacobian method for solving the inverse statics of a cable-driven soft arm with nonconstant curvature. *IEEE Transactions on Robotics*, 31(4):823–834, 2015.

[193] Gundula Runge, Mats Wiese, and Annika Raatz. Fem-based training of artificial neural networks for modular soft robots. In *2017 IEEE International Conference on Robotics and Biomimetics (ROBIO)*, pages 385–392. IEEE, 2017.

[194] Nabil Simaan, Kai Xu, Wei Wei, Ankur Kapoor, Peter Kazanzides, Russell Taylor, and Paul Flint. Design and integration of a telerobotic system for minimally invasive surgery of the throat. *The International journal of robotics research*, 28(9):1134–1153, 2009.

[195] Anthony J Sanfilippo, Vivian M Abascal, Mary Sheehan, Lynn B Oertel, Pamela Harrigan, Robert A Hughes, and Arthur E Weyman. Atrial enlargement as a consequence of atrial fibrillation. a prospective echocardiographic study. *Circulation*, 82(3):792–797, 1990.

[196] Malini Govindan, Anatoli Kiotsekoglou, Samir K Saha, and A John Camm. Right atrial myocardial deformation by two-dimensional speckle tracking echocardiography predicts recurrence in paroxysmal atrial fibrillation. *Journal of echocardiography*, 15(4):166–175, 2017.

[197] Mohsen Moradi Dalvand, Saeid Nahavandi, and Robert D Howe. Fast vision-based catheter 3d reconstruction. *Physics in Medicine & Biology*, 61(14):5128, 2016.

[198] Mohsen Dalvand, Saeid Nahavandi, and Robert D Howe. High speed vision-based 3d reconstruction of continuum robots. In *2016 IEEE International Conference on Systems, Man, and Cybernetics (SMC)*, pages 000618–000623. IEEE, 2016.

[199] Minhan Li, Rongjie Kang, Shineng Geng, and Emanuele Guglielmino. Design and control of a tendon-driven continuum robot. *Transactions of the Institute of Measurement and Control*, 40(11):3263–3272, 2018.

[200] Michael C Yip and David B Camarillo. Model-less feedback control of continuum manipulators in constrained environments. *IEEE Transactions on Robotics*, 30(4):880–889, 2014.

[201] Soufian T AlMahameed and Ohad Ziv. Ventricular arrhythmias. *Medical Clinics*, 103(5):881–895, 2019.

[202] Sana M Al-Khatib, William G Stevenson, Michael J Ackerman, William J Bryant, David J Callans, Anne B Curtis, Barbara J Deal, Timm Dickfeld, Michael E Field, Gregg C Fonarow, et al. 2017 aha/acc/hrs guideline for management of patients with ventricular arrhythmias and the prevention of sudden cardiac death: a report of the american college of cardiology/american heart association task force on clinical practice guidelines and the heart rhythm society. *Journal of the American College of Cardiology*, 72(14):e91–e220, 2018.

[203] Robert J Webster III, Joseph M Romano, and Noah J Cowan. Mechanics of precurved-tube continuum robots. *IEEE Transactions on Robotics*, 25(1):67–78, 2008.

[204] Mohammad Jolaei, Amir Hooshiar, and Dargahi. Kinematic analysis and position control of flexible tendon-driven catheter for minimally invasive cardiac surgery. In *30th International Conference on Adaptive Structures and Technologies*, pages 1–2. Concordia University, 2019.

Appendix A

A. Coding lines developed in MATLAB to define the desired trajectory

```matlab
function [L1, L2, L3, L4,
SS,dt,Traj,theta,phi]=ClassificationLenghtfinder(type)
%% Define Trajectory
% close all; clf; clc;
hold on
if(nargin == 0)
    type = 1;
end
[x,y]=createSpiral(0.2,2); B=[x;y];
% [x,y]=createCircle(5*[0 1.2 2]); C=[x;y];
[x,y]=createCircle([5]); C=[x;y]; %% createCircle(radious*[1 1.2
1.4])
% D=[ 0 -10  0  10 0 ; 0   0  10 0  0];
DD=[0 -1 -2 0 2 0 -1 0;0 -1 0 2 0 -2 -1 0]
D=[3*DD 5*DD 7*DD];

[F,dt]=sinasoidalInput(5,-5,0.5,type);        %% (amp,av,freq,m)
E=[linspace(0,-10,20);zeros(1,20)];           %% INITIALS FOR
SINASOIDAL MOVEMENTS
%%
if(type == 1)
    points=B;
elseif(type == 2)
    points=C;
elseif(type == 3)
    points=D;
elseif(type == 4)
    points=E;
elseif(type == 5)
    points=F;
elseif(type == 6)
    points=F;
elseif(type == 7)
    points=G;                                 %% Defining
phi&theta manualy  "G" Points
end
Traj=createTrajectory(points,type);
%% Check Domain
isDomain(Traj);
if all(isDomain(Traj))
    display('Feasible Trajectory')
else
    display('Non Feasible')
end
%% Traj2theta&phi
[r, theta, phi]=dec2sph(Traj');
%% Defining phi&theta manualy  "G" Points
```

```matlab
%% Spiral
% N=50;
% theta=zeros(5,1);
% phi=linspace(0,0.06,5)';
% theta=[theta ; linspace(-pi,pi,N)']; phi=[phi;
linspace(0.06,pi/10,N)']; r=ones(size(theta))*40
%% circle
% theta=linspace(-pi,pi,20)';  phi=ones(size(theta))*pi/6;
r=ones(size(theta))*40;
% [xx,yy,zz]=sph2dec(r,theta,phi);
% theta=[0;(linspace(-pi,pi,N))'];
% phi=[0;(ones(N,1)*(0.06))];
% theta=(-pi)*ones(5,1);
% phi=linspace(0,pi/10,5)';
%%  concentric circles
% IP=5;
% maxphi=pi/10;
% theta=zeros(IP,1);
% phi=linspace(0,maxphi,IP)';
% n=4;
% for i=1:n
%     theta=[theta  ;(linspace(-pi,pi,N))'];
%     phi=[phi ;(ones(N,1)*(((i/n)*(maxphi)))')];
% end
% theta=[theta;zeros(IP,1)];
% phi=[phi;linspace(0,pi/10,IP)'];
% figure('Name','Phi&Theta')
% plot(phi,theta);
% xlabel('Phi'); ylabel('Theta');
% r=ones(size(theta))*40;
%% plot phi&&theta manually
[xx,yy,zz]=sph2dec(r,theta,phi);
G=[xx , yy];
figure('Name','Phi&Theta To Dec')
plot3(xx,yy,zz,'-','linewidth',4)
hold on
plotSphere2(50)
axis equal; grid on;
xlabel('X'); ylabel('Y'); zlabel('Z');
%% Forming SS to be applied in classifier
% [SS,~,~]=NN10phithetaR2D(theta, phi);    %%COMPENSATION
% idx=find(theta< 0.7);theta(idx)=[]; phi(idx)=[];   %% TRYING
TO MAKE "3"SHAPED TRAJECTORY
SS=[theta phi]; idx=find(phi<0.06); SS(idx,:)=[];  %%dt(idx)=[];
%% Classifier Loading
load('Classifier')
Classes = trainedModel3.predictFcn(SS);
```

```matlab
%% Network
L=zeros(size(SS,1),4);
for i=1:size(SS,1)
    if   (Classes(i)==12)
         L(i,:)=NN10Ang2Len12(SS(i,:));      %%0.85;
    elseif(Classes(i)==13)
         L(i,:)=NN10Ang2Len13(SS(i,:));
    elseif(Classes(i)==24)
         L(i,:)=NN10Ang2Len24(SS(i,:));
    elseif(Classes(i)==34)
         L(i,:)=NN10Ang2Len34(SS(i,:));
    end
end
L1=L(:,1);
L1(find(L1<0))=0;
L2=L(:,2);                                   %%*1.3;
L2(find(L2<0))=0;
L3=L(:,3);                                   %%*0.8
L3(find(L3<0))=0;
L4=L(:,4);                                   %%*1.1
L4(find(L4<0))=0;
L=[L1,L2,L3,L4]
figure('Name','Predicted Lengths');
plot(L,'.');
legend('L1','L2','L3','L4')
end
%% ALL THE NEEDED FUNCTIONS
function [X,Y]=createSpiral(V,N)
t=linspace(0,2*pi*N,100);
X=V*t.^1.5.*cos(t);
Y=V*t.^1.5.*sin(t);
end
function [X,Y]=createCircle(V)
t=linspace(0,2*pi,100);
X=[]; Y=[];

for i=V
%     X=[X (i.*cos(t))];
    X=[X i-(i.*cos(t))];
    Y=[Y i.*sin(t)];
end
for i=V
%     X=[X (i.*cos(t))];
    X=[X -i+(i.*cos(t))];
    Y=[Y i.*sin(t)];
end
end
```

```matlab
function Traj=createTrajectory(WayPoints,k)
Traj=NaN;
[m,n]=size(WayPoints);
P=[];
X=[];0
Y=[];
Z=[];
 N=20;
if m==2
     if k==1
for i=1:n-1
X=[X linspace(WayPoints(1,i),WayPoints(1,i+1),N)];
Y=[Y linspace(WayPoints(2,i),WayPoints(2,i+1),N)];
end
     else
         X=WayPoints(1,:);
         Y=WayPoints(2,:);
     end
Z=getFeasibleZ([X;Y]);
Traj=[X;Y;Z];
plot3(X,Y,Z,'linewidth',4)
hold on
plotSpace();
end
end
function Z=getFeasibleZ(P)
Z=[];
[m,n]=size(P);
load('DomainBoundary');
load('FITXYZ_Ellipsoid');
Rmin=mean(R)-2*(std(R));
Rmax=mean(R)+2*(std(R));
Ravg=mean(R);
if (m==2)
       for i=1:n
          Pp=P(:,i);
c1=Pp(2)-feval(fit1,Pp(1));
c2=Pp(2)-feval(fit2,Pp(1));
c3=Pp(2)-feval(fit3,Pp(1));
c4=Pp(2)-feval(fit4,Pp(1));
if(c1*c2>0 & c3*c4>0 || true) %% inja ridim
Z(i)=feval(FITXYZ, [ Pp(1) Pp(2)]);
else
Z(i)=NaN;
end
       plot3(Pp(1),Pp(2),Z(i))
 end
```

```
end
end
function state=isDomain(P)
state=[];
[m,n]=size(P);
load('DomainBoundary');
if (m==3)
for i=1:n
        Pp=P(:,i);
c1=Pp(2)-feval(fit1,Pp(1));
c2=Pp(2)-feval(fit2,Pp(1));
c3=Pp(2)-feval(fit3,Pp(1));
c4=Pp(2)-feval(fit4,Pp(1));
Rp=norm(Pp);
Rmin=mean(R)-2*(std(R));
Rmax=mean(R)+2*(std(R));
if(c1*c2>0 & c3*c4>0 & Rp>Rmin & Rp<Rmax)
state(i)=1;
else
state(i)=0;
 end
 end
end
end
function [r,theta,phi]=dec2sph(varargin)
input=cell2mat(varargin);
x=input(:,1);
y=input(:,2);
z=input(:,3);
r=sqrt(x.^2+y.^2+z.^2);
theta=atan2(y,x);
phi=atan2(sqrt(x.^2+y.^2),z);
end
function plotSpace()
load('Workspace_calibrationTest_2_Classifier_LsEdited')
% T=evalin('base','T');
U=T(:,6:9); Kx=0.252; Ky=0.270; Kz=0.286;
CM=[Kx, 0, 0, 0; 0, Ky/2, 0, Ky/2; 0, 0, Kz, 0];
U1=T(:,6); V1=T(:,7); U2=T(:,8); V2=T(:,9);
N=length(T); PM=[];
for i=1:N
    PM(1:3,i)=CM*[[U1(i),V1(i),U2(i),V2(i)]'];
end
xlabel({'X';''}); ylabel({'Y';''}); zlabel({'Z';''})
plot3(PM(3,:),PM(1,:),-PM(2,:)+40,'.')
xlim([-32 32]); ylim([-32 32]); zlim([0 50])
%% POSITION ROTATION
```

```matlab
XX=getPtip2(U);
%% DRAW SPHERE
plotSphere2(50)
figure('Name','positions in mm');
plot(XX(:,1),'.')
hold on
plot(XX(:,2),'.')
plot(XX(:,3),'.')
legend('X','Y','Z')
end
function [P]=getPtip2(U)
Kx=0.252; Ky=0.270; Kz=0.286;
CM=[Kx, 0, 0, 0; 0, Ky/2, 0, Ky/2; 0, 0, Kz, 0];
U1=U(:,1); V1=U(:,2); U2=U(:,3); V2=U(:,4);
N=length(U1);
PM=[];
P=[];
T=[0 0 1 0 ; 1 0 0 0 ; 0 -1 0 40 ; 0 0 0 1];
for i=1:N
    PM(1:3,i)=CM*[[U1(i),V1(i),U2(i),V2(i)]'];
    PP=T*[PM(1:3,i); 1];
    P=[P PP(1:3)];
end
P=P';
xlabel({'X';''})
ylabel({'Y';''})
zlabel({'Z';''})
plot3(P(:,1),P(:,2),P(:,3),'.')
xlim([-32 32])
ylim([-32 32])
zlim([0 50])
end
function plotSphere2(N)
 L0=40; Ds=[];
theta=linspace(0,degtorad(90),N);
phi=linspace(0,2*pi,N);
d=sqrt(2)*L0./(2*theta).*sqrt(1-cos(2*theta));
range=1:1:N;
for i=range

X=(d(i)*ones(1,length(range))).*sin(theta(i)*ones(1,length(range
))).*cos(phi(range));

Y=(d(i)*ones(1,length(range))).*sin(theta(i)*ones(1,length(range
))).*sin(phi(range));
```

```matlab
Z=(d(i)*ones(1,length(range))).*cos(theta(i)*ones(1,length(range
)));
    hold on;
        plot3(X,Y,Z,'-','color',[0 0 0]+0.5);
    Ds=[Ds;[X' Y' Z']];
end
axis equal; grid on;
xlabel('X'); ylabel('Y'); zlabel('Z');
xlim([-32 32])
ylim([-32 32])
zlim([0 50])
hold on
view(-90,90)
end
function [x,y,z]=sph2dec(varargin)
input=cell2mat(varargin);

r=input(:,1);
theta=input(:,2);
phi=input(:,3);

z=r.*cos(phi);
y=r.*sin(phi).*sin(theta);
x=r.*sin(phi).*cos(theta);
end
function [F,dt]=sinasoidalInput(amp,av,freq,m)
np=500;        %%500
F=[]; dt=0;
if m==5
    % cos
    t=linspace(0,5/freq,np);
    dt=diff(t); dt=[dt dt(end)]';
    y=zeros(1, np); x=av+amp/2*(cos(2*pi*freq*t.^2)-1);
    F=[x; y];
    % sin
else if m==6
    t=linspace(0,1/freq,np);
    dt=diff(t); dt=[dt dt(end)]';
    y=zeros(1, np); x=av+amp*(sin(2*pi*freq*t));
    F=[x; y];
end
end
end
```

109

Appendix B

B. Coding lines developed in MATLAB to solve the tissue dynamic model

```matlab
function error=EqAssemebly(P)
global L
global Power
global w
global Fexp
%parameters=(P1,P2,P3,P4.P5);
 Fexp=evalin('base','F23');
 T=evalin('base','t23');
 N=length(T);
 M=(length(P)-1)/2; % number of Kelvin units.
 K=zeros(M,M);
 C=zeros(M,M);
 for i=1:M-1
     K(i,i:i+1)=P(2*i)*[-1 1];
     C(i,i:i+1)=P(2*i+1)*[-1 1];
 end
 K(M,M)=-P(end-1);
 C(M,M)=-P(end);
 C_i=inv(C);
 x0=evalin('base','D23');
 x=zeros(M+1,N);
 xd=zeros(M+1,N);
 x(1,:)=x0;
 xd(1,1:N-1)=diff(x(1,:))./diff(T)';
 dt=diff(T);
 L=zeros(N,1);
 for i=1:N-1
   L(i)=(P(1)*(x(2,i)-x(1,i))^Power);
   xd(2:end,i)=C_i*(L(i)-K*x(2:end,i));
   x(2:end,i+1)=xd(2:end,i)*dt(i)+x(2:end,i);
 end
%  error=abs(sum(Fexp.*x0+F.*x0));
%     w=.9;
%  error=w*max(abs(Fexp+L))+(1-w)*(norm(L(L<0)));
%  error=w*max(abs(Fexp+L))+(1-w)*min(abs(Fexp+L));
%  error=norm(Fexp+L)
%  error=((rms(Fexp+L))*100)/0.15
%  error=rms(Fexp+L)
   error=rms(abs(Fexp)-abs(L));
   plot(T,Fexp)
   hold on
```

```matlab
    plot(T,-L)
    hold off
end
% K0=P(1); k1=P(2); c1=P(3); k2=P(4); C2=P(5); k3=P(6); c3=P(7); k4=P↙
(8); c4=P(9); k5=P(10); c5=P(11); k6=P(12); c6=P(13); k7=P(14); c7=P↙
(15); k8=P(16);c8=X(17);
```